Towards attosecond 4D imaging of atomic-scale dynamics by single-electron diffraction

Alexander Gliserin

München 2014

Towards attosecond 4D imaging of atomic-scale dynamics by single-electron diffraction

Alexander Gliserin

Dissertation
an der Fakultät für Physik
der Ludwig–Maximilians–Universität
München

vorgelegt von
Alexander Gliserin
aus Kriwoj Rog, Ukraine

München, den 17. Februar 2014

Erstgutachter: Prof. Dr. Ferenc Krausz
Zweitgutachter: Prof. Dr. Eberhard Riedle
Tag der mündlichen Prüfung: 04. Juni 2014

谨献给爱妻 淑芬

Zusammenfassung

Viele physikalische und chemische Prozesse, die unser tägliches Leben bestimmen, laufen auf atomaren Längen- und Zeitskalen ab. Zeitaufgelöste Elektronenbeugung eignet sich durch die kurze de-Broglie-Wellenlänge schneller Elektronen hervorragend zur Aufklärung atomarer Strukturdynamik („4D imaging“). Dafür sind Elektronenpulsdauern im Bereich von Femtosekunden (10^{-15} s) oder kürzer erforderlich. Schwierigkeiten dabei sind die Coulombabstoßung sowie Dispersion von nichtrelativistischen Elektronenwellenpaketen im Vakuum. Momentan ist deshalb die Zeitauflösung von Beugungsexperimenten auf einige hundert Femtosekunden beschränkt. Dies ist unzureichend für die Untersuchung ultraschneller Primärprozesse in Molekülen und Festkörpern.

Um mit Elektronenbeugung künftig eine Zeitauflösung von wenigen Femtosekunden oder darunter zu erreichen, werden in dieser Arbeit vier neue Konzepte untersucht und kombiniert: Erstens wird die Coulombabstoßung verhindert, indem nur ein einzelnes Elektron pro Puls erzeugt wird, welches sich nicht selbst abstößt, jedoch in der Beugung an Atomen mit sich selbst interferiert.

Zweitens wird eine Dispersionskontrolle für Elektronenpulse mittels zeitabhängiger elektrischer Felder bei Mikrowellenfrequenzen eingesetzt. So werden die Einzelelektronenpulse zeitlich komprimiert bei gleichzeitiger Energieverbreiterung, wodurch prinzipiell fast beliebig kurze Pulsdauern ermöglicht werden.

Drittens wird aus ultrakurzen Laserpulsen, die sowohl für die Elektronenerzeugung, als auch zur Anregung einer Probe in einem Beugungsexperiment eingesetzt werden, ein Mikrowellensignal erzeugt, dessen Signal-Rausch-Verhältnis durch optische Überhöhung um drei Größenordnungen verbessert wird. Dies ermöglicht eine zeitliche Synchronisation zwischen dem Mikrowellenfeld und den Laserpulsen mit einer Präzision von unter einer Femtosekunde.

Viertens wird in dieser Arbeit eine Kreuzkorrelation zwischen Laserfeldern und Elektronenpulsen gemessen, um die mögliche Zeitauflösung von Beugungsexperimenten mit komprimierten Einzelelektronenpulsen zu ermitteln und die theoretischen

Modelle für Elektronendispersion und -kompression zu überprüfen. Diese neu entwickelte Charakterisierungsmethode basiert auf dem Prinzip einer Streak-Kamera mit optischen Feldern und besitzt potenziell eine Zeitauflösung im Bereich von Attosekunden (10^{-18} s).

Diese vier Konzepte bieten eine klare Perspektive zur Verbesserung der Zeitauflösung von Elektronenbeugung hin zur Zeitskala weniger Femtosekunden oder darunter. Dies eröffnet die Möglichkeit, Elektronendichten in Bewegung zu beobachten. Die in dieser Arbeit nachgewiesene komprimierte Elektronenpulsdauer beträgt (28 ± 5) fs Halbwertsbreite, entsprechend einer Standardabweichung von (12 ± 2) fs, bei einer de-Broglie-Wellenlänge von 0.08 Å. Dies sind momentan die kürzesten für Beugung geeigneten Elektronenpulse, etwa sechsfach kürzer als was bisher erreicht worden ist. Atomare Ortsauflösung und eine exzellente transversale Kohärenz wird anhand von Beugung an einem komplexen organischen molekularen Kristall demonstriert. Ultraschnelle Elektronenbeugung erfüllt nun die nötigen Anforderungen zur Untersuchung der schnellsten Primärprozesse in Molekülen und Festkörpern mit atomarer Auflösung in Raum und Zeit.

Abstract

Many physical and chemical processes which define our daily life take place on atomic scales in space and time. Time-resolved electron diffraction is an excellent tool for investigation of atomic-scale structural dynamics ("4D imaging") due to the short de Broglie wavelength of fast electrons. This requires electron pulses with durations on the order of femtoseconds (10^{-15} s) or below. Challenges arise from Coulomb repulsion and dispersion of non-relativistic electron wave packets in vacuum. Thus, the temporal resolution of diffraction experiments is currently limited to some hundreds of femtoseconds, which is insufficient for studying ultrafast primary processes in molecules and solids.

In order to eventually advance the temporal resolution of electron diffraction into the few-femtosecond range or below, four new concepts are investigated and combined in this work: First, Coulomb repulsion is avoided by using only a single electron per pulse, which does not repel itself but interferes with itself when being diffracted from atoms.

Secondly, dispersion control for electron pulses is implemented with time-dependent electric fields at microwave frequencies, compressing the duration of single-electron pulses at the expense of simultaneous energy broadening. Thus, almost arbitrarily short pulse durations can be potentially achieved.

Thirdly, a microwave signal is derived from an ultrashort laser pulse train, which is also used for the generation of electron pulses as well as for the excitation of a sample in a diffraction experiment. Optical enhancement improves the signal-to-noise ratio of the microwave signal by three orders of magnitude, which allows a temporal synchronization between the microwave field and the laser pulses with a precision below one femtosecond.

Fourthly, a cross-correlation between laser fields and electron pulses is measured in this work with the purpose of determining the possible temporal resolution of diffraction experiments employing compressed single-electron pulses and to verify the theoretical models of electron pulse dispersion and compression. This novel char-

acterization method uses the principles of a streak camera with optical fields and potentially offers attosecond (10^{-18} s) temporal resolution.

These four concepts show a clear path towards improving the temporal resolution of electron diffraction into the few-femtosecond domain or below, which opens the possibility of observing electron densities in motion. In this work, a compressed electron pulse's duration of (28 ± 5) fs full width at half maximum, corresponding to a standard deviation of (12 ± 2) fs, at a de Broglie wavelength of 0.08 Å is achieved. Currently, this constitutes the shortest electron pulses suitable for diffraction, about sixfold shorter than in previous work. Atomic spatial resolution and excellent transverse coherence is demonstrated via diffraction from a complex organic molecular crystal. Ultrafast electron diffraction now meets the requirements for investigating the fastest primary processes in molecules and solids with atomic resolution in space and time.

Contents

List of publications by the author

A. Gliserin, M. Walbran, F. Krausz, and P. Baum. *28-fs electron pulses for atomic-scale diffraction*. Submitted (2015).

A. Gliserin, M. Walbran, and P. Baum. *A high-resolution time-of-flight spectrometer for sub-relativistic electron pulses*. In preparation (2015).

A. Gliserin, S. Lahme, M. Walbran, F. Krausz, and P. Baum. *Ultrafast Single-Electron Diffraction*. In Ultrafast Phenomena XIX. Vol. 162, 295–298 (2015).

A. Gliserin, F. O. Kirchner, M. Walbran, F. Krausz, and P. Baum. *Laser Streaking of Free-Electron Pulses at 25 keV*. In Ultrafast Phenomena XIX. Vol. 162, 291–294 (2015).

F. O. Kirchner*, A. Gliserin*, F. Krausz, and P. Baum. *Laser streaking of free electrons at 25 keV*. Nature Photonics **8**, 52–57 (2014).
* Comparable contribution

A. Gliserin, M. Walbran, and P. Baum. *Passive optical enhancement of laser-microwave synchronization*. Applied Physics Letters **103**, 031113 (2013).

A. Gliserin, A. Apolonski, F. Krausz, and P. Baum. *Compression of single-electron pulses with a microwave cavity*. New Journal of Physics **14**, 073055 (2012).

S. H. Chew, F. Süssmann, C. Späth, A. Wirth, J. Schmidt, S. Zherebtsov, A. Guggenmos, A. Oelsner, N. Weber, J. Kapaldo, A. Gliserin, M. I. Stockman, M. F. Kling, and U. Kleineberg. *Time-of-flight-photoelectron emission microscopy on plasmonic structures using attosecond extreme ultraviolet pulses*. Applied Physics Letters **100**, 051904 (2012).

M. K. Fischer, A. Gliserin, A. Laubereau, and H. Iglev. *Ultrafast electron transfer processes studied by pump-repump-probe spectroscopy*. Journal of Biophotonics **4**, 178–183 (2011).

H. Iglev, M. K. Fischer, A. Gliserin, and A. Laubereau. *Ultrafast Geminate Recombination after Photodetachment of Aqueous Hydroxide*. Journal of the American Chemical Society **133**, 790–795 (2011).

List of acronyms

ADC	Analog-to-digital converter
DC	Direct current
EELS	Electron energy loss spectroscopy
FEL	Free-electron laser
FWHM	Full width at half maximum
MCP	Micro-channel plate
PLL-VCO	Phase-locked loop voltage-controlled oscillator
PSD	Power spectral density
RF	Radiofrequency
rms	Root mean square
SNR	Signal-to-noise ratio
TDC	Time-to-digital converter
TE	Transverse electric
TM	Transverse magnetic
ToF	Time of flight
UED	Ultrafast electron diffraction
UV	Ultraviolet
XUV	Extreme ultraviolet

Chapter 1

Observing atomic and electronic motion

Time-dependent interactions between the fundamental constituents of matter dictate the course of our material world and its appearance. Understanding phenomena in nature thus requires insight into the underlying *dynamics* – from the largest scope of astronomy down to the most minute of atoms and elementary particles.

Processes which are faster than the human perception have been studied since the end of the 19$^{\text{th}}$ century, the first one being motion of animals visualized via photographic movies [1]. Since then, numerous visualization techniques have been developed to experimentally access ever faster dynamics. For instance, time-resolved photography has progressed tremendously, resulting nowadays in so-called femtophotography with a temporal resolution of a few picoseconds, which allows visualizing propagating bursts of light [2].

Some of the most fundamental processes defining our immediate life take place on molecular and atomic length scales. Microscopic interactions between electrons and nuclei determine macroscopic properties of substances. Therefore, understanding their dynamics, i.e. the motion of nuclei and charge densities in space and time, is of the highest importance for prediction and control of chemical reactions or transformations in condensed matter [3]. The length scale of atoms and molecules is in the ångström range (10^{-10} m), while the time scale of their dynamics is determined by the energy and bandwidth of the process and by the masses of the involved particles or structures [4, 5]. For example, biological macromolecules, such as proteins, fold due to weak interactions (e.g. hydrogen bonds) on time scales of microseconds and above [6], while typical motions of simple molecules in the condensed phase – e.g. collective lattice oscillations or phase transformations in solids, vibrations or reorientation in liquids – take place on time scales of picoseconds [7–9] and below [7, 10, 11]. Primary processes in chemical reactions or molecular transformations involve motion of individual atoms (i.e. nuclei) on femtosecond time scales [4, 11].

Motion of electronic charge densities takes place on the attosecond time scale, on which the nuclei are nearly inert due to their large mass [12], at least at moderate interaction energies which do not destroy the atom or molecule. Although chemical processes – in their classical meaning – are therefore "frozen" in this regime, electronic attosecond dynamics drive some of the most fundamental phenomena in atomic and solid state physics. Recent research in this field includes decay of atomic inner-shell vacancies by an Auger process [13], time-resolved observation of electron tunneling in atoms [14], dissociation dynamics in diatomic molecules [15], tracing of coherent valence electron motion [16], attosecond control of collective electron motion on the nanoscale in metals [17] and dielectrics [18], and delayed photoemission between electrons from different bands [19] or orbitals [20] by means of attosecond streaking. Further fundamental processes on the attosecond time scale, such as the formation and breakup of molecular bonds or the time-dependent polarization response of electron densities upon interaction with electromagnetic fields, constituting the refractive index of a material, are yet to be investigated [5]. Attosecond science is a rapidly advancing field offering, ultimately, unforeseen possibilities to study the very constituents of matter and their fundamental interactions [21].

1.1 The pump-probe experiment

Direct observation or measurement of ultrafast phenomena in *real-time*, i.e. from a single process, is limited by the sampling rate of current detectors. Optical high-speed cameras are capable of a sampling rate of up to 200 million exposures per second [22], though at the expense of a very limited number of consecutive exposures, providing a temporal resolution of a few nanoseconds, while electronic sampling with a real-time bandwidth of up to 100 GHz and an according temporal resolution on the order of picoseconds has been recently demonstrated [23].

In order to study even faster processes, a repetitive technique must be employed to capture snapshots of a particular ultrafast process at different instances in time with a "slow" detector. The dynamics is initiated via an ultrafast interaction, referred to as the pump pulse, which is typically significantly shorter than the dynamics of the process under investigation, and probed after a well-defined delay time by a second pulse, the probe pulse, which usually does not modify the dynamics of the process but illuminates it within an ultrashort time window, allowing the detector to capture a snapshot with a temporal resolution limited only by the duration of the pulses. In the case of optical photography, the probe pulse would be a short flash of light facilitating an ultrafast exposure independent of the speed of the camera's shutter or image processing. In order to elucidate the complete dynamics, a series of snapshots needs to be taken at different pump-probe delay times. Provided

repeatability of both the investigated process and the interactions with the pump and probe pulses, this technique offers the possibility to make "movies" of ultrafast dynamics, albeit not in real-time.

Note that the pulses for pump-probe interaction can be of any nature suitable to initiate and illuminate the process of interest. Usually, ultrashort pulses of (laser) light and/or particles are employed in pump-probe experiments for studying ultrafast dynamics in matter (see section 1.3).

1.2 The streak camera

Another tool to visualize the temporal structure of a process is the streak camera [24, 25]. Here, a well-defined temporal gradient – typically a time-dependent electric field – is used to map (or streak) the temporal profile of an incoming pulse into an easily accessible quantity, such as position or energy, on a detector. The streaked pulse needs to be prepared such that it carries the temporal information of the process of interest; or the pulse itself (e.g. a light or particle pulse) can be temporally characterized in that way.

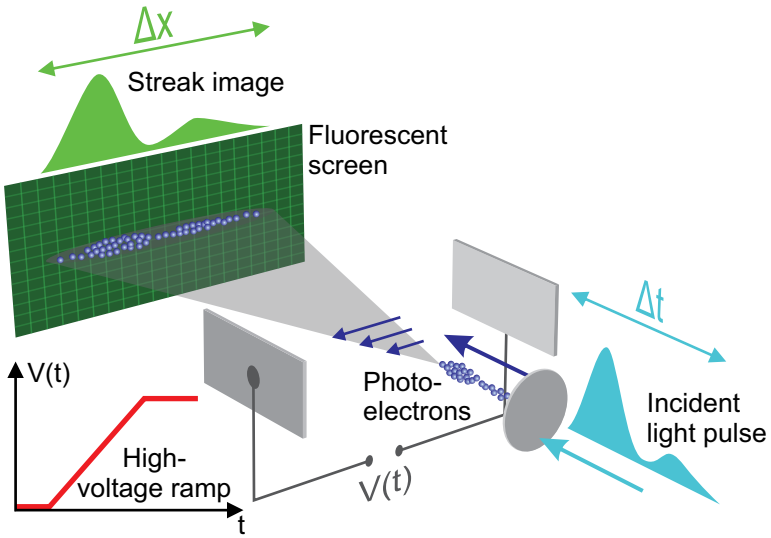

Figure 1.1: Schematic concept of a streak camera for characterizing the temporal profile of a light pulse. The light is converted into photoelectrons, which are then streaked in a transient electric field generated by an applied voltage ramp, V(t). The temporal width, Δt, is thereby mapped into a spatial width, Δx, on the screen. Figure adapted from [21].

Fig. 1.1 illustrates the principle of a streak camera intended to record the temporal structure of an optical pulse. The pulse hits a photocathode, i.e. a thin metal film, usually on a transparent substrate, and emits electrons from the cathode via

the photoelectric effect. The temporal profile of the photoelectron pulse is closely related to that of the optical pulse, given that the photoemission yield is proportional to the optical intensity and the duration of the photoemission dynamics is negligible compared to the temporal structure of the pulse. The electron pulse then propagates through a pair of plates biased at an electric potential that changes linearly in time. This transient electric field effects a time-dependent transverse momentum transfer to the electron pulse, leading to a sideways deflection, which maps the pulse's temporal profile into the position on the screen. The temporal resolution of a streak camera therefore depends only on the temporal gradient used for streaking and the resolution of the detector for the quantity which the temporal profile is mapped into (e.g. position or energy).

This technique serves as a powerful tool for ultrafast metrology when using transients of intense optical fields for streaking [19, 21, 26, 27] and is capable of resolving delays on the order of several attoseconds [20].

1.3 Ultrafast spectroscopy, microscopy, and diffraction

Historically, the development of ultrafast coherent light sources – from the first mode-locked helium-neon laser [28] until present-day Ti:sapphire oscillators [29] capable of producing few-cycle optical pulses [30] – is constantly pushing the limits of ultrafast science towards extreme temporal resolutions. The shortest controllable bursts of light reported up to now are pulses of coherent extreme ultraviolet (XUV) radiation, created by high-order harmonic generation, with durations below 80 attoseconds [31–33], constituting the shortest man-made temporal confinement.

Laser-driven femtosecond pump-probe experiments offer vast insight into the dynamics of chemical processes by means of optical pump-probe spectroscopy [34], establishing the field of femtochemistry [3, 12, 35, 36], while attosecond XUV pulses allow studying electronic dynamics, as pointed out in the previous sections[1]. However, despite the superior temporal resolution achieved with laser pulses in the optical to the XUV range, their potential to elucidate molecular or atomic structures is limited to indirect spectroscopic approaches. While resonant to many electronic transitions, the wavelength of this light ($\sim$1 µm to $\sim$10 nm) is orders of magnitude too large to directly visualize the motion of atoms [4, 37, 38]. Replacing classical static light sources for spectroscopy with ultrafast lasers is straightforward; however, a sophisticated choice of excited states and transitions of the system under investiga-

[1] A rigorous review of current techniques and applications for attosecond XUV pump-probe spectroscopy and streaking can also be found in [21].

tion as well as extensive modeling is required to determine structural dynamics from time-resolved spectroscopy. Linking spectral features to atomic or electronic motion, e.g. in order to map out pathways of chemical reactions, is intricate when lacking a direct access to the structural changes. This is caused particularly by degenerate states and superposition of different transitions of similar resonance frequencies, which are difficult to separate [10, 39], or by radiationless transitions [40].

Microscopy techniques with atomic spatial resolution employ beams of light or particles with sub-atomic wavelengths and respective energies for illumination, a notable exception being the scanning tunneling microscope, which uses an atomic-sized probe to map out a surface with ångström resolution [41, 42]. The first work on the determination of the atomic structure of simple crystals in reciprocal space by X-ray diffraction has been conducted a century ago by W. L. Bragg [43]. Since then, crystallography has advanced tremendously and allows nowadays visualizing huge biomolecules consisting of ten thousands of atoms [44]. Besides X-rays, particle beams of electrons [45] or neutrons [46] are used for diffraction crystallography, providing complementary insight due to their different nature of interaction with the specimen and the required energies for atomic resolution. Alongside diffraction, which usually requires crystalline samples, electron microscopy facilitates direct imaging of atoms with sub-ångström resolution [47] and thus provides a first-hand access to the most fundamental constituents of life [48].

Despite the enormous progress in both the visualization techniques with atomic resolution and the control on ultrashort time scales, the combination of these two fields into 4D imaging, i.e. highest resolution in space and time [49], is challenging and still emerging. Applying the well-established principles from the generation of ultrashort laser pulses to high-energy X-ray or electron beams capable of atomic spatial resolution promises an unprecedented understanding of structural dynamics by directly observing atoms and electron densities in motion.

Ultrashort X-ray pulses

Femtosecond X-ray pulses at 30 keV have been reported in 1996 for the first time [50, 51] by Thomson scattering of highly intense femtosecond near-infrared laser pulses from relativistic electron bunches [52]. Previously, sources of pulsed X-rays have utilized synchrotron radiation, providing a pulse duration limited by the picosecond duration of electron bunches in particle accelerators at that time. Current sources of ultrashort and highly brilliant X-ray pulses are free-electron lasers (FEL) [53–59], providing soft [53–55] and hard [56–58] X-rays with pulse durations in the ten-femtosecond to few-femtosecond range. Coherent X-ray pulses are emitted as synchrotron radiation when ultrarelativistic electron bunches of very low emittance

(closely related to the phase space volume, see section 2.1) undergo a wiggling motion in an undulator, which is an arrangement of periodically alternating static magnetic fields. The electron pulse is sliced into wavelength-spaced microbunches inside a long undulator due to interaction with the emitted synchrotron radiation, providing a coherent self-amplification of the spontaneous synchrotron emission [60] or amplification of seeded coherent X-ray radiation [61]. Generation of attosecond hard-X-ray pulses is proposed by electron bunch shaping in FEL [62], thus effectively compressing the X-ray pulse, or by enhanced Thomson scattering, employing tightly focused electron and laser beams from present-day sources [63].

These X-ray sources – despite their enormous potential in time-resolved crystallography and atomic-scale imaging – are extremely intricate and limited to a few large-scale facilities worldwide, as they require particle accelerators capable of providing electron bunches in the 100 MeV to GeV range. However, recent progress in the development of compact laser-driven particle accelerators [64, 65] might promote table-top and comparatively inexpensive coherent few-femtosecond X-ray sources in the future [59, 66, 67].

Ultrashort electron pulses

Ultrafast electron diffraction (UED) with sub-relativistic electrons and a temporal resolution of one picosecond has been pioneered about two decades ago [68, 69] and is currently approaching the 100 fs range for dense electron bunches [70]. According to Bragg's famous law for diffraction in reflection, $2d \sin\theta = n\lambda$, d being the interplanar distance of a crystal lattice ($\sim$1 Å), θ the diffraction angle, and n an integer, the diffracted beam's wavelength, λ, should be on the order of a few ångström to a few picometer for practical diffraction angles. Due to the electron's wave properties and the associated de Broglie wavelength, this condition is fulfilled at moderate kinetic energies, ranging from only a couple of eV to mildly relativistic $\sim$300 keV. Diffraction with electrons at kinetic energies in the MeV range requires additional electron optics to enlarge the very small diffraction angles for practical imaging and a more intricate electron source [71]. In electron microscopy, kinetic energies up to a few MeV are used in order to increase imaging resolution [72].

The charged particle nature of electrons leads to some key advantages in using electron beams rather than X-rays for atomic-scale diffraction and imaging: Electrons can be accelerated in static electric fields. High-voltage sources up to some 100 kV for static accelerators are readily available, stable, and inexpensive. Thus, contrary to photons from synchrotron radiation sources, electrons can be generated at conveniently low kinetic energies, e.g. by thermal emission, field emission, or photoemission, and then accelerated to the desired kinetic energy. This substantially

relaxes the requirements for generation of femtosecond electron pulses compared to X-ray pulses. A common femtosecond laser oscillator is sufficient for photoemission of ultrashort electron pulses from a thin metal foil for subsequent acceleration in a static electric field, thereby facilitating compact table-top experiments. Electron beams can be deflected and manipulated by means of electric and magnetic fields – the enormous progress in electron microscopy with high resolution has been only feasible on account of available and well-designed electron optics – while X-ray optics is limited to reflection or diffraction at grazing incidence [73], which is more intricate to control. Furthermore, the scattering cross-section of electrons in the 100 keV range (typical for diffraction or microscopy) is about six orders of magnitude larger, while the radiation damage due to the deposited energy after inelastic scattering is about three orders of magnitude smaller[2] compared to X-rays from current FEL sources [4]. The energy deposition from a highly intense X-ray FEL pulse usually destroys the sample and therefore a diffraction image has to be captured from a single shot and during a sufficiently short time before the atomic structure is significantly altered by the pulse [55].

However, in some cases the nature of electrons is unfavorable. The high scattering cross-section leads to a short inelastic mean free path inside the sample [74, 75], limiting the sample's thickness typically to some tens of nanometers for experiments in transmission. This constraint can be somewhat relaxed by using electrons at kinetic energies in the MeV range [71] if the additional effort is acceptable, whereas X-rays penetrate through matter over macroscopic distances[3]. The space charge of dense electron bunches poses another severe limitation. In contrast to photons, electrons within a bunch interact with each other via the Coulomb force. This mutual repulsion leads to self-broadening in space and time, resulting in an increased emittance and pulse duration and reduced coherence, except for highly relativistic energies. The broadening can be compensated to some extent by compression techniques [70, 76, 77]; however, the minimum pulse duration is limited by the space charge density at the beam's focus (in space and time). Moreover, vacuum is dispersive for sub-relativistic electrons, i.e. electrons of different kinetic energies travel at different velocities, thus any energy spread, whether from the generation process or due to space charge interaction, leads to a temporal broadening, especially at the very beginning of the acceleration where the electrons are still slow [78–80].

Currently, there is no prospective technology to advance the pulse duration of dense electron bunches at sub-relativistic kinetic energies suitable for diffraction into

[2]This refers to the deposited energy normalized to the elastic scattering events, which constitute the diffraction image.

[3]Note that an extended penetration depth of a probe pulse, unless velocity-matched with the pump pulse, limits the temporal resolution to the propagation time through the sample.

the few-femtosecond or even attosecond domain. Hence, avoiding space charge, i.e. using single-electron pulses, is a crucial requirement for achieving ultimate temporal resolutions with UED [81]. With absent broadening due to space charge, only the dispersion of vacuum for electrons and their energy spread have to be taken into account. Reducing the energy spread of the electrons by minimizing their excess kinetic energy after photoemission [82–84] not only increases the coherence but also reduces the temporal broadening of single-electron pulses due to dispersion [82]. In the absence of space charge, dispersion compensation with time-varying longitudinal electric fields transforms the phase space of the electrons almost linearly (cf. section 3.1), allowing for temporal compression to nearly arbitrarily short pulse durations at the expense of an accordingly increased energy spread [37, 79–81]. This approach is demonstrated in this work. However, the limitation to one electron per pulse constitutes a considerable constraint for practical UED. For an adequate signal-to-noise ratio of a diffraction image, 10^5–10^6 electrons (or more, depending on the studied system and desired resolution) need to be collected by the detector [78]. This necessitates very long acquisition times or very high pulse repetition rates in the 100 kHz to MHz range, respectively, when using single-electron pulses. The studied dynamics are therefore limited to reversible processes and highly stable specimens capable of withstanding millions of consecutive pump-probe cycles [85, 86]. When using optical pump pulses for excitation at high repetition rates and nanometer thin samples for UED in transmission, thermal damage can be a substantial issue [87].

Albeit being demanding with respect to the choice and excitation of the sample, single-electron UED paves the path towards visualizing dynamics on the electronic time scale and atomic length scale and offers the prospect of the highest spatiotemporal resolution available in the near future. Moreover, the achievable temporal resolution of ultrafast electron microscopy can also be improved by using ultrashort single-electron pulses [37], provided a minimized dispersion of the electron optics. In this work, sub-relativistic single-electron pulses are compressed to about 28 fs FWHM (about 12 fs of standard deviation) and fully characterized (see sections 7.2 and 7.3). This demonstrates, to our knowledge, the shortest electron pulses at a kinetic energy suitable for diffraction or microscopy reported up to now, having a sixfold shorter duration than in previous work [70]. More importantly, the here presented concepts provide a clear perspective for advancing 4D imaging into the few-femtosecond or even attosecond regime.

A survey of currently existing and proposed sources for both photon and electron pulses for studying ultrafast structural dynamics is depicted in fig. 1.2. The wavelength, as a measure for the structural resolving power, and the full-width-at-half-maximum (FWHM) pulse duration of various instruments, covering femtosecond and attosecond optical and XUV laser pulses, ultrafast X-ray sources, ultrafast

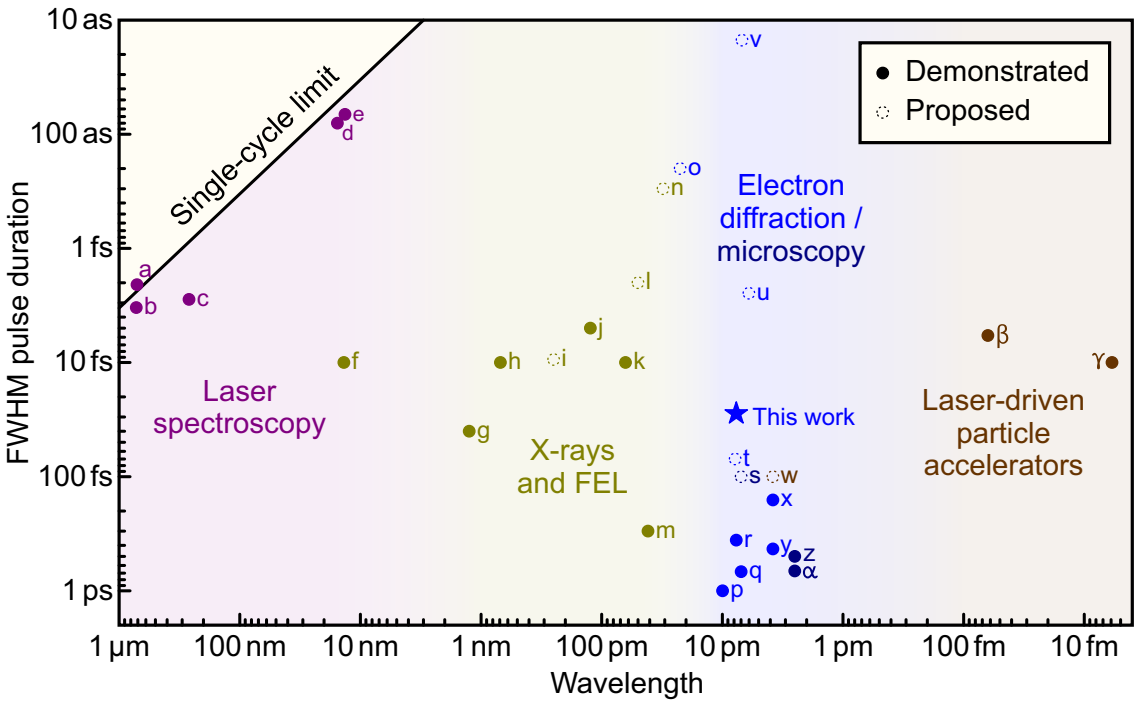

Figure 1.2: Spatiotemporal resolution capabilities of various sources for ultrashort photon and electron pulses in comparison to the present work. Wavelength denotes the de Broglie wavelength in the case of electron pulses. The single-cycle limit is the duration of one period of the according wavelength at the speed of light in vacuum. Note that the temporal localization due to the uncertainty principle can become shorter than one cycle if the bandwidth is sufficiently high, as demonstrated in a. References: a [27], b [31], c [88], d [31], e [33], f [53], g [89], h [54], i [66], j [56], k [58], l [90], m [51], n [63], o [91], p [68], q [92], r [93], s [94], t [82], u [80], v [37], w [95], x [70], y [96], z [97], α [98], β [65], γ [64].

electron diffraction and microscopy, as well as high-energy particle accelerators capable of providing ultrashort electron bunches, are shown in comparison to the sub-relativistic single-electron pulses for ultrafast diffraction generated in this work.

1.4 Basics of a laser-driven UED experiment

Unlike femtosecond laser spectroscopy [10], UED poses the technological challenge of employing both ultrashort laser and electron pulses. Since vacuum is dispersive for electrons and their charged nature leads to mutual repulsion and broadening (unless single-electron pulses are used) – both not being the case for photons – control of electron pulses strongly differs from laser optics. Nevertheless, manipulation of the electron pulse's spatial, temporal, and spectral properties (e.g. deflection and steering, focusing, and dispersion control) can be achieved in analogy to optics by using magnetic and electric fields.

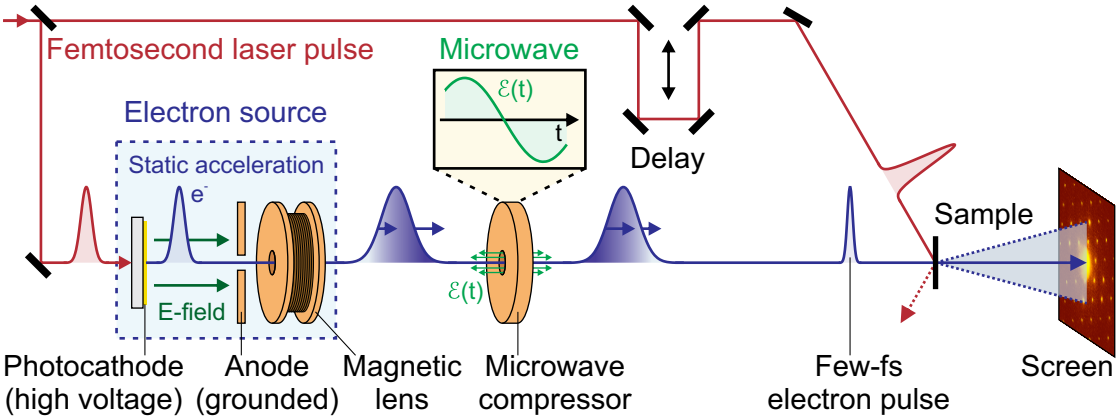

Figure 1.3: Concept of a laser-driven UED pump-probe experiment, employing electron pulse compression with microwave fields. A femtosecond laser pulse is divided into two parts by a beam splitter. One part is used to excite photoinduced structural dynamics at the sample, while the other part generates an ultrashort electron pulse for diffraction via photoemission from a thin metal cathode. The electron pulse is accelerated in a static electric field and collimated or focused by a solenoid magnetic lens. A microwave compressor with a longitudinally oscillating electric field can be used to reverse the dispersion of the electron pulse, which leads to self-compression (see section 3.1). A variable optical delay allows acquiring diffraction snapshots at different delay times after excitation, thus recording a "structural movie".

Fig. 1.3 shows a schematic of the UED pump-probe concept used in this work, suitable for structural probing of photoinduced dynamics. Femtosecond laser pulses are divided via a beam splitter into a pump and a probe part. While the pump pulse is used for excitation of structural dynamics at the sample, the probe pulse is used to generate ultrashort electron pulses via photoelectric emission from a photocathode. A typical photocathode consists of a thin film (5 nm to 50 nm) of gold or silver coated on a quartz or sapphire substrate and is biased at a negative high voltage (−10 kV to −300 kV). In order to generate photoelectrons, the work function of the material has to be overcome by the laser pulse's photon energy, which is in the ultraviolet (UV) range (∼4.2 eV for thin gold films [99]). Since most UED experiments employ Ti:sapphire lasers with a central wavelength around 800 nm (1.55 eV of photon energy), photoemission from a gold film requires either parametric conversion of the fundamental laser frequency, such as frequency tripling (providing 4.65 eV of photon energy) [81] or continuum generation [82], or multiphoton absorption [100]. The density of the generated electron packets is adjusted via the optical pulse energy on the photocathode or via the optical intensity in the case of multiphoton photoemission. For minimized transverse emittance[4], which is a requirement for coherent and

[4]The transverse emittance is defined as the product between the source size and the divergence of a longitudinal cross-section of a beam (e.g. in units of mm mrad). For asymmetric beam profiles, the emittance depends on the cross-section's angle with respect to the beam profile [101].

tightly focused or collimated electron beams, the laser has to be tightly focused onto the photocathode in order to confine the area of photoemission [87]. This is limited to the order of 1 µm by the laser's wavelength and focusing optics, although it can be substantially reduced by using nanometer-sized tips for photoemission instead of metal films [102, 103], which can also potentially improve transverse coherence [104] and provide an enhanced electrostatic field around the tip for acceleration [85]. However, this field is strongly curved close to the tip, which leads to a curved spatial profile of the electron pulse (i.e. an intrinsic spatiotemporal broadening), while a flat source produces spatially flat electron packets due to the homogeneous electrostatic field [105]. Since the photoemission process is statistical (see section 2.1) and "instantaneous" with respect to the femtosecond laser pulse's duration [19, 20], its temporal spread is initially transferred to the electron pulses.

The electron pulses are then accelerated in a static electric field towards a grounded anode with a small center hole, thus acquiring their final energy for diffraction. The beam is divergent due to the intrinsic transverse momentum spread of the electrons after photoemission (see section 2.1) and the defocusing effect arising from distortions of the electric field at the anode hole [106]. Since vacuum is dispersive for electrons, i.e. electrons with higher kinetic energy travel faster than those with lower kinetic energy, unless accelerated to highly relativistic energies, any initial energy spread after photoemission leads to temporal broadening of the pulse, essentially at the very beginning of the static acceleration [78–80]. This initial dispersion can be minimized by using the highest possible electric fields for acceleration. It is limited to ∼10 kV/mm due to vacuum breakdown [82] and can only be overcome by dynamic acceleration with radiofrequency (RF) [79, 107] or laser fields [64, 65, 95], which pose other challenges, particularly with respect to synchronization (in the case of RF acceleration) and achievable energies and energy spreads suitable for diffraction (in the case of laser acceleration). A solenoid constitutes a focusing lens for the electron beam, utilizing the gradient of the magnetic field, which can be controlled by the current through the solenoid. It can be employed for collimation, focusing, or beam steering to some extent. Further details and a theoretical background of the magnetic lens can be found elsewhere [87, 105, 106].

Highest temporal resolutions require temporal compression of the electron packets, since it is impossible or impractical to maintain the shortest pulse duration during the entire propagation from the photoemission at the photocathode until the diffraction sample due to the vacuum's dispersion for electrons as pointed out above. Concepts for compression with static fields include magnetic chicanes [108], electrostatic reflectrons [109, 110], or a combination of electric and magnetic fields [91]. In the absence of space charge, these approaches can entirely reverse the dispersion gained by the electron pulses during propagation and by that recompress their du-

ration to the initial value at the instant of photoemission, i.e. the duration of the generating laser pulse. In contrast, the employment of time-dependent electric fields allows almost arbitrary compression of the electron pulses, even below the laser pulse's duration, at the expense of increased bandwidth, which promises reaching the few-femtosecond or even attosecond range (see section 3.1). A common approach for an electron pulse compressor with time-dependent electric fields is a cavity resonantly driven by a RF signal at microwave frequencies (see section 3.2), which can compress both single-electron and dense electron pulses [70, 76–81, 96].

The electron pulse compressor acts as a longitudinal lens, i.e. it compresses the pulse duration at a certain point along the beam, which is referred to as the temporal focus. The parameters of the compressor, e.g. RF field amplitude and frequency in the case of a microwave cavity, have to be chosen such that the temporal focus coincides with the position of the sample. In transmission geometry, as depicted in fig. 1.3, the thickness of the sample must not exceed some tens of nanometers (cf. section 1.3); therefore, the time for the electrons to pass through the sample is in the attosecond range. However, the transverse extent (i.e. the beam diameter) of a collimated or focused electron beam from a photocathode source is on the order of 10 µm–100 µm. Thus, the laser pump pulse needs to illuminate each point of the sample's surface, which is probed by the electron beam, at the same temporal delay across the transverse profile of the electron pulse. Unless both the laser and the electron beam propagate collinearly and impinge perpendicularly onto the sample, group velocity matching needs to be ensured, e.g. by choosing appropriate angles, such that the wavefronts of both pulses sweep along the sample's surface at a fixed delay (see section 7.1). Also, the entire cross-section of the electron probe beam at the sample should be covered by the laser pump beam in order to obtain the highest signal of structural change. Bulk samples can also be used for diffraction in reflection under a grazing angle. Here, the area of the sample's surface swept by the electron pulse is much larger than for a transmission geometry, requiring a larger energy of the laser pulse for excitation of this area. The same group velocity matching argument applies to the grazing incidence geometry, which necessitates a wavefront tilt of the laser pump pulses [111, 112].

Note that the entire electron beam, from the photocathode to the detector, needs to propagate inside a vacuum chamber at a pressure in the mid high vacuum range ($<10^{-5}$ hPa) in order to avoid scattering from residual gas molecules. For surface sensitive applications, e.g. diffraction in reflection, contamination of the sample's surface by the residual gas needs to be avoided and might require ultrahigh vacuum conditions ($<10^{-9}$ hPa). Moreover, contamination of the photocathode can potentially alter the material's work function and hence the yield and energy spread of photoemission, which affects the long-term stability of the electron source [113].

Chapter 2

Single-electron pulses for UED

In contrast to optical pulses, electron pulses suffer from both dispersion in vacuum and electron-electron interaction via the Coulomb force within the pulse, as pointed out in section 1.3. Although dense electron bunches offer the advantage of recording a diffraction image of a transient atomic structure within a single shot in a UED pump-probe experiment (see section 8.2), the temporal resolution is strongly limited by Coulomb broadening of the electron pulse. Achieving ultimate temporal resolutions for studying electronic dynamics with UED thus requires the elimination of space charge.

The approach in this work is to use single-electron pulses for UED. In the absence of space charge, the propagation and dispersion of the electrons is dictated by a simple equation of motion without any nonlinear internal forces. Moreover, single-electron pulses facilitate excellent dispersion control by means of time-dependent energy modulation with microwave fields, allowing virtually arbitrary temporal compression of the pulse's duration (see chapter 3).

2.1 Phase space statistics and coherence of single-electron pulses

In order to understand the concept of pulse duration and compression of single-electron pulses, it is instructive to consider their phase space during propagation. At any given instant in time, each electron can be classically described by its position and momentum in three-dimensional space, spanning a six-dimensional phase space. The temporal properties of collimated high-energy electron bunches can be described by a simplified two-dimensional phase space consisting of the longitudinal position and momentum, i.e. along the main direction of propagation. The transverse phase space, on the other hand, provides information about the beam's diameter and

divergence. The phase space volume, enclosing all states of the electrons, is a direct measure for the longitudinal and transverse emittance, respectively, when converting the relative momentum spread into an angular spread (cf. section 1.4). For dense electron packets, the spatial and temporal profile is directly evident from the distribution of each electron (or the electron density) constituting the packet within the phase space: The longitudinal spatial distribution yields the pulse duration when divided by the mean velocity, while the longitudinal momentum distribution is correlated with the packet's energy spread or bandwidth.

For single-electron pulses, however, the concept of statistical quantities, i.e. distributions, applies to ensembles of many consecutive pulses with respect to a repetitive timing reference, as illustrated in fig. 2.1. This is a consequence of the discrete (quantum) nature of electrons: It is impossible to measure the spatial or temporal distribution of a single electron's quantum mechanical wave function, since the particle is consumed after being detected by any mechanism and its wave function collapses at a particular point in space and time. Only a repetitive measurement yields a distribution and eventually a diffraction image. Therefore, we implicitly invoke the statistics of repetitive ensembles when referring to pulse durations, beam diameters, or other distributions related to the phase space of single-electron pulses [85]. It is noteworthy that the intrinsic quantum mechanical wave function (or any statistical distribution) of a single-electron pulse cannot be measured exactly, because a repetitive measurement imprints additional broadening on the statistical quantities of the pulse, e.g. due to timing jitter or limited resolution [114], yielding convolutions as upper limits for those quantities.

Illumination of an extended source, such as a flat photocathode, leads to incoherent photoemission, i.e. a random probability distribution of the emission across the illuminated area and within the laser pulse's duration, weighted by the laser's intensity profile in space and time. Typically, photoelectrons are emitted from within a few-nanometer depth of a metal film after UV excitation [115]. The physics describing the subsequent propagation of the electrons to the surface is indirect and rather complex, involving scattering, electron-electron interaction, and refraction from rough surfaces [116–118]. Therefore, the excess energy, $E_{\mathrm{ph}} - \Phi$, E_{ph} being the photon energy (for single-photon photoemission) and Φ the material's work function, is smeared out due to inelastic scattering during the emitted electron's travel from the bulk into vacuum, resulting in an energy spread. The laser pulse's finite bandwidth (i.e. E_{ph} spans over a range of energies) also contributes to the bandwidth of the electrons. Likewise, elastic and inelastic scattering leads to a broad angular distribution of the emitted electrons, which is assumed to be isotropic into a half sphere [82], despite the directed momenta of the laser pulse's photons.

Coherence is particularly important for diffraction, as it requires interference of the electron wave packets scattered from different unit cells of the sample's crystal

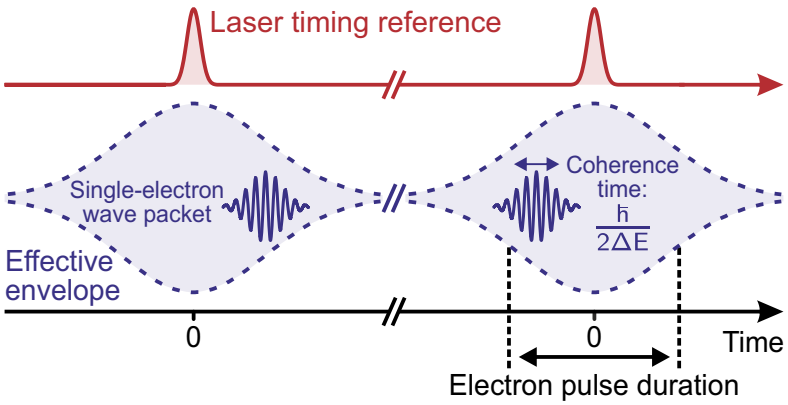

Figure 2.1: Illustration of the effective pulse duration of single electrons [5, 81, 85]. All statistical quantities of single-electron pulses refer to ensembles of many consecutive (repetitive) single-electron wave packets. The duration of single-electron pulses is therefore defined as the distribution of arrival times with respect to a repetitive timing reference, e.g. the laser pump pulses at the sample. Note that the coherence time of a single-electron wave packet, which follows from the uncertainty relation and the bandwidth ΔE, can be substantially shorter than the effective pulse duration at the sample due to the random emission time (within the laser pulse's duration) and dispersion.

lattice. Single electrons interfere with themselves, as in Young's double-slit experiment; therefore, their coherence length has to exceed the dimensions of a unit cell. The longitudinal coherence time[1], τ_c, as illustrated in fig. 2.1, follows from the energy-time uncertainty: $\tau_c \approx \hbar/(2\Delta E)$, $\hbar$ being the reduced Planck constant and ΔE the bandwidth (time and energy distributions referring to standard deviations). The corresponding longitudinal coherence length, $\xi_l = v_l \tau_c$, v_l being the longitudinal velocity, is in the ∼100 nm range for typical UV photoemission sources. However, the transverse coherence length, ξ_t, determines the visibility of Bragg spots for diffraction in transmission, constituting an important beam parameter for electron diffraction experiments. A common definition is $\xi_t = \lambda/(2\pi\sigma_\theta)$, λ being the de Broglie wavelength and σ_θ the standard deviation of the angular spread, which is a consequence of the transverse momentum distribution [76, 78, 82, 86, 114]. According to this definition, the visibility of interference fringes (or Bragg spots) is reduced by 12 % over a transverse distance of ξ_t at the diffraction sample [119]. Typically, transverse coherence lengths from photocathode sources for UED are in the sub-nanometer to few-nanometer range [76, 82, 114]. This coherence can be in principle arbitrarily improved by magnifying the beam [86, 104]; however, the maximum practical beam diameter is technically limited by the sample's transverse size (some 100 µm in the case of thin crystalline foils for transmission) and the laser

[1] In optics, the temporal coherence is sometimes defined as $\tau_c \approx h/\Delta E$, which follows from the autocorrelation theorem [119].

pump pulse's energy. Since dense electron packets suffer from increased transverse momentum spread due to Coulomb repulsion, single-electron sources can in principle provide better transverse coherence. In combination with magnifying electron optics, a transverse coherence of 20 nm has been achieved at the diffraction sample with a reasonably small beam radius of ∼80 µm (standard deviation), allowing investigation of large biomolecules [86]. Reducing the momentum spread by using an ultracold electron source [83, 84, 104] rather than a thin-film photocathode renders a different approach for increasing the coherence of electron pulses.

2.2 Dispersion of single-electron pulses

Dispersion relates the angular frequency (or phase velocity) ω of a plane wave to its wave number $k = 2\pi/\lambda$, λ being the wavelength, by the group velocity $v(k) = \partial\omega(k)/\partial k$. For electromagnetic waves, $v(k) = c$ in vacuum, i.e. the group velocity is constant for all wavelengths. However, inside a material $v(k) = c/n(k)$ with the wavelength-dependent refractive index $n(k)$. A wavelength-dependent group velocity leads to temporal spreading of a wave packet (e.g. a pulse), which is a superposition of plane waves of different wavelengths. In analogy to electromagnetic waves, the angular frequency ω and wave number k of a matter wave are related to its energy E (sum of the kinetic energy and rest energy of a particle) and momentum p, respectively, according to de Broglie, by $E = \hbar\omega$ and $p = \hbar k$. Therefore, the dispersion of electrons in vacuum in terms of energy and momentum is given by:

$$E(p) = \sqrt{p^2c^2 + m_e^2c^4}, \tag{2.1}$$

m_e being the electron's rest mass. The relativistic momentum, p, is given by:

$$p = \gamma m_e v, \qquad \gamma = \frac{1}{\sqrt{1 - \left(\frac{v}{c}\right)^2}}, \tag{2.2}$$

where v is the electron's group velocity and γ the Lorentz factor. Note that p and v are vector quantities and we consider projections along their directions. In the sub-relativistic case ($v \ll c \Rightarrow \gamma \approx 1$), $p \approx m_e v$ and eqn 2.1 can be simplified by Taylor expansion:

$$E(p) \approx \frac{p^2}{2m_e} + m_e c^2 = \frac{1}{2}m_e v^2 + m_e c^2 \tag{2.3}$$

Subtracting the rest energy, $E_0 = m_e c^2$, from eqn 2.3 yields the classical kinetic energy of an electron:

$$E_{kin}(p) = E(p) - E_0 \approx \frac{p^2}{2m_e} = \frac{1}{2}m_e v^2 \tag{2.4}$$

Note that the electron's group velocity, which results from the dispersion relation, $v = \partial E(p)/\partial p$, is the same for both the relativistic and non-relativistic case and is identical to the velocity of a particle defined in Newtonian mechanics as the time derivative of the particle's position. As a direct consequence, a longitudinal distribution of initial sub-relativistic velocities, Δv_z, at a position z_0 with (ideally) zero or negligible initial spatial spread leads to a spatial broadening, Δz, after a propagation time t:

$$\Delta z = \Delta v_z t, \tag{2.5}$$

while the center of the distribution propagates a distance of $z = z_0 + v_z t$ with a central velocity of v_z. For realistic distributions of particles with a nonzero phase space volume, the transformation of a certain velocity or momentum spread into a spatial spread after some propagation needs to be calculated using the equation of motion for each particle. In the absence of space charge, the propagation of a dynamic phase space density function, $\varrho(z, p_z, t)$, with $p_z = m_e v_z$, describing the temporal evolution of an arbitrary initial phase space density, $\varrho_0(z, p_z)$, is given by:

$$\varrho(z, p_z, t) = \varrho_0(z - v_z t, p_z) \tag{2.6}$$

The projection of the density function onto the position or momentum axis, respectively, then yields the corresponding distribution.

Fig. 2.2 illustrates the phase space of a dispersing repetitive ensemble of single-electron pulses (cf. section 2.1). For simplicity, the velocity is shown instead of the momentum. In fig. 2.2 (a), the velocities and positions of the single electrons are initially uncorrelated, representing the situation at the instant of photoemission at the photocathode. After some propagation time, the finite velocity spread leads to a broadening of the initial spatial distribution according to eqns 2.5 and 2.6 and a linear correlation of the velocity with the relative position within the distribution becomes visible, since faster electrons move to the front, while slower ones stay at the back. In optics, this is referred to as the group delay dispersion, or *chirp*. Note that the initial phase space volume is conserved. This simple relation is only valid for single-electron distributions, as space charge would introduce nonlinear internal forces in dependence on the instantaneous charge density, leading to an additional broadening of the spatial distribution as well as a broadening of the velocity spread. Also, the phase space volume is in general not conserved for dense electron packets.

Remarkably, the vacuum dispersion, which usually broadens an electron pulse, can also be used to compress it, as shown in fig. 2.2 (b). If a phase space distribution is prepared in such a way that the faster electrons are at the back and the slower at the front (i.e. an inverted linear correlation, or chirp, compared to fig. 2.2 (a)), the back catches up with the front at a certain instant in time due to the dispersion.

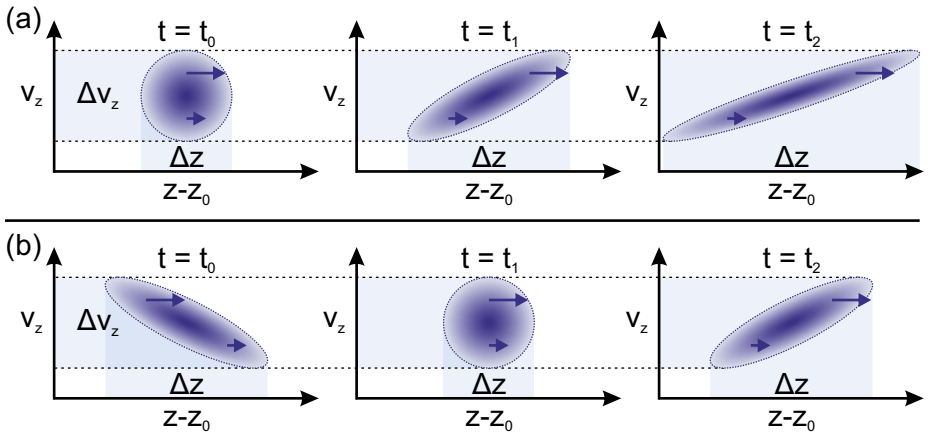

Figure 2.2: Phase space illustration of dispersing single-electron pulses. The position axis is shifted to the center of the distribution, z_0. The blue arrows represent different velocities. (a) An initially uncorrelated phase space disperses due to the velocity spread, Δv_z, leading to a broadening of the spatial distribution, Δz. The dispersion produces a linear position-dependence of the velocity, faster electrons being moved to the front of the distribution, while the phase space volume is conserved. (b) A phase space initially correlated for compression, slower electrons being at the front, compresses itself at a certain point in time, at which the trailing fast electrons catch up with the slow front, and then broadens again.

This instant of least correlation, or zero chirp, yields the smallest spatial and hence temporal distribution and is therefore referred to as the temporal focus. After this, the dispersion broadens the spatial distribution again as in fig. 2.2 (a). This dispersive nature of electron distributions prohibits maintaining a constantly short pulse duration over an extended propagation distance, unless for a very small velocity spread or at highly relativistic velocities, and therefore the temporal focus needs to be carefully matched with the sample's position. For an ideally linear velocity distribution as in fig. 2.2 (b), defined as $v_z(z) = v_0 - (z - z_0)\,\Delta v_z/\Delta z$, v_0 being the central velocity, the time it takes for the faster electrons at the back to catch up with the front simply follows from eqn 2.5 as $t_f = \Delta z/\Delta v_z$. The distance f from the distribution's center, z_0, to the temporal focus is therefore given by:

$$f = v_0 t_f = v_0 \frac{\Delta z}{\Delta v_z} \tag{2.7}$$

Preparing a phase space distribution with an inverted chirp with respect to the electron's normal dispersion in vacuum, as shown in fig. 2.2 (b), requires manipulation of the electron pulse's phase space by means of external electric fields. This concept of chirp reversal for electron pulse compression by energy (or velocity) modulation with microwave fields is discussed in the next chapter.

Chapter 3

Compression of single-electron pulses with microwave fields

UED experiments are based on the pump-probe technique (cf. sections 1.1 and 1.4), using laser pulses to excite ultrafast structural dynamics and electron pulses to record snapshots of the transient structure via diffraction. Therefore, the synchronization between the laser pump pulses and the electron probe pulses is crucial in order to assign the exact timing to a particular acquisition relative to the initiating pump pulse, especially when exposures are integrated over many consecutive pump-probe cycles, e.g. in the case of single-electron or few-electron pulses. While this synchronization is naturally maintained in all-optical pump-probe experiments (i.e. driven by the same laser source), the optically triggered generation of electron pulses, their dispersion, and especially their interaction with electric and magnetic fields can deteriorate the synchronization to the laser pump pulses and hence degrade the temporal resolution of the experiment. In the case of single-electron pulses, these effects broaden their temporal distribution with respect to the laser pulses (cf. fig. 2.1), even if the electron pulse's intrinsic duration is short [81].

In this work, an oscillating electric field inside a resonant cavity at microwave frequencies is used for dispersion control of single-electron pulses. This technique allows manipulation of the electron pulse's phase space in the energy domain in order to prepare a velocity distribution suitable for subsequent self-compression (cf. fig. 2.2 (b)). Moreover, the conservation of phase space volume in the absence of space charge allows achieving almost arbitrarily short single-electron pulses at the expense of according energy broadening. However, the synchronization between the microwave's phase and the laser pulses poses the most intricate technological challenge in advancing the temporal resolution of UED into the few-femtosecond or attosecond domain by compression of single-electron pulses with microwave fields.

3.1 Dispersion control of single-electron pulses

As pointed out in section 1.4, static electric or magnetic fields can be employed to introduce reversed dispersion in relation to vacuum's dispersion, thus delaying faster electrons with respect to the slower ones [91, 108–110]. These principles rely on spatially separating electrons of different velocities and forcing the faster ones to propagate over a longer distance before being spatially recombined again. This is similar to dispersion management and pulse compression in optics based on prisms [120], gratings [121], or chirped mirrors [122]. Although these methods are in principle suitable to reshape the electron pulse's phase space for subsequent self-compression (cf. fig. 2.2 (b)), the shortest achievable pulse duration at the temporal focus, i.e. the instant of zero chirp, cannot go below the initial duration of photoemission, which is defined by the laser pulse's duration, owing to the conservation of phase space volume.

Using time-dependent rather than static (conservative) fields, a net momentum transfer to the electrons can be achieved. For a longitudinal time-dependent electric field, $\mathcal{E}_z(t)$, the momentum transferred to an electron after propagation through the field is given by:

$$\Delta p_z = e \int_{\tau} \mathcal{E}_z(t)\ \mathrm{d}t, \tag{3.1}$$

e being the elementary charge and τ the duration of the interaction with the field. A linear time dependence therefore imprints a linear momentum transfer on the phase space as a function of the electron's position within the distribution. This can be used to reverse the chirp acquired during dispersion by slowing down the leading electrons, while accelerating the trailing ones, instead of merely delaying the faster electrons, as in the case of static fields. Moreover, the chirp can be overcompensated by choosing a steeper temporal slope of the field, leading to an increased bandwidth and therefore a shorter pulse duration at the temporal focus than at the photocathode, since the phase space volume is conserved in the absence of space charge.

Time-dependent electric fields thus provide complementary phase space control of single-electron pulses: Dispersive elements, e.g. static fields or free propagation in vacuum, manipulate the temporal (or spatial) distribution of the single-electron pulse's phase space, while maintaining a constant bandwidth; in contrast, time-dependent fields manipulate the energy (or momentum) distribution, while not altering the temporal distribution, provided a short interaction time with the fields. Combining both, a complete phase space control is possible, while conserving the phase space volume – the pulses can be made arbitrarily short at the expense of increased bandwidth, or arbitrarily monochromatic at the expense of according temporal broadening, limited only by quantum uncertainty. Note that independent ma-

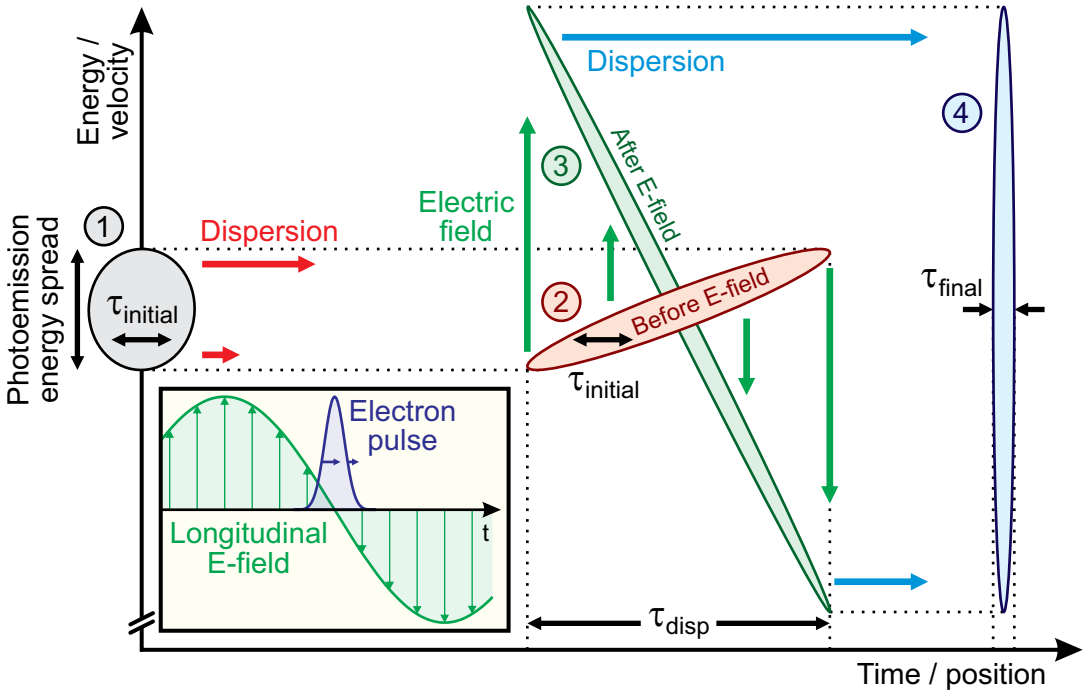

Figure 3.1: Concept of single-electron pulse compression with time-dependent longitudinal electric fields [81]. The velocity coordinate of the phase space diagram can also be interpreted as energy when considering small relative velocity spreads and the position coordinate can be directly interpreted as time. Immediately after photoemission (1), the phase space is uncorrelated, having a temporal spread of $\tau_{initial}$. After free propagation, dispersion broadens the distribution (2) to a duration of τ_{disp} and imprints a linear chirp. The time-dependent longitudinal electric field is set such that the electrons at the front are slowed down (energy loss), while the trailing electrons are accelerated (energy gain), thus inverting and overcompensating the chirp (3). The dispersion during subsequent propagation then leads to self-compression (4). Note that the excess energy spread imprinted by the field results in a final duration of τ_{final}, which is shorter than the initial duration, since the phase space volume is conserved. The finite duration of static acceleration after photoemission is ignored here. The inset shows a practical realization of the time-dependent electric field, using the nearly linear time dependence of an oscillating microwave field around the zero crossing, provided an oscillation period which is substantially longer than τ_{disp}.

nipulation of the electron pulse's phase space in the temporal and energy domain is in general impossible in the presence of space charge, since the internal Coulomb forces broaden the phase space both temporally and energetically at the same time.

Fig. 3.1 demonstrates single-electron pulse compression below the initial duration of photoemission using longitudinal electric fields with a linear time dependence. Here, the initial phase space distribution (1) is shown assuming an instantaneous acceleration to the final energy after photoemission, i.e. the finite acceleration time inside the static electric field at the photocathode, which leads to a slightly curved

shape of the phase space, is neglected. After free propagation, dispersion temporally broadens the pulse (τ_{disp}), leading to a linear chirp (2). The temporal slope of the longitudinal electric field is set to slow down the fast electrons at the front and to accelerate the trailing slow electrons, as illustrated in the inset. The temporal distribution is nearly unchanged after the interaction with the field; however, the chirp is inverted and overcompensated, yielding an increased bandwidth (3). The subsequent propagation leads to self-compression at a temporal focus in the same way as in fig. 2.2 (b) with the notable difference that the final duration, τ_{final}, at the temporal focus is shorter than the initial duration, τ_{initial}, due to the increased bandwidth, since the phase space volume is conserved (4). If the longitudinal electric field is linear with time and exactly correlated to the center of the phase space, the reduction of the pulse duration at the temporal focus with respect to the initial pulse duration at the photocathode corresponds to the relative increase in bandwidth:

$$\tau_{\mathrm{final}} = \tau_{\mathrm{initial}} \frac{\Delta v_{\mathrm{initial}}}{\Delta v_{\mathrm{final}}} \approx \tau_{\mathrm{initial}} \frac{\Delta E_{\mathrm{initial}}}{\Delta E_{\mathrm{final}}}, \tag{3.2}$$

$\Delta v_{\mathrm{initial}}$, $\Delta v_{\mathrm{final}}$, $\Delta E_{\mathrm{initial}}$, and $\Delta E_{\mathrm{final}}$ being the initial and final velocity and energy spread, respectively. Since the relation between energy and velocity is nonlinear (cf. eqns 2.1 and 2.2), the simple proportionality in eqn 3.2 is only valid for a small relative bandwidth, which is true for UED, typical relative bandwidths being in the range of 10^{-5}–10^{-3}, even after compression with longitudinal electric fields. At relativistic velocities, the dispersion in vacuum is very small and therefore the distance to the temporal focus can become impractically long, necessitating additional dispersive elements for temporal compression after the interaction with the longitudinal electric field.

Modeling the dispersion during the static acceleration within the region between photocathode and anode (which is neglected in fig. 3.1) is essential for an estimation of the uncompressed pulse duration, τ_{disp}. Without any compression technique, this limits the temporal resolution of UED experiments. After acceleration in a static field, $\mathcal{E}_{\mathrm{acc}}$, an initial longitudinal velocity spread of Δv_z at the photocathode leads to a temporal spread according to the non-relativistic equation of motion:

$$\tau_{\mathrm{acc}} \approx \frac{m_{\mathrm{e}} \Delta v_z}{e \mathcal{E}_{\mathrm{acc}}} \tag{3.3}$$

Note that the initial temporal spread of the photoemission (essentially the laser pulse's duration) broadens the duration of the dispersed pulse, which is a convolution between the initial and the purely dispersive temporal spread (for Gaussian-like distributions):

$$\tau_{\mathrm{disp}}^2 = \tau_{\mathrm{initial}}^2 + \tau_{\mathrm{acc}}^2 \tag{3.4}$$

Since the simple model in eqn 3.3 only calculates the time difference between electrons with initial velocities of zero and Δv_z, the particular shape of the initial velocity distribution significantly affects the resulting temporal distribution. Different models exist correlating the energy bandwidth at photoemission to a certain longitudinal velocity spread and according temporal spread, τ_{acc}, after acceleration [78, 80, 82, 100, 114], based on different assumptions about the photoemission process. Despite this theoretical uncertainty, it is evident from eqn 3.3 that minimizing the bandwidth at photoemission, e.g. by matching the laser's wavelength to the photocathode's work function [82], produces the shortest pulses. However, the optical Fourier limit dictates that the achievable laser pulse's duration increases when reducing its bandwidth and thus temporally broadens the electron pulse (cf. eqn 3.4). Increasing the acceleration field, $\mathcal{E}_{\mathrm{acc}}$, can also reduce the dispersion (cf. eqn 3.3). This is limited for static acceleration by vacuum breakdown to about 10 kV/mm (cf. section 1.4); therefore, a minimum single-electron pulse's duration of about 70 fs FWHM is predicted at this acceleration field when using bandwidth-limited 40 fs laser pulses, being a trade-off between narrow bandwidth and short duration, and tuning the laser's wavelength close to the photocathode's work function [82].

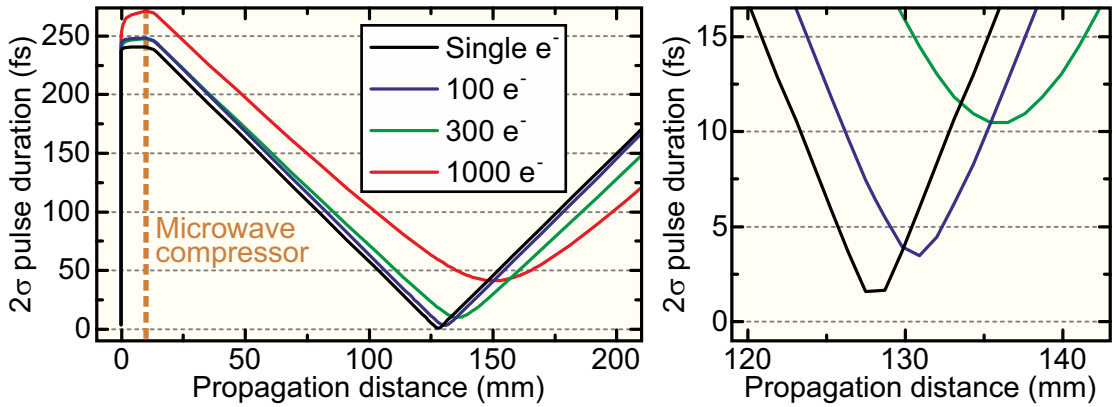

Figure 3.2: Simulation of electron pulse propagation with static acceleration followed by compression with longitudinal microwave fields; data taken from [80]. The 2σ pulse duration denotes two standard deviations of the temporal distribution. After photoemission by a 10 fs laser pulse and static acceleration in a field of 4 kV/mm to a kinetic energy of 40 keV, the pulse is compressed by the linear part of a microwave field, transferring energy to the electrons at a rate of 95.5 eV/ps. The subsequent self-compression is linear for single-electron pulses and yields a minimum duration at the temporal focus of ∼1 fs. In the presence of space charge, compression still works; however, the achievable compressed pulse duration deteriorates. Note that the initial broadening after photoemission occurs mainly within the first micrometers of acceleration. The right panel is a zoom around the temporal focus.

Fig. 3.2 shows a simulated propagation of electron pulses under realistic conditions, including static acceleration and compression with longitudinal microwave

fields, for both the single-electron and space-charge regime (durations denote two standard deviations). A 10 fs laser pulse generates electron pulses with an energy spread of ∼1 eV from a photocathode, which are accelerated in a static field of 4 kV/mm to a kinetic energy of 40 keV. Note that the initial broadening to about 250 fs takes place within the first micrometers of acceleration, while the electrons are still slow. A longitudinal microwave field at 5 GHz is used to interact with the electron pulses over a few millimeters around the zero-crossing phase of the energy modulation. Thus, electrons at the front are slowed down, while trailing ones are accelerated (cf. fig. 3.1). The rate of energy transfer is 95.5 eV/ps. Further details of the simulation can be found in [80]. The linear time dependence of the microwave field leads to linear self-compression due to dispersion during the subsequent free propagation. The simulation yields a duration at the temporal focus of about 1 fs for single-electron pulses. This constitutes a remarkable first proof for the concept of electron pulse compression into the few-femtosecond range or below. At the same time, the requirements for optimizing the photoemission bandwidth and acceleration field are largely relaxed, allowing operation at technically convenient conditions.

The presence of space charge causes nonlinear and non-conservative transformations of the phase space, thus limiting the achievable compressed pulse's duration. In addition, the distance to the temporal focus increases with increasing space charge because Coulomb repulsion grows near to the temporal focus, retarding the process of compression. Nevertheless, pulses consisting of up to a few hundred electrons can be compressed into the few-femtosecond range.

3.2 The microwave cavity

The concept for the compression of electron pulses by means of time-dependent electric fields, as pointed out in the previous section, makes certain technically challenging demands concerning the attributes of the employed fields. First, the field needs to be longitudinal, i.e. oriented along the propagation direction of the electron pulses. Secondly, the time dependence must be linear and its slope has to be high enough to compensate the chirp acquired by dispersion and to imprint a certain amount of inverse chirp for a desired temporal focus, according to eqn 2.7. Thirdly, the field must be maintained at constant conditions (i.e. amplitude, direction, and temporal slope) over the entire longitudinal interaction distance as well as over the transverse extent of the electron beam. Homogeneous transient electric fields with a steep linear time dependence are usually employed in streak cameras (cf. section 1.2), though in the transverse direction. For electron pulse compression, the concept of a longitudinal streak camera needs to be employed.

Here, we exploit the on-axis electric field of the TM_{010} mode oscillating at microwave frequencies inside a resonant cavity. For the simplest cavity shape, a hollow cylinder of a conducting material, also referred to as a pill-box cavity, standing-wave solutions of Maxwell's equations yield modes of different shapes and resonance frequencies. They are categorized as transverse electric (TE) or transverse magnetic (TM) modes, meaning that either the electric or magnetic field, respectively, has no longitudinal component, i.e. is entirely transverse. In cylindrical coordinates (r, ϕ, z), their geometrical shapes are further characterized by three indices, TE_{mnp} or TM_{mnp}, respectively, where m is the number of azimuthal full-period variations, n the number of radial zero crossings, and p the number of longitudinal half-period variations of the field components. Thus, m, n, and p quantify the number of nodes of the field distribution along orthogonal directions in cylindrical coordinates. By definition, only TM modes provide a nonzero longitudinal component of the electric field, the TM_{010} mode being the simplest solution of Maxwell's equations. This mode consists of a longitudinal electric field, $\mathcal{E}_z$, and an azimuthal magnetic field, H_ϕ, both being independent of the longitudinal coordinate z, while all other field components are zero:

$$\mathcal{E}_z(r,t) = \mathcal{E}_0 J_0(k_r r)\cos(\omega_0 t) \equiv \mathcal{E}_{0,z}(r)\cos(\omega_0 t), \tag{3.5}$$

$$H_\phi(r,t) = \sqrt{\frac{\epsilon_0}{\mu_0}}\mathcal{E}_0 J_1(k_r r)\sin(\omega_0 t) \equiv H_{0,\phi}(r)\sin(\omega_0 t), \tag{3.6}$$

$\mathcal{E}_0$ being the electric field amplitude, ϵ_0 and μ_0 the permittivity and permeability of vacuum, respectively, $\omega_0 = 2\pi f_0$ the resonant angular frequency (f_0 being the resonant frequency), J_i the i-th order Bessel function of the first kind, and k_r the radial wave number. $\mathcal{E}_{0,z}(r)$ and $H_{0,\phi}(r)$ describe the radial dependence of the electric and magnetic field amplitude, respectively. For a pill-box cavity with radius R and perfectly conducting walls, the resonant boundary condition at the walls requires $\mathcal{E}_z(R,t) = 0$ and therefore $J_0(k_r R) = 0$. This implies $k_r \approx 2.405/R$ (the first root of J_0 being approximately at 2.405) and thus the resonance frequency is given by:

$$\omega_0 = k_r c \approx \frac{2.405c}{R} \tag{3.7}$$

For example, a pill-box cavity with a radius of 2 cm has therefore a resonance frequency, f_0, of about 6 GHz. Electrons can interact with the electric field inside the cavity by adding small entrance and exit holes to the cavity's walls on the axis, which only negligibly perturb the field distribution. The mode inside the cavity is excited by applying an RF signal via a coaxial cable or waveguide which is coupled via an antenna (i.e. a thin wire) inside the cavity to the mode. Usually, magnetic

coupling is used, for which the antenna is formed into a current loop perpendicularly to the magnetic field lines and positioned radially at the maximum of the magnetic field amplitude (see fig. 3.3 (a)). Coupling to the electric field is unfavorable, as the antenna would have to be placed close to the axis in that case and thus would interfere with the electron beam. TM_{010} cavities are used in almost all RF particle accelerators, hence a rigorous cavity theory can be found in many accelerator textbooks [106, 123].

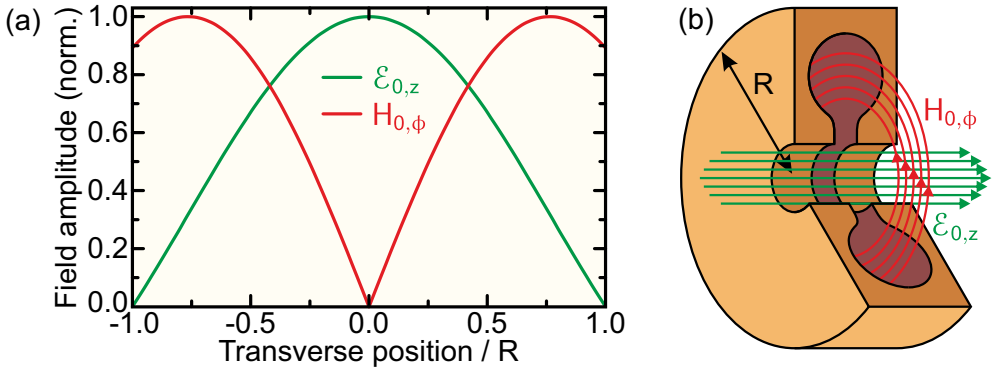

Figure 3.3: Field profiles of the TM_{010} mode of an ideal pill-box cavity and illustration of an optimized omega-shaped cavity. (a) Transverse profile of the normalized field amplitudes $\mathcal{E}_{0,z}(r)$ (electric field) and $H_{0,\phi}(r)$ (magnetic field), essentially the Bessel functions J_0 and J_1, in units of the pill-box cavity's radius R. (b) The toroidal omega-shaped cavity design concentrates the electric field on the axis, maximizing the field strength, and reduces the surface-to-volume ratio for the volume enclosed by the magnetic field, minimizing the losses due to eddy currents in the walls.

The radial field profiles of the TM_{010} mode of a pill-box cavity are shown in fig. 3.3 (a). The magnetic field is nonzero at the cavity's walls and therefore induces eddy currents, since it is oscillating. This results in ohmic losses due to the finite conductivity of the material which the cavity is made of (e.g. copper). In order to maintain a certain amplitude of the oscillating electric field, determined by the velocity of the electrons and the desired distance to the temporal focus, these losses have to be compensated by the RF source feeding the cavity. The RF power which is directly obtained from typical primary RF sources, e.g. oscillators or photodiodes, (milliwatts at microwave frequencies) is insufficient for electron pulse compression; hence, further amplification is required (see section 5.2). High amplification poses a technical challenge and introduces additional noise which translates into timing jitter (see section 3.3); thus, a power-efficient cavity design is crucial. The simple cylindrical pill-box cavity is not ideal in this respect [124]. In an optimized design, the shape is modified by narrowing the cavity longitudinally around the axis within the electric field region. Thus, the capacitance is increased around the axis, leading to an increased electric field and stored electric energy there. Furthermore, the losses are

reduced if the surface integral of the magnetic field, which induces the eddy currents that lead to ohmic losses, is minimized. This requires the smallest possible surface-to-volume ratio of the part of the cavity within the magnetic field region (i.e. away from the axis), while maintaining the correct radial size for the desired resonance frequency. A sphere has the smallest surface-to-volume ratio; however, because of the narrow region around the axis, the optimum shape is a toroid with an elliptical cross-section [124]. This design is referred to as an "omega-shaped" cavity, since the cross-section resembles the letter Ω [80, 81, 125]. Fig. 3.3 (b) illustrates the shape and the field distribution of such a cavity with an (exaggerated) axial aperture for the electrons to interact with the electric field.

The losses of the cavity can be described in analogy to an electric circuit of lumped elements, representing the cavity's ohmic resistance, inductance, and capacitance. A series or parallel connection of these three elements are both suitable to model the cavity. For a series connection, the current through all elements is constant, while for a parallel connection the voltage across all elements is constant, which affects the respective contributions of the resistance, inductance, and capacitance to the cavity's losses [126]. However, both approaches yield the same results for the resonance frequency, bandwidth, and phase [126, 127]; therefore, the series connection is chosen here for simplicity. Using Kirchhoff's voltage law results in a differential equation for the time-dependent current response to a voltage driving the circuit. The steady-state solution for an ideal driving voltage, $U(t) = U_0 \cos(\omega t)$, with an amplitude U_0, oscillating at an angular frequency ω, is given by:

$$I(t) = \frac{U_0 \cos(\omega t)}{|Z(\omega)|}, \quad \langle I \rangle_t = \frac{U_0}{\sqrt{2}\,|Z(\omega)|}, \tag{3.8}$$

where $\langle I \rangle_t$ denotes the cycle-averaged root mean square (rms) of the current and $Z(\omega)$ is the complex frequency-dependent impedance:

$$Z(\omega) = R_{\text{cav}} + i\omega L_{\text{cav}} + \frac{1}{i\omega C_{\text{cav}}}, \tag{3.9}$$

R_{cav}, L_{cav}, and C_{cav} denoting the cavity's ohmic resistance, inductance, and capacitance, respectively. Since eqn 3.9 describes a series connection, the respective impedance contributions can be simply summed up in order to obtain the total impedance. A complete derivation can be found in textbooks [127]. The complex cycle-averaged power delivered to the circuit is then given by:

$$P(\omega) = |\langle I \rangle_t|^2 \, Z(\omega) = \frac{U_0^2}{2R_{\text{cav}} + 2i\left(\frac{1}{\omega C_{\text{cav}}} - \omega L_{\text{cav}}\right)} \tag{3.10}$$

It is evident from eqn 3.10 that the delivered power is maximized when the inductive and capacitive impedance cancel out at the resonance frequency:

$$\omega_0 = 2\pi f_0 = \frac{1}{\sqrt{L_{\mathrm{cav}} C_{\mathrm{cav}}}} \tag{3.11}$$

At this frequency, the impedance is purely real, $Z(\omega_0) = R_{\mathrm{cav}}$, thus the power delivered to the circuit is entirely dissipated by ohmic losses. A useful quantity to characterize the quality of a resonant circuit is the dimensionless Q-factor, defined as the energy stored inside the circuit, E_{stored}, divided by the energy loss per cycle, E_{loss}:

$$Q_0 = 2\pi \frac{E_{\mathrm{stored}}}{E_{\mathrm{loss}}} = \omega_0 \frac{E_{\mathrm{stored}}}{P_{\mathrm{loss}}}, \tag{3.12}$$

where $P_{\mathrm{loss}} = E_{\mathrm{loss}} f_0$ is the cycle-averaged energy loss rate. At resonance, the losses are purely ohmic, thus, according to eqn 3.10, $P_{\mathrm{loss}} = U_0^2 / (2R_{\mathrm{cav}})$. The energy inside the circuit is stored in the magnetic field produced by the current through the circuit, $I(t)$, and in the electric field produced by the voltage across the capacitor, $U_{\mathrm{c}}(t)$:

$$E_{\mathrm{stored}} = \frac{1}{2} L_{\mathrm{cav}} \left| I(t) \right|^2 + \frac{1}{2} C_{\mathrm{cav}} \left| U_{\mathrm{c}}(t) \right|^2 \tag{3.13}$$

Since the current through each element of the series circuit is given by eqn 3.8, the voltage across the capacitor follows as:

$$U_{\mathrm{c}}(t) = \frac{1}{C_{\mathrm{cav}}} \int I(t)\, \mathrm{d}t = \frac{U_0}{\omega \left| Z(\omega) \right| C_{\mathrm{cav}}} \sin \omega t \equiv U_{0,\mathrm{c}}(\omega) \sin \omega t \tag{3.14}$$

Substituting eqns 3.8 and 3.14 in eqn 3.13 and using eqn 3.11 and the identity $Z(\omega_0) = R_{\mathrm{cav}}$ at the resonance frequency ($\omega = \omega_0$) yields for the stored energy:

$$E_{\mathrm{stored}} = \frac{U_0^2 L_{\mathrm{cav}}}{2R_{\mathrm{cav}}^2} \cos^2 \omega_0 t + \frac{U_0^2}{2\omega^2 R_{\mathrm{cav}}^2 C_{\mathrm{cav}}} \sin^2 \omega_0 t = \frac{U_0^2 L_{\mathrm{cav}}}{2R_{\mathrm{cav}}^2} \tag{3.15}$$

Here, the identity $\cos^2 \phi + \sin^2 \phi = 1$ is used. Note that the inductive energy is equal to the capacitive energy at resonance. Together with P_{loss} at resonance, the Q-factor[1] in eqn 3.12 can be then expressed in terms of ohmic resistance, inductance, and capacitance of the cavity:

$$Q_0 = \omega_0 \frac{L_{\mathrm{cav}}}{R_{\mathrm{cav}}} = \frac{1}{\omega_0 R_{\mathrm{cav}} C_{\mathrm{cav}}} \tag{3.16}$$

[1] Note that this definition of the Q-factor applies to a series connection. For a parallel connection, the Q-factor is inverted: $Q_0 = R_{\mathrm{cav}} / (\omega_0 L_{\mathrm{cav}}) = \omega_0 R_{\mathrm{cav}} C_{\mathrm{cav}}$ [126].

For the second equality in eqn 3.16, the identity in eqn 3.11 at resonance is used. The voltage across the capacitor which is formed by the cavity's shape around the axis, $U_\mathrm{c}(r,t)$, is of particular interest for accelerating electrons, since it is related to the magnitude of the longitudinal electric field of the TM_{010} mode (cf. eqn 3.5) according to:

$$U_\mathrm{c}(r,t) = \int_d \mathcal{E}_z(r,z,t)\ \mathrm{d}z, \tag{3.17}$$

d being the longitudinal on-axis distance between the cavity's walls (i.e. its thickness). Note that for an optimized cavity design deviating from the cylindrical (pillbox) shape and a wall material with finite conductivity, the amplitude of $\mathcal{E}_z$ is in general not constant along the longitudinal z-direction inside the cavity. A useful figure of merit concerning the power efficiency of a cavity is the corresponding shunt resistance[2], R_s, which relates the voltage amplitude across the capacitor (cf. eqn 3.14), $U_{0,\mathrm{c}}$, to the cycle-averaged input power at resonance (cf. eqn 3.10), using the identity in eqn 3.11:

$$R_\mathrm{s} = \frac{U_{0,\mathrm{c}}^2}{P_\mathrm{loss}} = 2\frac{L_\mathrm{cav}}{R_\mathrm{cav}C_\mathrm{cav}}, \tag{3.18}$$

This quantity describes the input power required for a maximum energy transfer of (ideally) $eU_{0,\mathrm{c}}$ to the electrons. Note that the factor of 2 is sometimes omitted in literature, depending on whether the amplitude, $U_{0,\mathrm{c}}$, or the cycle-averaged rms value of the voltage across the capacitor, $U_{0,\mathrm{c}}/\sqrt{2}$, is considered.

The power absorbed by the cavity (cf. eqn 3.10) as a function of frequency, normalized to the maximum at resonance, can be expressed in terms of the Q-factor:

$$\begin{aligned}\Re\left[\frac{P(\omega)}{P(\omega_0)}\right] &= \frac{1}{1+\left(\frac{1}{\omega R_\mathrm{cav}C_\mathrm{cav}} - \omega\frac{L_\mathrm{cav}}{R_\mathrm{cav}}\right)^2} = \frac{1}{1+\left(Q_0\left[\frac{\omega_0}{\omega}-\frac{\omega}{\omega_0}\right]\right)^2} \\ &= \frac{1}{1+\left(Q_0\left[\frac{(\omega+\omega_0)\Delta\omega}{\omega\omega_0}\right]\right)^2} \approx \frac{1}{1+\left(2Q_0\frac{\Delta\omega}{\omega_0}\right)^2}\end{aligned} \tag{3.19}$$

Here, Q_0 from eqn 3.16 is substituted and $\Delta\omega = \omega - \omega_0$ is used. The last identity in eqn 3.19 is valid around the resonance frequency ($\omega \approx \omega_0$) and for high Q-factors ($Q_0 \gg 1$). Therefore, the absorbed power can be approximated by a Lorentzian around the resonance frequency. It follows from eqn 3.19 that the Q-factor is closely related to the cavity's bandwidth, since its FWHM is given by:

$$\Delta\omega_\mathrm{FWHM} = \frac{\omega_0}{Q_0} = \frac{2\pi f_0}{Q_0} \tag{3.20}$$

[2] In the same way as for the Q-factor, this definition for the shunt resistance applies to a series connection. For a parallel connection, $R_\mathrm{s} = 2R_\mathrm{cav}$ [126].

Similarly to eqn 3.19, the phase of the complex power delivered to the circuit is given by:

$$\phi(\omega) = \arctan \frac{\Im\left[P(\omega)\right]}{\Re\left[P(\omega)\right]} \approx \arctan\left(2Q_0 \frac{\Delta\omega}{\omega_0}\right) \tag{3.21}$$

The parameters of the microwave cavity used in this work have been chosen according to the requirements for efficient compression of electron pulses at energies around 30 keV. A high Q-factor is desirable, since it provides a higher stored energy and compression field for a particular input power (cf. eqns 3.12, 3.13, and 3.17). However, this comes at the expense of a reduced bandwidth (cf. eqn 3.20), which limits the range of usable frequencies, e.g. for synchronization with the laser's repetition rate (see chapter 4). Also, the slope of the phase with respect to frequency depends on the bandwidth (cf. eqn 3.21) and therefore a frequency drift of the input signal translates into a severe phase or timing drift of the intra-cavity field for very high Q-factors (see section 3.3).

A similar trade-off applies to the choice of the resonance frequency. The temporal slope of the longitudinal electric field increases with frequency at a given amplitude. Also, the requirements for the phase synchronization of the RF source to the laser's repetition rate are relaxed, since a higher amount of phase jitter (in degrees) is acceptable to maintain the same timing jitter (in femtoseconds) at higher frequencies. However, linear manipulation of the electron pulse's phase space, as described in section 3.1, requires a linear time dependence of the electric field. For a sinusoidal microwave field, this holds only if the period is much larger than the temporal spread of the electron pulses interacting with the field and poses a fundamental upper limit for usable frequencies. As the dimensions of the TM_{010} mode scale inversely with the resonance frequency (cf. eqn 3.7), transverse inhomogeneities of the field distribution become more severe for a particular diameter of the electron beam (limited by its emittance, cf. section 2.1) and accurate machining becomes challenging for very small cavity dimensions. Finally, low-noise high-performance electronics (amplifiers, filters, etc.) for very high frequencies are less available and more expensive than components used for common telecommunication and radar applications within the standard microwave bands.

Considering these requirements, the microwave cavity used in this work has been designed for a resonance frequency of 6.2 GHz (lying in the IEEE C-band) and a bandwidth of about 2 MHz FWHM ($Q_0 = 3100$) and manufactured by the Budker Institute of Nuclear Physics (Novosibirsk, Russia) [81]. The cavity is made of copper and has an omega-shaped design with an on-axis thickness of 3 mm and a central aperture of 2 mm for the electron beam. Thus, the propagation time through the longitudinal field region is about 30 ps, extending significantly beyond the linear part of the field. However, according to eqn 3.1, the momentum transferred to an electron

has the same periodicity with the time when it enters the cavity as the oscillation of the electric field. Therefore, only the electron pulse's duration in relation to the microwave's period is essential for a linear compression, rather than the absolute propagation time through the cavity.

In addition to the input coupling antenna, a second probe antenna allows online monitoring of the amplitude and phase of the field inside the cavity, e.g. for synchronization purposes, while the power extracted by the probe antenna (−60 dB of the input power) is negligible. The resonance frequency can be tuned over a range of ∼100 MHz by inserting a pin into the cavity, effectively reducing its volume; fine tuning is achieved by temperature control, the coefficient being about −0.1 MHz/K. The shunt resistance (cf. eqn 3.18) is on the order of 2 MΩ, which allows setting the temporal focus for 30 keV electrons at about 20 cm after the cavity using well below 1 W of microwave power. At the same time, the bandwidth is high enough for reasonable synchronization with our laser system (see section 4.3).

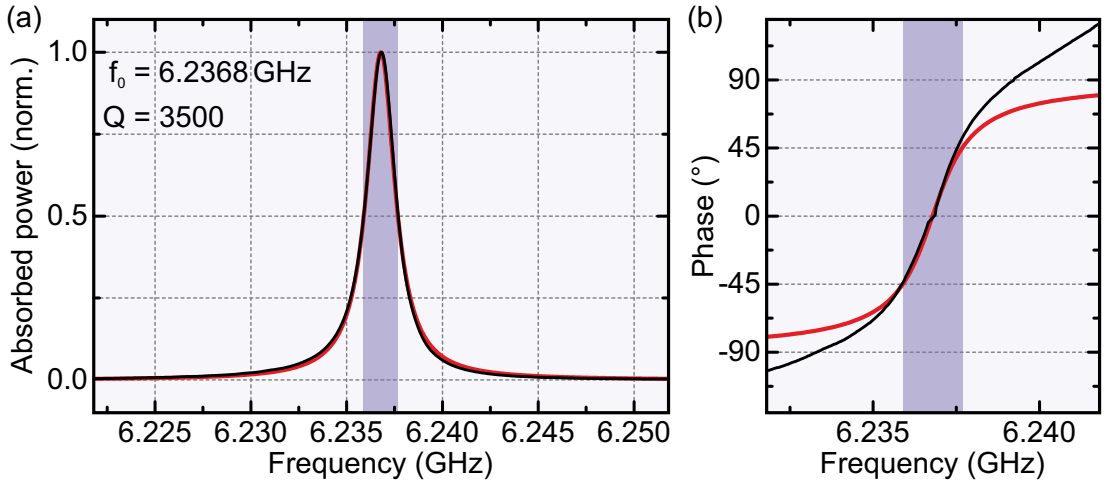

Figure 3.4: Absorption and phase of the microwave cavity. (a) Measured absorption curve of the cavity (black line) and fitted Lorentzian profile (red line) according to eqn 3.19. The resonance frequency is at 6.2368 GHz and the Q-factor is 3500, yielding a bandwidth of 1.78 MHz FWHM. (b) The measured phase of the cavity (black line) and calculated phase (red line) according to eqn 3.21 using the fitted parameters from (a). The phase slope at the resonance frequency is 64.3 °/MHz. The purple areas mark the FWHM bandwidth in both graphs.

Fig. 3.4 shows the measured power absorption and phase together with theoretical curves from eqns 3.19 and 3.21. The absorption in fig. 3.4 (a) is determined by measuring the power at the output (probe) port of the cavity, while sweeping the frequency of a microwave source at the input port at a constant power (black line). The data is fitted by a Lorentzian (red line), which yields a resonance frequency, f_0, of 6.2368 GHz and a Q-factor of 3500. This corresponds to a bandwidth of 1.78 MHz FWHM according to eqn 3.20. The phase in fig. 3.4 (b) is measured in a similar

way (black curve); however, the signal from the microwave source is split in two parts, one of which is fed into the cavity. The cavity's output is then mixed with the other part of the original signal in a well-characterized double-balanced mixer. The voltage at the output of such a mixer is proportional to the phase difference between the signals at its two inputs. The phase (red curve), calculated according to eqn 3.21 using the fitted values from fig. 3.4 (a), fits well to the measurement within the FWHM bandwidth but deviates significantly outside the bandwidth. The mixer's calibration fails there because of the rapidly decreasing output signal's amplitude. Imperfect impedance matching between the cavity and the source can also cause deviations from the ideal curves for both the absorption and the phase. Nevertheless, the measured phase shows the characteristic 90° flip over the FWHM bandwidth and a slope at the resonance frequency of 64.3 °/MHz.

3.3 Limits of temporal resolution and jitter

The general principle of phase space control with time-dependent electric fields, as pointed out in section 3.1, promises single-electron UED with potentially attosecond temporal resolution. However, technological constraints both in the transverse (spatial) and longitudinal (temporal) domain broaden the spatiotemporal confinement of the electron pulses and thus limit the temporal resolution of UED pump-probe experiments. Addressing these technological challenges and minimizing their contributions to temporal broadening is therefore crucial for ultimate resolutions.

Broadening in the transverse domain is related to the electron beam's diameter and divergence. The ideal manipulation of the electron pulse's longitudinal phase space, as shown in fig. 3.1, requires the longitudinal position and velocity distributions (Δz and Δv_z) to be constant over the transverse plane (i.e. along the x- and y-directions). Radially inhomogeneous electric and magnetic fields bend the pulse front, since the amount of momentum transferred from such fields to the electrons varies as a function of distance from the axis. Every component for beam steering or shaping introduces more or less pronounced transversely inhomogeneous fields, especially focusing or defocusing components, such as the anode hole and magnetic lenses [105]. The longitudinal electric field of the microwave cavity has a radial dependence (cf. fig. 3.3 (a)). Also, only the linear part of the microwave around the zero-crossing phase is used for compression, where the azimuthal magnetic field is strongest and acts as a transversely defocusing lens. In general, beam divergence or convergence leads to temporal broadening: For a constant magnitude of the velocity across a non-collimated beam, which is true e.g. after a magnetic lens, the pulse front is bent. In contrast, a straight pulse front requires a radially inhomogeneous

magnitude of the velocity for a non-collimated beam, which leads to inhomogeneous interactions with electric and magnetic fields.

Transverse inhomogeneities deteriorate the temporal resolution because the diffraction pattern is collected from the entire volume of interaction between the electron beam and the sample. A correlation of the electrons at the detector to their lateral position at the sample is impossible. Therefore, a longitudinal displacement of the electrons across the beam profile at the instant when structural dynamics are initiated by the pump pulse translates into a temporal delay, thus broadening the temporal confinement of the diffraction snapshot. A common strategy to reduce transverse inhomogeneities is to minimize emittance and to employ the smallest possible collimated beam diameter. The influence of inhomogeneous fields can be reduced by using large field sources (e.g. for magnetic steering of the beam) or large mode areas (e.g. the size of the TM_{010} mode), minimizing the variation of the field across the electron beam's diameter. The temporal distortions introduced by transverse inhomogeneities of magnetic lenses or the anode hole are typically on the order of 10 fs [80, 105]. They can be in principle compensated by an "isochronic" operation of the magnetic lens (or lenses), at which a temporal focus, i.e. an instant of minimized or zero transverse distortions, exists and coincides with the spatial focus (see section 8.3). Transverse distortions from the fields of a compression cavity can also be compensated in the same way, providing the ability to focus the electron beam simultaneously in space and time [105].

Longitudinal broadening can arise from such interactions with fields which result in a nonlinear relation between the longitudinal position and velocity, i.e. a nonlinear chirp. A nonlinearly shaped phase space at the entrance of the compression cavity gives rise to an effectively reduced compression ratio, which can be in principle compensated at the expense of a higher velocity spread required for compression compared to linearly chirped electron pulses of the same duration. This is the case for the static acceleration after photoemission, since electrons of initially different velocities spend a different amount of time inside the accelerating field. It is also true for the interaction with the longitudinal electric field of a compression cavity; however, the relative longitudinal velocity spread after the static acceleration (on the order of 10^{-6}) is negligible and so is the difference in interaction time with the field inside the cavity. Furthermore, the relative velocity spread gained inside the cavity during propagation (typically on the order of 10^{-4}) is negligible for reasonable compression ratios. Likewise, a nonlinear time dependence of the microwave field deteriorates the compression. At 6.2 GHz, the period of the microwave field is 161 ps and the deviation from linearity for a 1 ps electron pulse entering the cavity around the zero-crossing phase is $\sim 10^{-4}$, implying a timing deviation of 100 as at the temporal focus and proportionally less for shorter incoming pulses.

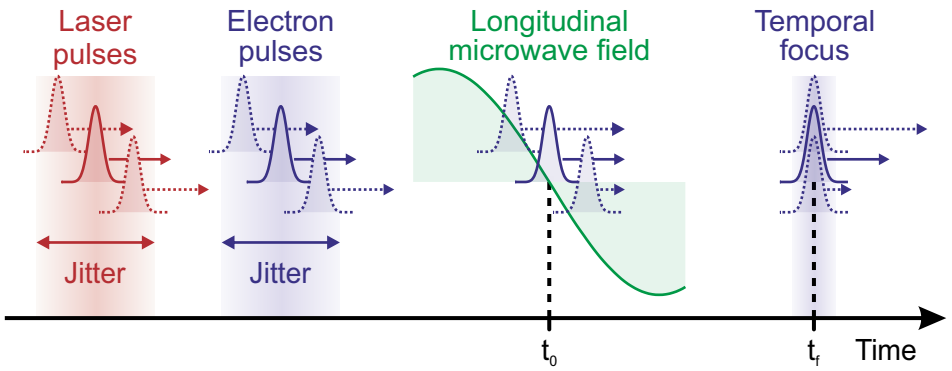

Figure 3.5: Illustration of timing jitter between the laser's repetition rate and the microwave's phase. The timing of the laser pulses relative to the microwave's zero-crossing phase defines the timing of the electrons (within the laser pulse's duration). The momentum transferred from the microwave to the electrons depends on the arrival time at the microwave cavity (t_0). The jitter is thus compensated at the temporal focus (t_f), which is the intended working principle of electron pulse compression with microwave fields. However, the timing of the electron pulses is not correlated to the laser pulses anymore but rather to the microwave's phase. Hence, the temporal resolution of pump-probe experiments involving the laser pulses deteriorates by the amount of timing jitter between the laser pulses and the microwave's phase. Note that the temporal jitter gives rise to an additional velocity spread after the interaction with the microwave field (cf. fig. 3.1).

The most severe contribution to longitudinal broadening is usually timing jitter between the electron pulses and the phase of the microwave field used for compression. The effect of jitter is illustrated in fig. 3.5. The timing of the electron pulse's arrival at the temporal focus is entirely defined by the microwave's phase – this is by definition the concept of electron pulse compression: The electrons gain or lose momentum according to their timing relative to the microwave's zero-crossing phase such that their propagation time to the temporal focus (at a fixed distance) is identical after the interaction with the microwave, regardless of their arrival time at the cavity (cf. section 3.1), as long as the arrival times are distributed over the linear part of the microwave field. If the timing of the laser pump pulses at the sample jitters with respect to the microwave's phase, which defines the timing of the electron probe pulses at the sample, the effective temporal resolution of the pump-probe experiment is compromised, since a diffraction image requires integration over many consecutive pulses. Note that after the interaction with the microwave field a distinction between the intrinsic duration of the electron pulse, defined by the laser pulse's duration at the instant of photoemission and subsequent dispersion (cf. sections 2.1 and 2.2), and the temporal broadening due to jitter between laser and microwave is impossible for single-electron pulses. In a phase space plot defined relative to the microwave's zero-crossing phase (cf. fig. 3.1), this is equivalent to electron pulses which

are initially broadened in time with the consequence of an accordingly increased velocity spread after the interaction with the microwave field. Such a broadened pulse would still be compressed with respect to the microwave's zero-crossing phase, as shown in fig. 3.5, yet lose its synchronization with the laser pump pulse.

A certain amount of timing jitter between the laser pulses and the microwave's phase is always present because any synchronization scheme suffers from electronic noise (see section 4.1) which translates into phase noise and therefore timing noise of the microwave's phase with respect to the laser's repetition rate. At 6.2 GHz, a synchronization with a relative period jitter of $6 \cdot 10^{-6}$ or a phase jitter of 40 µrad is required in order to maintain a temporal resolution of 1 fs. The next chapter is dedicated to the challenge of reducing the phase noise and thus enhancing the quality of synchronization between laser and microwave.

Additionally, systematic timing drifts between the laser pulses and the microwave's phase compromise the temporal long-term stability of single-electron UED pump-probe experiments which require long acquisition times on the order of minutes to hours (cf. section 1.3). They usually arise from fluctuations of the environmental conditions, such as mechanical vibrations, temperature drifts, or fluctuating external electric and magnetic fields. Tiny mechanical displacements of the laser's optical components due to vibrations at acoustic frequencies lead to fluctuations of the delay between the laser pulses and the microwave. Fluctuating external fields, especially magnetic fields, e.g. from power lines or elevators, have to be considered and properly shielded or compensated, since they can deflect electrons and thus distort their spatial and temporal distributions. Slower temperature drift causes not only displacements and according delays similar to mechanical vibrations, but also changes of the cavity's dimensions and therefore its resonance frequency, which changes the phase of the microwave inside the cavity according to eqn 3.21. This requires a temperature stabilization of our cavity (cf. section 3.2) to about 0.4 mK for a timing drift of 1 fs. Likewise, the frequency dependence of the phase implies a maximum allowable frequency drift of the microwave source – due to drift of the laser's repetition rate which the microwave is synchronized to – of about 40 Hz for 1 fs of timing drift. Amplitude fluctuations of the microwave field alter the amount of velocity spread imprinted onto the electrons (cf. section 3.1) and therefore, according to eqn 2.7, the position of the temporal focus. In order to maintain the temporal focus within a distance corresponding to 1 fs at sub-relativistic electron velocities typical for UED, the required stability of the microwave power is about 0.2 %. These requirements, though technologically intricate, are within reach of state-of-the-art stabilization and synchronization systems, paving the way for advancing the temporal resolution of UED into the few-femtosecond domain or below.

Chapter 4

Passive optical enhancement of laser-microwave synchronization

A precise synchronization between the timing of ultrashort laser pulses and the phase of RF signals at microwave frequencies is required for all applications which combine ultrafast optical excitation with the manipulation of charged particles. Apart from dispersion and phase space control of electron pulses for UED, as described in chapter 3, synchronization between optical pulses and microwaves is of highest importance for time-resolved experiments with FEL or synchrotron sources which employ particle accelerators at microwave frequencies [128–130]. Another emerging field of a broad range of applications for laser-microwave synchronization is timing distribution and metrology [131–139]. Here, ultrastable laser oscillators are used to generate equally stable microwaves by optical frequency division [139], or the frequency stability of a microwave signal from an atomic clock can be transferred to a laser for precise spectroscopy [131]. Femtosecond mode-locked lasers can easily bridge the large frequency gap between the RF/microwave domain (MHz to GHz range) and the optical domain (100 THz range): Their optical spectrum is a frequency comb, containing a large number of equidistant optical modes which are spaced by multiples of the repetition rate, while beating between the optical modes, e.g. at a photodetector, produces the fundamental repetition rate and its harmonics in the RF range. Thus, optical and radiofrequencies are linked in a fundamental way, constituting an accurate and broadband rule in the frequency domain. Synchronization techniques allow locking femtosecond lasers to ultrastable continuous-wave lasers or atomic clocks and, at the same time, extraction of microwaves at harmonics of the repetition rate, thus providing precise timing distribution, e.g. for large-scale FEL facilities, which require long-term timing stability between synchronized laser and microwave sources over kilometers of distance [133–135].

In almost all approaches for laser-microwave synchronization, with the notable exception of the balanced optical mixer [136, 137], a photodetector is used at some point to convert the optical pulse train from a mode-locked laser into an electric signal [138–142]. A fast photodiode generates pulses of photocurrent upon illumination by a laser pulse train, which are composed of mode-locked harmonics of the laser's repetition rate up to the photodiode's cutoff frequency, extending in the GHz range for photodiodes with the largest bandwidths [143, 144]. Subsequent narrow-band filtering of the pulsed signal then yields a single harmonic signal at a desired frequency, e.g. in the microwave range, the phase of which is locked to the laser's repetition rate [81]. In general, this process of photoelectric conversion ensures an intrinsic synchronism between the optical and electric pulse trains, similar to the photoemission process of electron pulses from a photocathode (cf. section 2.1). However, nonlinearities and saturation effects of the conversion process can introduce systematic delays between the optical and current pulses [145, 146], while electronic thermal noise [141, 142] and optical shot noise [147] give rise to statistical phase noise and hence timing jitter.

The inherent phase noise of the photocurrent with respect to the timing of the impinging laser pulses poses a lower limit for the achievable timing jitter between the laser's repetition rate and the phase of the extracted microwave signal. It is therefore crucial for all applications employing laser-synchronized microwaves to minimize this initial phase noise upon photodetection of the laser pulse train by all means. In this chapter, an optical enhancement technique is presented, which substantially reduces the thermal noise floor of a laser-synchronized microwave signal extracted from a low-repetition-rate (∼5 MHz) femtosecond laser oscillator via photodetection [142]. Furthermore, the phase noise and phase drift of such a microwave signal are evaluated, as well as the limits they impose on the achievable duration of compressed electron pulses and hence the temporal resolution of UED experiments (cf. section 3.3).

4.1 The thermal noise limit

Thermal agitation of charge carriers in a material of a resistance R at a temperature T gives rise to purely random potential fluctuations across the resistance. The associated standard deviation (rms) of the thermal noise voltage, U_{th}, consists of nearly identical components at all frequencies within the range of practical radiofrequencies. For a finite bandwidth, Δf, it is given by [148, 149]:

$$U_{\mathrm{th}} = \sqrt{4 k_B T R \Delta f}, \tag{4.1}$$

k_B being the Boltzmann constant. If the impedance of the source (e.g. a photodiode) is matched to the load (i.e. the remaining electric circuit), only half of this voltage contributes to the dissipated power, P_{th}, inside the load, and therefore:

$$P_{\mathrm{th}} = \frac{U_{\mathrm{th}}^2}{4R} = k_B T \Delta f \tag{4.2}$$

At room temperature ($T = 300\,\mathrm{K}$), the power spectral density (PSD) of the thermal noise, $P_{\mathrm{th}}/\Delta f = k_B T$, is hence about $-174\,\mathrm{dBm/Hz}$ ($4.14 \cdot 10^{-21}\,\mathrm{W/Hz}$). According to the Fourier theorem, noise can be described in the time domain as a superposition of harmonic signals of different frequencies, amplitudes, and phases. Therefore, each harmonic component of the noise spectrum modulates the desired ideal RF signal which oscillates at its carrier frequency, producing usually symmetric sidebands in the frequency domain at sum and difference frequencies. These modulations constitute amplitude modulations if both sidebands have the same phase, or phase modulations if they have opposite phase. The overall effect of noise is a smeared-out PSD around the carrier. Note that the thermal noise PSD is independent of the resistance and its nearly "white"[1] (i.e. frequency-independent) nature gives rise to a fundamental lower limit of the phase and amplitude noise of an electric signal.

A phase shift of a harmonic signal, $\Delta\phi$, is directly related to a timing delay, Δt, via the signal's carrier frequency, f_0: $\Delta\phi = 2\pi f_0 \Delta t$. Therefore, the rms timing jitter of a signal, J, with respect to a clock, e.g. the repetition rate of a laser pulse train, can be expressed in terms of its phase fluctuations [150]:

$$J = \frac{1}{2\pi f_0} \sqrt{\int_{\Delta f} S_\phi(f)\ \mathrm{d}f} \tag{4.3}$$

Here, $S_\phi(f)$ denotes the double-sideband[2] spectral density of the signal's phase variations and is integrated over the bandwidth of interest, Δf, while f refers to the offset frequency with respect to the carrier. Since the phase noise is usually symmetric around the carrier, it is more common to refer to the single-sideband phase noise spectral density, $\mathcal{L}_\phi(f) = S_\phi(f)/2$ [151], describing the contribution of phase noise sidebands at positive offset frequencies only. If the phase fluctuations (in rad) at an offset frequency f are small, this quantity is directly accessible by measuring the signal's PSD in the phase noise sidebands, $\mathcal{P}_\phi(f)$, in relation to the carrier's

[1] In contrast, technical noise sources, such as electronic $1/f$-noise, are frequency-dependent: They are more pronounced around the carrier frequency and vanish at high offset frequencies with respect to the carrier.

[2] The term "double-sideband" indicates the contribution of both the positive and negative sideband at a particular offset frequency around the carrier to the spectral density of a particular quantity, although $S_\phi(f)$ is a one-sided function of a positive argument f.

total power, P_c, as a function of the offset frequency: $\mathcal{L}_\phi(f) = \mathcal{P}_\phi(f)/P_c$, usually expressed in relative units of decibel below the carrier's power per unit of bandwidth, dBc/Hz. For practical reasons, any RF power measurement always applies to a finite resolution bandwidth, i.e. it is integrated over this bandwidth around a particular frequency. Hence, offset frequencies around the carrier below the resolution bandwidth of the measurement instrument (representing slow drift) are attributed to the carrier's power. Likewise, the PSD is simply the power measured at an offset frequency, divided by the used resolution bandwidth. Note that the total PSD of a signal at a certain offset frequency contains both amplitude and phase noise; however, only phase noise contributes to timing jitter and therefore amplitude noise needs to be suppressed for an accurate measurement if the total power is measured [152].

The rms timing jitter due to the thermal noise floor, J_{th}, follows from eqn 4.3, expressed in terms of $\mathcal{L}_\phi(f)$, using the thermal noise PSD from eqn 4.2, $P_{\mathrm{th}}/\Delta f$:

$$J_{\mathrm{th}} = \frac{1}{2\pi f_0}\sqrt{2\int_{\Delta f}\mathcal{L}_{\phi,\mathrm{th}}(f)\ \mathrm{d}f} = \frac{1}{2\pi f_0}\sqrt{\frac{k_B T \Delta f}{P_c}} \tag{4.4}$$

Here, $\mathcal{L}_{\phi,\mathrm{th}}(f) = P_{\mathrm{th}}/\left(2P_c\Delta f\right) = k_B T/\left(2P_c\right)$ represents the phase noise floor due to thermal noise, which contributes equally to amplitude and phase noise [141, 153], hence P_{th} is divided by 2. It is evident from eqn 4.4 that the timing jitter due to thermal noise depends on the signal-to-noise ratio (SNR), i.e. the power in the carrier over the power in the thermal noise background within the bandwidth of interest. Thus, minimizing the timing jitter of a microwave signal extracted from a photodiode with respect to the laser's repetition rate requires the highest possible RF power from the photodiode (P_c) at the highest possible microwave frequency (f_0) and a minimized bandwidth of the application (Δf). The carrier frequency and noise bandwidth are given by the design of the microwave cavity (cf. section 3.2), which is based on a reasonable resonance frequency for linear and efficient electron compression and a minimum bandwidth to accommodate for the frequency fluctuations of the laser's repetition rate (see section 4.3). Therefore, in order to reduce the contribution of the thermal noise floor to the total timing jitter below 1 fs rms at a carrier frequency of 6.2 GHz and a bandwidth of 1 MHz, the microwave power in the carrier, P_c, must exceed −26 dBm (2.5 µW) at room temperature. Reducing the temperature can also improve the timing jitter, since it reduces the thermal noise floor. However, the technical effort for this is substantial, while the benefit is rather small. Cooling down from room temperature to liquid nitrogen temperature (77 K) reduces the timing jitter only by a factor of 2, and reducing the temperature by orders of magnitude is impossible due to the heat deposition from the laser, besides the obvious technical challenges. Hence, we choose to enhance the power of the ex-

tracted microwave signal in order to increase the SNR and consequently to reduce the jitter related to the thermal noise floor into the attosecond range.

4.2 Optical mode filtering

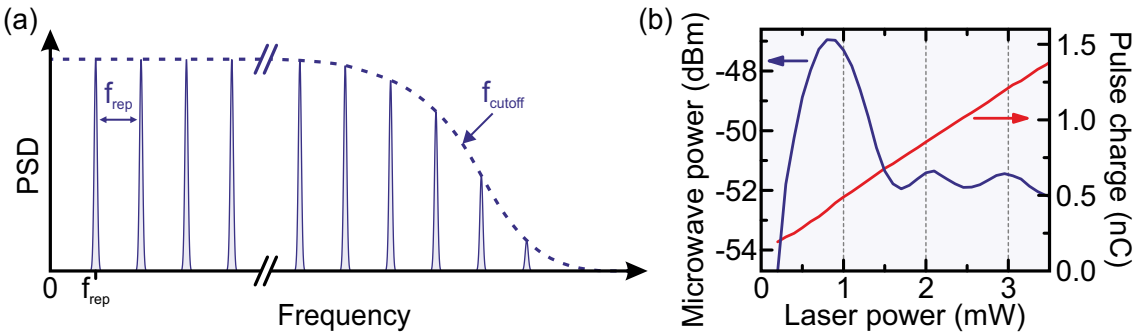

Figure 4.1: Frequency response and saturation effects of a fast photodiode. (a) Schematic power spectral density of the photocurrent response of a photodiode illuminated by a femtosecond laser pulse train of a repetition rate f_{rep}. The laser's frequency comb is transferred to the photocurrent, which is composed of harmonics of the repetition rate until the photodiode's cutoff frequency, f_{cutoff}. The entire photocurrent spectrum can comprise thousands of modes for a high-bandwidth photodiode (f_{cutoff} in the GHz range) and a laser of low repetition rate (few MHz or less). The width of the modes is exaggerated. (b) Measurement of the microwave power (single harmonic at 6.2 GHz, blue) and pulse charge (integrated photocurrent over one pulse, red) of a fast photodiode, illuminated by 800 nm laser pulses at ∼5 MHz repetition rate, as a function of the average laser power. Saturation effects manifest as a decrease of microwave response at high laser intensities, while the pulse charge (i.e. photocurrent) is still linear.

The microwave power which can be extracted from a photodiode is limited, since the extractable photocurrent density saturates at a certain optical intensity (i.e. power per area). The total saturation current depends on the photodiode's design, as does the cutoff frequency: While a large active area facilitates a high photocurrent at a given optical intensity, it also increases the photodiode's capacitance and hence reduces its cutoff frequency. There is an optimum choice of the active area to extract the highest possible microwave power, when the frequency of the desired microwave signal is near to the photodiode's cutoff frequency.

When illuminated by femtosecond laser pulses, the electric power generated in the photodiode is distributed over all modes constituting the photocurrent pulses. This is illustrated in fig. 4.1 (a). However, only one mode of the frequency comb at the desired microwave frequency, optimally near to the photodiode's cutoff frequency, is needed for the application (e.g. electron pulse compression), while all other modes are suppressed or disregarded. This single mode contains only a fraction of the total

electric power, roughly $f_{\mathrm{rep}}/f_{\mathrm{cutoff}}$, f_{rep} being the laser's repetition rate and f_{cutoff} the photodiode's cutoff frequency. Therefore, the effective loss of microwave power due to this power distribution into many modes becomes more severe for lasers of low repetition rate (few MHz or less), for which $f_{\mathrm{rep}}/f_{\mathrm{cutoff}}$ is on the order of 10^{-3} or less if a fast photodiode with a cutoff frequency in the GHz range is used.

Recently developed high-power photodiodes promise watts of average microwave power if a suitable light source is used [144, 154]. However, the high peak power of femtosecond laser pulses, rather than the average power, is the dominating cause for saturation in this regime due to the generation of high space charge densities inside the p-n junction of a photodiode, leading to a significantly reduced high-frequency response [140, 155]. Fig. 4.1 (b) demonstrates the effect of saturation on the extractable microwave power from a fast GaAs photodiode used in this work (ET4000, EOT, Inc. with a cutoff frequency of $\gtrsim$10 GHz), illuminated by femtosecond laser pulses from a Ti:sapphire oscillator (see section 4.3) at 800 nm wavelength and a repetition rate of 5.128 MHz. The microwave power of a single mode (blue) at the $\sim 1200^{\mathrm{th}}$ harmonic of the repetition rate at about 6.2 GHz is measured with a spectrum analyzer (PSA E4447A, Agilent Technologies, Inc.) as a function of the average laser power on the photodiode. At the same time, the photocurrent is integrated over a single pulse with an oscilloscope, yielding the generated pulse charge (red). Saturation due to the peak power is evident above 0.85 mW of laser power, corresponding to 0.17 nJ of optical pulse energy, since the microwave yield decreases with increasing optical power, while the pulse charge, i.e. the integrated photocurrent, is still linear. The peak photocurrent (not shown) starts to saturate at about the same laser power, thus broadening the photocurrent pulse in time.

Our approach is to redistribute the PSD in the photocurrent response of a photodiode into (ideally) a single harmonic at the desired microwave frequency, while still allowing a laser of low repetition rate to be used. This is achieved by an optical mode filter for the laser pulses: a small optical cavity which converts each laser pulse into a rapid pulse train before impinging on the photodiode [142]. Fig. 4.2 (a) illustrates this approach. Two curved mirrors of a reflectivity R, separated by a distance L, form a cavity with an oscillation frequency of $f_{\mathrm{microwave}} = c/(2L)$ for a laser pulse that is coupled into the cavity through one of the mirrors. If the laser's repetition rate, f_{rep}, is much smaller than $f_{\mathrm{microwave}}$, only a single pulse oscillates inside the cavity, generating a decaying pulse train at the output with a temporal spacing of $1/f_{\mathrm{microwave}}$. In the frequency domain, this constitutes a band-pass filter with a central passband frequency of $f_{\mathrm{microwave}}$; thus, only laser modes at multiples of $f_{\mathrm{microwave}}$ are transmitted, while all others are reflected – hence the term "mode filter". If the cavity length, L, is chosen such that $f_{\mathrm{microwave}}$ is the desired microwave frequency, the power extracted from the photodiode at this frequency is enhanced

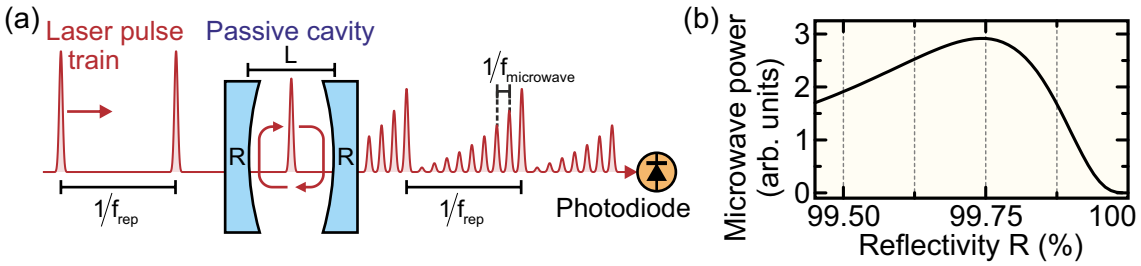

Figure 4.2: Concept of microwave enhancement by mode filtering. (a) Mode filter in the time domain. A passive optical cavity (reflectivity R, mirror separation L) converts incoming laser pulses with a repetition rate f_{rep} into trains of decaying pulses, separated in time by $1/f_{microwave}$. (b) Simulation of the power at $f_{microwave} = 6.2\,GHz$ extracted from a photodiode after mode filtering as a function of the mirror reflectivity with input laser pulses of constant intensity and at $f_{rep} = 5.1\,MHz$. The optimum is at $R = 99.75\,\%$.

because all other modes are suppressed, provided that the optical power after mode filtering is sufficient to saturate the photodiode.

The enhancement of the microwave power by optical mode filtering depends on the reflectivity R of the cavity mirrors. A too high reflectivity might require more laser power than available at the input in order to couple in enough optical power to extract the maximum microwave power from the photodiode (just below saturation). Also, the cavity needs to be optically depleted before the next laser pulse; otherwise it would interfere with the residual previous pulse oscillating inside the cavity and thus distort the output pulse train or require an interferometric stabilization of the cavity's length. A low reflectivity, on the other hand, leads to a rapid decay of the output pulse train, resulting in a reduced enhancement. The optimum reflectivity can be found by considering the decaying mode-filtered pulse train. The intensity of the N^{th} pulse within the pulse train (starting at $N = 1$) is given by:

$$I_N \propto (1 - R)^2 R^{2(N-1)} \tag{4.5}$$

The frequency response of the mode-filtered laser pulses on a photodiode is numerically simulated in the time domain with a laser repetition rate of $f_{rep} = 5.128\,MHz$, a response time of the photodiode of 60 ps FWHM, a repetition rate of the pulses within the decaying pulse train of $f_{microwave} = 6.237\,GHz$ (i.e. a mirror separation of $L = 24\,mm$), and an envelope given by eqn 4.5. The input laser intensity is kept constant and the reflectivity, R, is varied. Fig. 4.2 (b) shows the amplitude of the PSD of this simulated time-domain signal at $f_{microwave}$ as a function of the reflectivity. An optimum is found at $R = 99.75\,\%$, corresponding to a finesse[3] of the cavity of

[3]The finesse of the optical mode filter described here, which is by definition a Fabry-Pérot interferometer or etalon, is given by $\mathcal{F} = \frac{\pi\sqrt{R}}{1-R}$.

1255, which is the best trade-off between optical throughput (low reflectivity) and low decay rate (high reflectivity). Note that the power ratio transmitted through the mode filter is $(1 - R)/2$ (the factor 1/2 accounts for the fact that a decaying pulse train is produced at both cavity mirrors), leaving only a small fraction of the input laser power to be used for microwave generation at the photodiode. In the experiment, all available laser power from the oscillator (see section 4.3) needs to be directed onto the mode filter in order to maximize the microwave output from the photodiode (near saturation). Nearly the total power is reflected from the first mirror ($\sim R$) and separated from the incoming beam via a Faraday rotator. This power, less the losses from the Faraday rotator, is available for UED experiments.

Fabry-Pérot cavities similar to the one reported here are sometimes used as repetition rate multipliers [140, 141, 156–158] for the generation of femtosecond laser pulse trains at very high repetition rates (in the GHz range), which are difficult to obtain directly from laser oscillators. However, these cavities are operated at comparably small multiplication factors (up to 20) and at already high repetition rates of the input laser pulses (hundreds of MHz to 1 GHz) [141, 159]. At these repetition rates, the incoming pulses interfere with the pulse oscillating inside the cavity, thus precise active stabilization of the cavity's length and the corresponding $f_{\mathrm{microwave}}$ to a harmonic of the laser's repetition rate is required. In contrast, our cavity is operated at a very high multiplication factor ($\sim$1200) and is optically depleted before the next pulse arrives, thus avoiding interference and the need for an active stabilization (i.e. feedback or lock).

4.3 The laser system

As pointed out earlier (cf. section 1.3), the ideal laser system for single-electron UED experiments operates at intermediate repetition rates between typical ultrafast laser oscillators (tens to hundreds of MHz) and regenerative amplifier systems (few kHz). For many UED samples with interesting structural dynamics upon photoexcitation, a repetition rate in the 100 kHz to few MHz range leaves enough time for relaxation between two consecutive shots, while allowing acquisition of a diffraction image with single-electron pulses in a reasonable time [85]. The required optical pulse energy is essentially determined by the pump volume and absorption cross-section of the sample, since the generation of single-electron pulses from a photocathode only requires some pJ of pulse energy in the UV and the photodiode for microwave extraction saturates already at well below 1 nJ (cf. section4.2). Higher pulse energy is required if parametric conversion of the fundamental wavelength is employed.

The laser system used in this work is a long-cavity Ti:sapphire oscillator (Femtosource XL, Femtolasers Produktions GmbH), providing a high pulse energy of

about 500 nJ directly from the oscillator and a repetition rate of 5.128 MHz (about 2.6 W of average power) at a central wavelength of about 800 nm [87]. The oscillator operates in the positive dispersion regime, i.e. the pulses inside the cavity are chirped and therefore temporally broadened in order to achieve high pulse energies at peak intensities below the damage threshold of the laser crystal. The pulses are compressed by a prism compressor outside the cavity, allowing pre-compensation of dispersion in the experiment. Mode-locking is achieved by a combination of Kerr-lens mode-locking and a saturable semiconductor Bragg reflector [160]. Fig. 4.3 shows a typical spectrum and intensity autocorrelation of the laser, yielding a duration of the compressed optical pulses of about 50 fs FWHM (Gaussian intensity envelope). The non-Gaussian spectrum with the steep edges produces a temporal pedestal of the pulse over several 100 fs, >90 % of the total power being confined within ±100 fs.

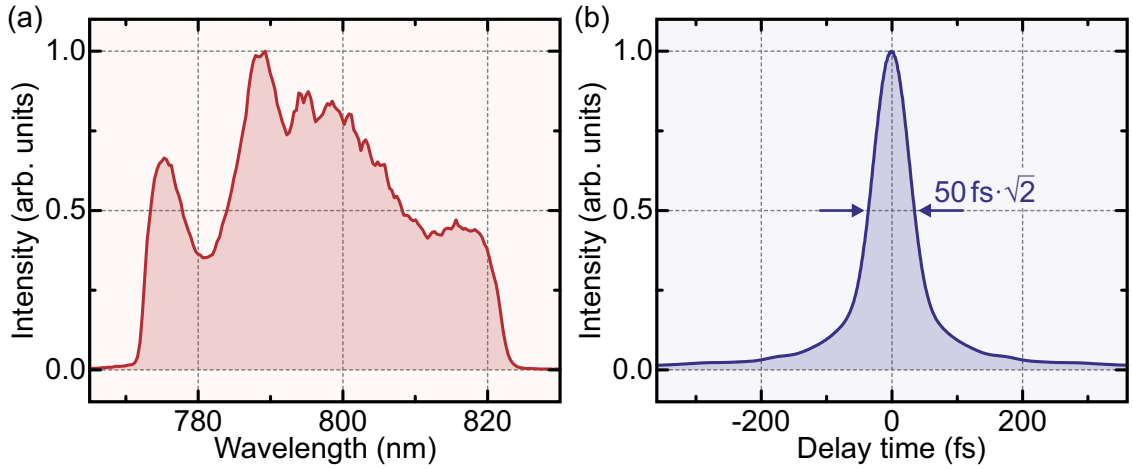

Figure 4.3: (a) Typical spectrum of the long-cavity Ti:sapphire oscillator, spanning from 770 nm to 825 nm. (b) Corresponding intensity autocorrelation, yielding a pulse duration of 50 fs FWHM. Note that the temporal width of the intensity autocorrelation is larger than the actual pulse duration by a factor of $\sqrt{2}$.

The quality of laser-microwave synchronization via a fast photodiode depends, apart from the thermal noise limit (cf. section 4.1), also on the amplitude and frequency fluctuations of the laser pulses. While the absolute timing of the laser pulses directly transfers to the photocurrent pulses extracted from the photodiode, any filter components with a frequency-dependent phase, e.g. the optical mode filter cavity or subsequent microwave electronics, convert frequency fluctuations into phase and therefore timing fluctuations. Likewise, amplitude noise can induce timing jitter via amplitude-to-phase coupling in photodiodes [145, 146]. Measurements of the laser's phase noise and slow drift of the repetition rate are shown in fig. 4.4, acquired with the same photodiode and spectrum analyzer as in fig. 4.1 (b). The phase noise in fig. 4.4 (a) is measured at the fundamental repetition rate of 5.128 MHz for off-

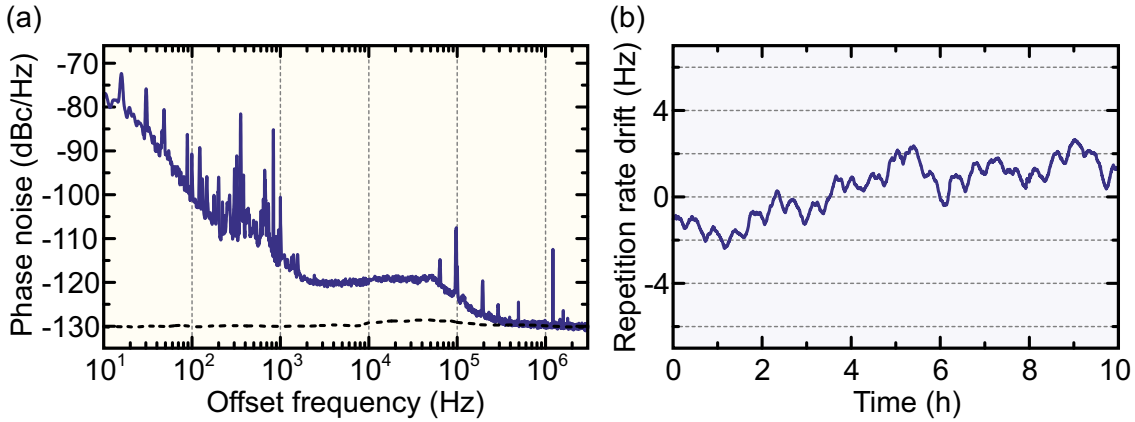

Figure 4.4: Phase noise and drift of the repetition rate of the laser system. (a) Phase noise measured relative to the internal clock of a spectrum analyzer at the fundamental repetition rate of 5.128 MHz. Significant phase noise contributions from the laser are visible at acoustic frequencies (<2 kHz) due to mechanical vibrations, while the plateau (>2 kHz) is dominated by the phase noise of the analyzer's clock. The dashed line denotes the analyzer's noise floor due to its dynamic range. (b) Repetition rate drift showing deviations from the central repetition rate at 5.128 MHz. The characteristic oscillations reflect fluctuations of the ambient temperature.

set frequencies from 10 Hz to the Nyquist frequency (2.56 MHz). The measurement reproduces the relative phase noise between the laser's repetition rate and the analyzer's internal clock (frequency stability of $5 \cdot 10^{-7}$). Hence, the general $1/f$-behavior at low offset frequencies and the characteristic plateau (>2 kHz) are dominated by the phase noise of the analyzer's clock, while its dynamic range limits the measurement floor (dashed line) above 500 kHz. The spikes at acoustic frequencies denote mechanical vibrations of the laser cavity's mirrors, which can cause substantial timing jitter of a long-cavity oscillator, contributing about 10 ps rms at the fundamental repetition rate. This value is scaled down by the harmonic number when considering harmonics of the repetition rate, e.g. at microwave frequencies (cf. eqn 4.3). The drift of the central repetition rate, shown in fig. 4.4 (b), is mainly limited by temperature stabilization, since it follows the temperature oscillations in the laboratory (about 0.1 °C with a half an hour period). Nevertheless, the frequency stability is better than 1 Hz (or $2 \cdot 10^{-7}$) over one hour and substantially better on a minute time scale. Amplitude fluctuations are ∼0.5 % rms under good conditions [142].

Consequentially, the bandwidth of the microwave cavity for electron pulse compression used in this work (about 2 MHz, cf. section 3.2) has been chosen to accommodate for the phase noise and drift of the laser's repetition rate, which are transferred to the extracted microwave signal. The drift is on the order of 1 kHz over one hour at the ∼1200$^{\text{th}}$ harmonic of the repetition rate, and also nearly the entire noise power is contained within this narrow bandwidth, according to fig. 4.4 (a). However,

the bandwidth of the microwave cavity has been chosen to be substantially larger in order to reduce the effect of its frequency-dependent phase. According to eqn 3.21 in section 3.2, such a drift of the repetition rate corresponds to a timing drift of about 30 fs for the microwave cavity used in this work. This drift is expected to be much smaller over shorter time scales.

Ultrafast laser oscillators at high repetition rates, especially monolithic Erbium-doped fiber lasers, offer a superior stability of the repetition rate, since mechanical vibrations are substantially reduced and less severe in terms of timing jitter compared to the long-cavity laser system used in this work. Microwave extraction with sub-femtosecond timing jitter has been demonstrated with such types of oscillators at repetition rates of 75 MHz and above [134, 136–139]. However, despite their tremendous value for precise timing distribution and metrology, these laser sources provide too little pulse energy for studying ultrafast dynamics in condensed matter. Amplifying the pulses from such oscillators at strongly reduced repetition rates, in order to provide sufficient energy of the pump pulses, can introduce additional femtosecond timing jitter at the sample. Since the microwave is extracted from the oscillator, the temporal resolution is limited by the relative timing jitter between the amplified pulses and the pulses directly from the oscillator. Another intricate approach involves locking a laser of low repetition rate, capable of providing sufficient pulse energy, to a highly stable oscillator for microwave extraction [133, 134].

Deriving the microwave signal directly from the pump pulses promises the lowest pump-probe jitter for UED applications and minimal technical effort. The long-cavity laser system used in this work provides pulse energies suitable for UED directly from the oscillator and a reasonable frequency stability without the need for amplification or active control of the repetition rate. Here, mode filtering (cf. section 4.2) enables microwave extraction from laser pulses of low repetition rate at power levels sufficiently above the thermal noise floor for a timing jitter in the few-femtosecond range or below.

4.4 Experimental performance

As a first experiment, the optical enhancement of microwave yield at the 1216^{th} harmonic of the laser's repetition rate is determined. The optical mode filter cavity in the experiment consists of curved mirrors with a reflectivity of $R = (99.75 \pm 0.05)\,\%$ over the entire spectrum of the laser, a radius of curvature of 200 mm, and a separation between the mirrors of $L = 24\,\text{mm}$. Transverse mode size matching with the incoming beam is approximately achieved via a 200 mm focusing lens outside the mode filter. The total available laser power is impinging at the end mirror of the mode filter and the reflected beam is separated from the incoming beam via a Faraday rotator.

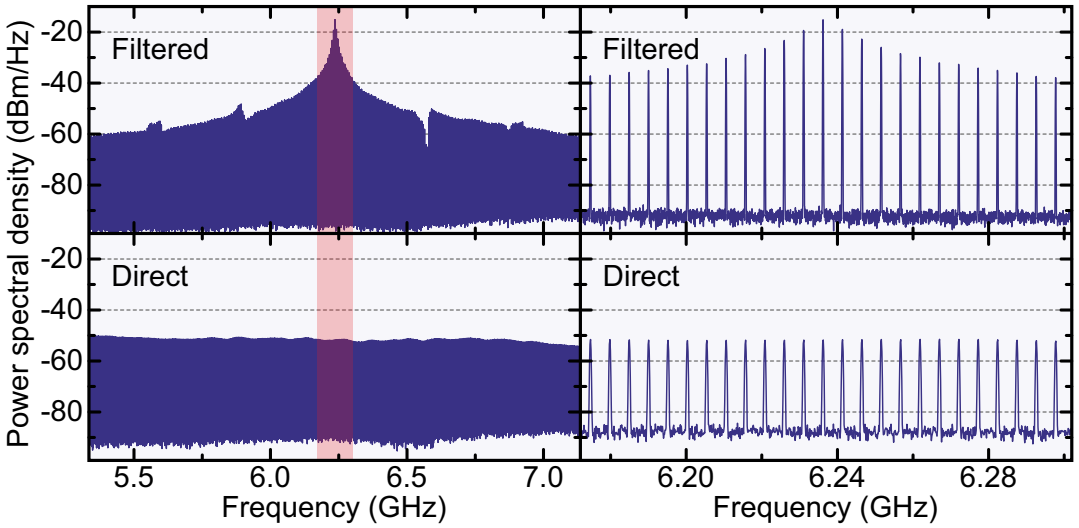

Figure 4.5: Microwave power enhancement by mode filtering. The PSD of the photocurrent signal from a fast photodiode after mode filtering (upper panels) shows an enhancement at the 1216$^{\text{th}}$ harmonic of the laser's repetition rate at 6.237 GHz by 36 dB (a factor of ∼4000), compared to photodetection at the same optical power but without mode filtering (lower panels). Note that the individual modes are indistinguishable at the zoom level in the left panels. The right panels show a zoom of the red shaded region and the mode spacing by the laser's repetition rate (5.128 MHz) is visible.

After mode filtering, about 2.5 mW of power is available for microwave extraction, which is focused via a 20 mm focusing lens onto a fast photodiode (ET4000, EOT, Inc.) with a diameter of the active area of 40 µm. The photocurrent signal from the photodiode is monitored with a spectrum analyzer around the desired microwave frequency at 6.237 GHz for optimization of all alignment parameters of the mode filter (especially the mirror separation) and the photodiode. Fig. 4.5 shows the microwave PSD extracted from the photodiode after mode filtering in comparison to unfiltered photodetection at the same average optical power at the photodiode. The microwave power is clearly redistributed from an initially almost flat PSD (lower panels) into modes around the desired microwave harmonic (upper panels), defined by the mirror separation of the mode filter cavity. If no mode filtering is applied, the microwave power in the 1216$^{\text{th}}$ harmonic of the laser's repetition rate at 6.237 GHz is −51 dBm. According to eqn 4.4, this power level above thermal noise amounts to 18 fs rms of timing jitter per 1 MHz of bandwidth, setting a fundamental limit for the quality of synchronization. With the mode filter, the microwave power in this harmonic is enhanced to −15 dBm and the timing jitter related to thermal noise is accordingly reduced to 0.3 fs rms per 1 MHz of bandwidth, paving the way for laser-microwave synchronization with attosecond precision at low repetition rates. This power enhancement by 36 dB corresponds to a factor of almost 4000.

The optical cavity acts as a passive band-pass filter for laser modes around multiples of its passband frequency (cf. section 4.2). This filter can be characterized by its finesse, $\mathcal{F}$, in analogy to the Q-factor used for oscillating electric circuits or RF cavities (cf. section 3.2). The finesse is defined as the ratio between the free spectral range, i.e. the fundamental passband frequency, $f_{\text{microwave}}$, given by the separation between the mirrors, and the FWHM bandwidth of each transmitted band. An optical mode filter has identical transmission characteristics at all multiples of $f_{\text{microwave}}$ (within the wavelength range of the reflective coating), which is generally not the case for electric circuits. The Q-factor is thus identical to the finesse for the fundamental passband at $f_{\text{microwave}}$ (cf. eqn 3.20). According to eqn 3.21, a phase flip of $\pm 90°$ is expected over the passband, or $\pm 45°$ within the FWHM bandwidth.

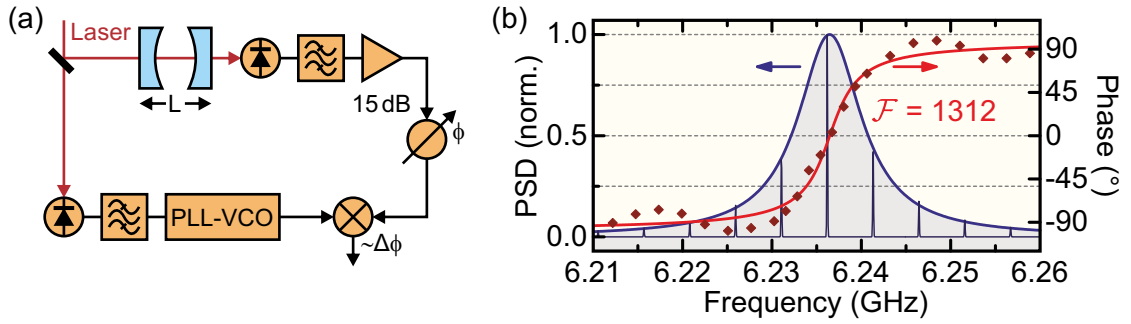

Figure 4.6: Phase measurement of the optical mode filter. (a) Setup for the phase measurement. The laser is split into a mode-filtered and an unfiltered part, each detected via a fast photodiode. Each photocurrent signal passes through a band-pass filter in order to isolate a mode at 6.237 GHz. The signal without the mode filter is used to lock a PLL-VCO to the laser's repetition rate. The mode-filtered signal is amplified and combined with the signal from the PLL-VCO at a double-balanced mixer. The mode filter's phase is measured by varying the separation between the mirrors, L, while the output of the mixer, which is a periodic function of the phase difference at its inputs, is controlled to zero by a calibrated phase shifter in the mode-filtered signal's path. (b) The enhanced PSD at the photodiode is shown as dark blue spikes (data identical to fig. 4.5, upper panels) and the envelope is fitted with a Lorentzian (blue line) according to eqn 3.19. The measured phase (dark red diamonds) is fitted according to eqn 3.21 (red line), yielding a finesse of 1312. Note that the phase shows ripples around the passband frequency and the frequency range between $\pm 45°$ implies a smaller FWHM bandwidth and thus a higher finesse than what is measured for the transmission (blue line).

A measurement of the mode filter's phase is shown in fig. 4.6. The technique is similar to the phase measurement of the microwave cavity (cf. section 3.2); however, sweeping the input frequency (i.e. the laser's repetition rate) is not possible here. Instead, the passband frequency of the mode filter is varied over a short range by changing the distance of the mirror separation, L, as shown in fig. 4.6 (a). The laser is split into a mode-filtered and an unfiltered part, each detected via a fast photodiode. The corresponding signals are shown in the upper and lower panels of fig. 4.5,

respectively. A single mode is isolated from both photocurrent signals via narrow band-pass filters at 6.237 GHz (FWHM bandwidth of 5 MHz). For measuring the phase between two signals of identical frequencies, a double-balanced mixer is used, the output of which is a periodic function of the phase difference between the two input signals. The mixer requires similar amplitudes of the input signals at a power level on the order of 0 dBm to 10 dBm to properly work as a linear phase detector. Therefore, the mode-filtered signal is amplified by ∼15 dB via a low-noise amplifier (HD26945, HD Communications Corp.) to approximately 0 dBm. The initial power level of the unfiltered signal is much lower and even after the band-pass filter it contains pronounced sidebands at multiples of the laser's repetition rate (5.128 MHz), which would compromise the phase measurement at the mixer. The unfiltered signal is therefore used to lock an external microwave synthesizer (SMF100A, Rohde & Schwarz GmbH) to the laser's repetition rate by means of a proportional-integrating loop filter (D2-125 Laser Servo, Vescent Photonics, Inc.) controlling the synthesizer's frequency modulation. The loop filter detects a phase mismatch between the synthesizer's signal and the 6.237 GHz signal from the photodiode via another double-balanced mixer and permanently adjusts the synthesizer's frequency via a control voltage output in order to keep the phase mismatch at zero. This system constitutes a phase-locked loop voltage-controlled oscillator (PLL-VCO), which is widely used in RF electronics to lock the frequency and phase of a signal generator to an arbitrary reference signal. The power of the microwave synthesizer is adjusted to match the power of the amplified mode-filtered signal at the mixer. In order to measure the phase difference between the mode-filtered and unfiltered signal, a calibrated manual phase shifter is introduced into the mode-filtered signal path and the direct current (DC) part of the mixer's output signal is controlled to zero for each value L of the separation between the mode filter's mirrors.

The resulting phase measurement is shown in fig. 4.6 (b) as dark red diamonds, fitted according to eqn 3.21 (red line). A Q-factor or finesse of 1312 (FWHM bandwidth of 4.8 MHz) is extracted from the fit, matching well to the designed finesse of 1255. A deviation from the ideal damped cavity (cf. section 3.2) manifests as ripples of the phase around the passband frequency and can also be observed as modulations of the transmission curve in the upper left panel of fig. 4.5. For comparison, the transmitted modes are shown in dark blue (cf. the upper panels in fig. 4.5; here on a linear scale). The envelope is fitted with a Lorentzian (blue line) according to eqn 3.19, yielding a finesse of only 723 (FWHM bandwidth of 8.6 MHz). The inconsistency with the finesse extracted from the phase measurement can be attributed to nonlinearities of the photodetection process (e.g. saturation), non-ideal transverse mode matching between the incoming laser beam and the mode filter, and imperfect focusing on the photodiode. The phase measurement reveals the mode filter's finesse

more accurately, since it does not depend on the efficiency of photodetection. This also implies that the microwave enhancement by mode filtering the laser pulses can be about a factor of 2 higher than reported here (approaching 10^4) with optimized photodetection. The phase slope at the central passband frequency, extracted from the fit, is 24.1 °/MHz, corresponding to a timing deviation of 10.7 fs/kHz or 2.8 fs/nm in terms of the drift of the separation, L, between the mode filter's mirrors at the chosen microwave frequency.

As pointed out before, sources for systematic phase drift of the mode-filtered signal, such as mechanical vibrations of the mode filter's mirrors, drift of the laser's repetition rate, and amplitude-to-phase coupling in the photodiode, contribute together with purely statistical noise (thermal noise and shot noise) to the total phase noise and drift of the microwave signal. Here, we demonstrate the improvement of the statistical noise floor, governed by thermal noise, by mode filtering. Fig. 4.7 shows a measurement of the statistical phase noise and the according timing jitter of the enhanced microwave signal at 6.237 GHz. To this end, the mode-filtered laser beam is split in two parts, impinging on two identical photodiodes (see fig. 4.7 (a)). Systematic fluctuations of the mode filter cavity, the laser's repetition rate, or the amplitude are correlated and thus cause identical phase fluctuations of the signals from both photodiodes. In contrast, thermal noise, being purely statistical, causes uncorrelated phase fluctuations at the photodiodes. As before, harmonics at 6.237 GHz are isolated via narrow band-pass filters; then both signals are amplified by ∼15 dB and combined at a double-balanced mixer. The mixer's output is low-pass filtered below 2.5 MHz and amplified via a low-noise voltage amplifier (HVA-10M-60B, Femto Messtechnik GmbH) by 60 dB, corresponding to a power amplification of 30 dB. Since only small phase fluctuations are measured, the mixer's output voltage is proportional to the phase difference. The slope of the mixer's voltage is thus calibrated by a manual phase shifter within a short range around zero phase difference and used to convert the measured fluctuations of the voltage amplitude into phase noise. A spectrum analyzer records the PSD of the mixer's amplified output signal within the range of 1 Hz to 1 MHz, while an analog-to-digital converter (ADC) samples the signal in real-time with a sampling rate of 5 kHz.

Fig. 4.7 (b) shows the single-sideband phase noise PSD measured with the spectrum analyzer (light blue line) and the phase noise PSD calculated from the sampled ADC signal by Fourier transformation (dark blue line), together covering slow drift as well as high-frequency components within a frequency range of 2 mHz (8.3 min) to 1 MHz (1 µs). The integrated jitter within this frequency range is ∼3.5 fs rms (green line), which is an upper limit, essentially inflicted by the instrument's noise floor, as well as the reduced optical power on the two photodiodes due to the split mode-filtered laser beam. The calculated thermal noise PSD of the unfiltered signal

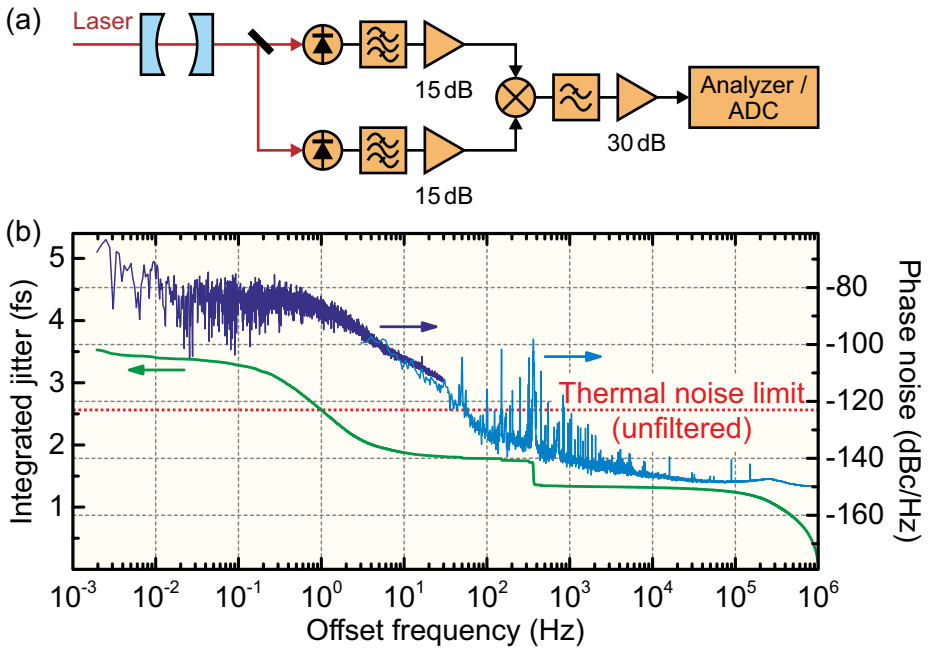

Figure 4.7: Measurement of the statistical (uncorrelated) single-sideband phase noise and timing jitter of the enhanced microwave signal. (a) Two identical photodiodes are illuminated by the same mode-filtered laser beam via a beam splitter. The two signals are band-pass filtered around 6.237 GHz, amplified, and combined at a double-balanced mixer. The mixer's output signal, proportional to the phase difference between the input signals, is low-pass filtered, amplified, and characterized with a spectrum analyzer (high frequencies) and an ADC (low frequencies and drift). (b) Phase noise PSD measured with the spectrum analyzer (light blue line) and calculated from the time-domain signal sampled by the ADC (dark blue line). This measurement is essentially limited by the instrument's noise floor. However, at offset frequencies above ∼50 Hz the measured phase noise PSD of the enhanced signal is already below the theoretical thermal noise limit without mode filtering (red dotted line). The integrated timing jitter (green line) amounts to about 3.5 fs rms from 2 mHz to 1 MHz, while the unfiltered thermal noise floor amounts to 18 fs rms of jitter within this range.

is at −123 dBc/Hz (red dotted line), amounting to 18 fs rms of jitter within this range. This clearly demonstrates the improvement of the statistical noise floor by mode filtering. However, systematic drift and noise sources which are not measured by this approach can deteriorate the synchronization between the laser's repetition rate and the extracted microwave signal.

4.5 Quality of synchronization

The quality of laser-microwave synchronization dictates the achievable temporal resolution in UED experiments employing compression of electron pulses with microwave fields (cf. section 3.3). Enhancement of the microwave power extracted from

a photodiode, as presented in this chapter, substantially increases the microwave's SNR with respect to thermal noise, potentially offering microwave synchronization to laser pulses of low repetition rate with attosecond timing jitter. Other sources for phase noise and drift, and hence timing jitter, are not compensated by this passive synchronization scheme and need to be carefully considered, as they pose a technical limit for the temporal resolution.

The passively enhanced microwave signal suffers mainly from three systematic contributions to timing drift or jitter: First, mechanical vibrations of the mode filter's mirrors cause phase fluctuations (cf. fig. 4.6 (b)). Second, drift of the laser's repetition rate translates into phase drift due to the mode filter's frequency-dependent phase. Third, fluctuations of the laser's power give rise to phase noise due to amplitude-to-phase coupling in the photodiode. As shown in the previous section, the separation between the mode filter's mirrors needs to be stabilized with nanometer precision or better for few-femtosecond timing jitter or below. Long-term thermal drift changes the length of the mode filter by an amount on the order of 20 nm–30 nm, corresponding to a delay drift of 60 fs–90 fs on a time scale of about one hour. The mechanical stability can be improved by a monolithic design. In addition, thermal and mechanical isolation as well as appropriate materials can provide a length stability on the picometer scale [161], which would facilitate sub-femtosecond timing stability. Drift of the laser's repetition rate (cf. section 4.3) is less severe: Harmonics of the repetition rate at microwave frequencies drift about 1 kHz on an hour scale, leading to about 11 fs of timing drift due to the mode filter's frequency-dependent phase. This is less than the timing drift caused by the microwave cavity's phase (cf. section 3.2), since the bandwidth of the microwave cavity is narrower. The frequency-dependent phase of all involved microwave electronics, such as filters, amplifiers, and even cables [162], likewise contributes to timing drift, although to a substantially smaller degree due to their (usually) much higher bandwidth compared to the mode filter and microwave cavity.

Amplitude-to-phase coupling in the photodiode translates fluctuations of the laser's power into phase noise [145]. The amplitude-to-phase coefficient depends mainly on the extracted photocurrent (i.e. optical power) and the type of the photodiode. It has been found to vanish at certain values of the photocurrent, depending on the carrier frequency and the photodiode type [145, 146]. At a carrier frequency of 6.237 GHz and 2 mW of optical power incident on the photodiode, this coefficient is 0.07 rad/$(\Delta P/P_0)$ [142], where $\Delta P/P_0$ denotes the relative change in optical power. For the laser system used in this work, $\Delta P/P_0 \approx 0.5\,\%$ rms under good conditions (cf. section 4.3), yielding about 10 fs rms of timing jitter. This contribution can be significantly reduced by carefully choosing an appropriate photodiode and optical power with a minimized or vanishing amplitude-to-phase coefficient.

Quantum noise of the photon number contained in the laser pulses, also referred to as shot noise, poses another fundamental limit on the quality of laser-microwave synchronization. This noise source inherently smears out the timing of laser pulses with respect to an ideal timing reference because it randomly distorts the pulse's temporal intensity envelope and thus its center of mass. In contrast, thermal noise is imprinted onto the electric signal after photodetection. However, for femtosecond laser pulses and the power levels of the extracted microwave demonstrated in section 4.4, the shot noise PSD lies several orders of magnitude below the thermal noise floor [147]. Shot noise competes with thermal noise only at extreme levels of microwave power extracted from the photodiode, on the order of 1 W [147]. At that power level, the thermal noise floor corresponds to a timing jitter of only 1.6 as rms per 1 MHz of bandwidth at a carrier frequency of 6.237 GHz (cf. eqn 4.4).

For applications that require a high level of microwave power, such as compression of electron pulses with microwave fields [70, 81], further amplification of the signal from the photodiode is required. The SNR of the microwave is reduced after amplification because additional noise from the amplifier, referred to as the noise figure, is added. Typically, the noise figure depends on the gain and therefore a high power level of the signal from the photodiode is beneficial in order to maintain the SNR, since less amplification is required afterwards. For example, a noise figure of 6 dB (typical for a gain between 40 dB and 50 dB at ∼6 GHz) increases the timing jitter related to thermal noise due to the reduced SNR by a factor of 2, according to eqn 4.4.

The passively enhanced microwave extraction from a femtosecond laser pulse train presented here constitutes a simple but effective microwave source for electron pulse compression at low repetition rates suitable for UED. A high-quality synchronization with a timing drift and jitter of some tens of femtoseconds over short times is readily available without any active compensation. The achievable stability of this microwave source is currently limited by thermal drift, mechanical vibrations, and amplitude fluctuations. Advancing the synchronization into the few-femtosecond or attosecond range with the passive approach therefore requires extensive thermal and mechanical stabilization of the environment as well as a specially engineered photodiode, which provides high microwave power and a minimized amplitude-to-phase coefficient.

The improved thermal noise floor of the microwave source presented here paves the way for attosecond synchronization. Active compensation of the remaining drift and jitter via optical interferometric laser-microwave phase detection in combination with a feedback loop promises sub-femtosecond stability with regard to both timing drift and jitter [136, 137].

Chapter 5

Characterization of jitter by microwave streaking

The temporal resolution of UED experiments employing electron pulse compression with microwave fields is limited by the quality of synchronization between the microwave's phase and the timing of the laser pump pulses (cf. sections 3.3 and 4.5). Noise and drift of the microwave signal have been estimated in the previous chapter; however, only a direct characterization of the timing jitter between the microwave's phase and the laser's repetition rate reveals the system's actual performance. Laser-microwave phase detection has been demonstrated before with sub-femtosecond precision [136, 137]. These approaches, however, require a separate feed of the microwave signal and hence fail to measure the microwave's phase inside the cavity for electron pulse compression. Thus, possible cavity-related phase drift, e.g. due to temperature drift or fluctuations of the laser's repetition rate, is not detected. Only recently a laser-microwave phase detection scheme has been demonstrated which directly employs the electric field of the TM_{010} mode inside a microwave cavity suitable for electron pulse compression [163]. This scheme utilizes the Pockels effect of a crystal placed inside a microwave cavity, which therefore cannot be used for UED at the same time but rather requires using an additional identical cavity under the same conditions for electron pulse compression.

In contrast, our approach exploits the energy modulation of electron pulses passing through the microwave cavity [81]. Electrons arriving at different times at the cavity with respect to the microwave's phase gain or lose kinetic energy as a function of the arrival time (cf. section 3.3). The energy transfer is nearly linear with the arrival time around the microwave's zero crossing, which is the intended purpose of the cavity for electron pulse compression (cf. section 3.1). As a consequence, the arrival time is mapped into the kinetic energy of the electrons leaving the cavity,

which constitutes a streak camera, as introduced in section 1.2, yet in the energy domain[1]. The temporal distribution of the arrival times with respect to the microwave's phase can then be measured via an energy analyzer. This yields a convolution between the laser-microwave jitter and the statistical temporal distribution of the electron pulses with respect to the laser pulses, i.e. the effective duration of the electron pulses, as defined in section 2.1. Both contributions are indistinguishable and therefore the electron pulse's duration has to be known or estimated independently in order to obtain the laser-microwave jitter. Note that this microwave streaking technique yields the duration of the electron pulses at the entrance of the cavity if jitter is negligible.

In this chapter, the concept of laser-microwave jitter measurement by microwave streaking is presented, employing a Wien filter as an energy analyzer. The jitter of the synchronized microwave source presented in chapter 4 is characterized with this method and compared with the jitter from two different PLL-VCO sources, demonstrating the ability of this approach for relative assessment of the quality of different microwave sources. The absolute value of the measured timing jitter is limited by the energy resolution and the uncertainties of the theoretical model predicting the duration of the electron pulses at the entrance of the microwave cavity.

5.1 The Wien filter energy analyzer

The experimental arrangement of the microwave streak camera using ultrashort electron pulses is depicted in fig. 5.1. It resembles a simplified version of a UED experiment employing electron pulse compression with a microwave cavity (cf. fig. 1.3 in section 1.4), yet with an energy analyzer instead of a laser-pumped diffraction sample. Single-electron pulses are generated by converting about 0.1 W of 800 nm laser pulses from a Ti:sapphire laser system (cf. section 4.3) at a repetition rate of 5.128 MHz into UV by third harmonic generation. To this end, a frequency tripler (TPL Tripler, Minioptic Technologies, Inc.) is used for collinear second harmonic generation and subsequent sum-frequency generation between the second harmonic and the fundamental light with two thin β-barium-borate crystals and a delay plate which ensures temporal overlap at the sum-frequency generation. The resulting UV pulses at 267 nm wavelength are attenuated to ∼20 pJ of pulse energy and focused onto a 40 nm thin gold photocathode on a quartz substrate, biased at −25 kV. On

[1] The classical streak camera, as shown in fig. 1.1, operates in the transverse domain, i.e. mapping time into a deflection angle or transverse position on the detector, while the TM_{010} mode inside a microwave cavity operates in the longitudinal domain, mapping time into energy. In contrast, the TM_{110} mode, exhibiting a transverse electric field, is sometimes used as a transverse streak camera, similar to the concept shown in fig. 1.1 [70, 124].

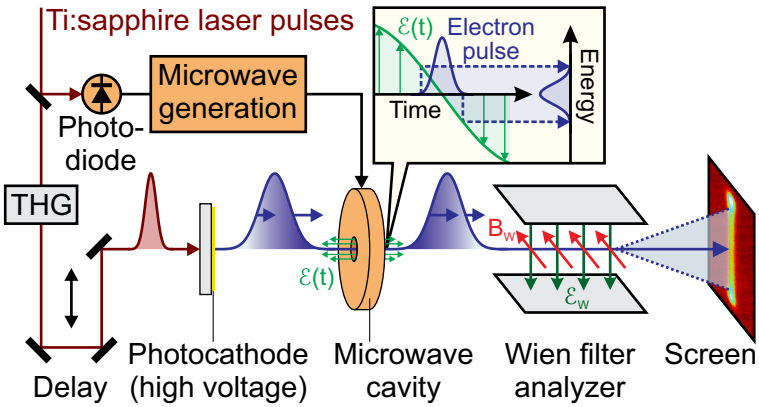

Figure 5.1: Concept of the microwave streak camera using a Wien filter as an energy analyzer. Pulses from a Ti:sapphire laser at a central wavelength of 800 nm are split in two parts. One part is used to generate a microwave signal which is synchronized to the laser's repetition rate via a photodiode (cf. section 5.2). The other part is converted into 267 nm UV pulses by third harmonic generation (THG) and focused onto a gold photocathode. The optical power is attenuated, thus generating not more than one electron per pulse. A static potential of −25 kV is applied to the photocathode, which accelerates the electrons towards the grounded microwave cavity being fed by the synchronized microwave signal. The shading of the depicted electron pulses indicates reversed dispersion and thus compression; i.e. the microwave cavity operates in the same way as in UED experiments (cf. fig. 1.3). A Wien filter, consisting of perpendicularly arranged static electric and magnetic fields ($\mathcal{E}_W$ and B_W, respectively), deflects electrons according to their kinetic energy around the Wien filter's pass energy, which is set to 25 keV by choosing appropriate field strengths. The electrons are then detected on a phosphor screen coupled to a CMOS camera chip and the energy spectrum is extracted from the image after calibration. A pinhole can be inserted before the Wien filter in order to increase the resolution. The inset illustrates the principle of a streak camera in the energy domain, i.e. using the longitudinal microwave field to map the temporal profile of electron pulses into energy.

average, about 0.1 electrons per pulse are generated, ensuring the single-electron regime; i.e. pulses containing more than one electron have a negligible probability (<1 %) according to Poisson statistics. The electrons are accelerated towards the grounded casing of a microwave cavity (cf. section 3.2), which serves as an anode here. The optically enhanced and amplified microwave signal from a photodiode (cf. chapter 4) as well as two PLL-VCO systems (see section 5.2) are employed as microwave sources for driving the cavity and are synchronized to the laser's repetition rate. For each source a photodiode provides an electronic reference of the laser's repetition rate. The UV pulses can be mechanically delayed in order to adjust the relative timing between the electron pulses (generated by the UV) and the microwave's phase inside the cavity.

After passing through the microwave cavity, the electrons enter a Wien filter, which is an arrangement of homogeneous electric and magnetic fields perpendicular to the electron's trajectory and to each other, used as an energy analyzer. Finally, the electron beam is detected on a phosphor screen coupled to a camera chip by fiber optics (TemCam F416, 4096×4096 pixels, 16 bit dynamic range, CMOS technology, TVIPS GmbH).

Wien filters[2] are used as energy analyzers in electron microscopes [165] or as mass spectrometers for ions [166]. This element allows high energy resolution, while maintaining a straight beam line design, in contrast to e.g. bending magnets. The perpendicular electric and magnetic fields are adjusted to compensate each other's forces for the electron's central kinetic energy, here 25 keV, which is referred to as pass energy. Thus, electrons with this energy maintain their trajectory after passing through the Wien filter, while electrons at different energies are deflected according to the resulting Lorentz force. This energy-dependent angular dispersion maps the kinetic energy into a transverse position on the screen, from which the energy spectrum can be retrieved. While the pass energy is set via the ratio of the magnitudes of the electric and magnetic fields, their absolute values define the amount of angular dispersion and hence the energy resolution. For opposite directions of the forces resulting from the electric and magnetic fields inside a Wien filter, $\mathcal{E}_W$ and B_W, respectively, and for small magnitudes of the magnetic field, the acceleration of an electron inside the Wien filter is given by [166]:

$$\frac{\mathrm{d}v_t}{\mathrm{d}t} = \frac{e}{m_\mathrm{e}} \left(\mathcal{E}_W - v_l B_W\right), \tag{5.1}$$

v_t being the electron's transverse velocity, i.e. perpendicular to its initial direction of propagation, v_l its longitudinal velocity, and e and m_e its charge and mass, respectively. The final transverse velocity of a deflected electron at the exit of the Wien filter is then obtained by integrating eqn 5.1 over the drift time spent inside the Wien filter, given by $t_d = d/v_l$, d being the Wien filter's length:

$$v_t = \frac{e}{m_\mathrm{e}} \left(\mathcal{E}_W - v_l B_W\right) t_d = \frac{de}{m_\mathrm{e} v_l} \left(\mathcal{E}_W - v_l B_W\right) \tag{5.2}$$

It is evident from eqn 5.2 that electrons with $v_l = \mathcal{E}_W / B_W$ gain zero transverse velocity and thus are not deflected. This condition describes the pass velocity or equivalently the pass energy, since the kinetic energy, E_kin, is given by $v_l = \sqrt{2E_\mathrm{kin}/m_\mathrm{e}}$

[2] Historically, W. Wien has used parallel electric and magnetic fields simultaneously to identify different types of anode rays (i.e. ion beams) [164]. The perpendicular arrangement has been adapted later for energy and mass spectrometry.

in the non-relativistic case. Thus, the energy-dependent deflection angle α is given by:

$$\tan\alpha = \frac{v_t}{v_l} = \frac{de}{2E_{\mathrm{kin}}}\left(\mathcal{E}_W - \sqrt{\frac{2E_{\mathrm{kin}}}{m_{\mathrm{e}}}}B_W\right) \tag{5.3}$$

The displacement on the screen with respect to the position of zero deflection (i.e. the pass energy) is simply given by $\Delta s = L\tan\alpha$, L being the on-axis distance between the exit of the Wien filter and the screen.

In the experiment, two parallel electrodes provide a homogeneous electric field of about 1 kV/mm and a solenoid attached to an iron yoke of high permeability with a gap perpendicular to the electrodes provides a corresponding magnetic field of about 11 mT, setting the pass energy to 25 keV. The field region is shielded by µ-metal[3] in order to minimize stray fields and a 50 µm pinhole is placed before the Wien filter, which increases the resolution at the expense of a reduced signal.

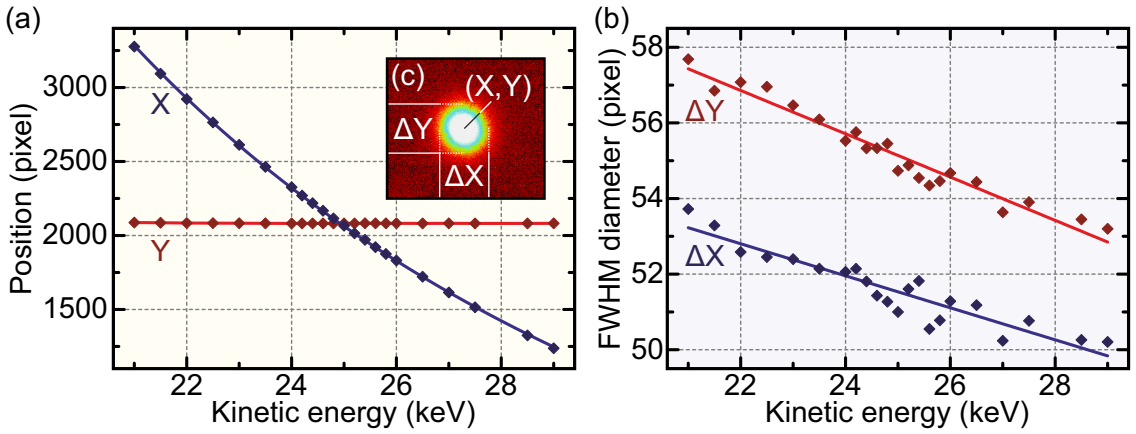

Figure 5.2: Calibration measurement of the Wien filter analyzer. (a) Central position of the electron beam on the screen (the pixel size is 15.6 µm) as a function of the kinetic energy. X (blue diamonds) and Y (red diamonds) denote orthogonal directions, X being chosen along the Wien filter's deflection plane. The solid blue line is a fit according to eqn 5.3. (b) Corresponding FWHM spot widths ΔX (blue diamonds) and ΔY (red diamonds). The solid lines are linear fits. An increasing spot width at lower kinetic energies is a consequence of the electron beam's intrinsic transverse velocity spread (i.e. divergence). (c) A typical camera image of an electron spot after the Wien filter. A 50 µm pinhole is used in front of the Wien filter in order to reduce the spot size, thus increasing the resolution. The geometric quantities (position and width) are determined by fitting a Gaussian surface to the spot.

Since eqn 5.3 describes the ideal energy mapping for well-known field strengths and dimensions, an experimental energy calibration is required for precise energy

[3] µ-metal is a "soft" magnetic nickel-iron alloy (also containing other metals in small quantities) with a very high relative permeability of up to 10^5, typically used for shielding low-frequency magnetic fields.

measurements. To this end, the acceleration voltage is scanned with the microwave cavity being switched off and the electron beam's position on the screen is recorded. Fig. 5.2 shows a typical calibration measurement of the Wien filter analyzer. The spot on the camera, as shown in fig. 5.2 (c), is fitted with a Gaussian surface in order to determine its central position and width. Fig. 5.2 (a) depicts the spot position on the screen (15.6 µm pixel size) along orthogonal directions, X and Y, X being chosen as a direction parallel to the Wien filter's deflection plane. Note that there is no notable deflection along the orthogonal direction Y (red diamonds). The position on the screen is fitted as a function of the kinetic energy using eqn 5.3 (blue line). This provides a calibration which can then be used to convert an arbitrary position on the screen into energy. Although a 50 µm pinhole is used in front of the Wien filter, the spot size on the camera is about 50 pixels or ∼0.8 mm FWHM, as shown in fig. 5.2 (b). This large divergence is caused by inhomogeneous stray fields around the Wien filter, despite the shielding, which act as a defocusing lens. This limits the usable field strengths (currently below the limit of vacuum breakdown) and thus the achievable resolution. An increase of the spot diameter can be seen at lower kinetic energies (i.e. longer total propagation times) due to the electron beam's intrinsic transverse velocity spread. This can be linearly approximated within the scanned energy range (solid lines).

The spot position and width can be determined with sub-pixel accuracy, which is more than one order of magnitude smaller than the typical spot size shown in fig. 5.2 (b). As a consequence, the intrinsic spot width caused by the Wien filter's lensing effect contributes substantially to the spot width measured after microwave streaking. According to the calibration (cf. fig. 5.2 (a)), the intrinsic spot width of about 50 pixels corresponds to a calculated energy spread of ∼200 eV. Since the actual energy bandwidth imprinted by the microwave onto the electrons is considerably smaller for most of the measurements in this work (see section 5.3), the broadening of the spot on the screen is minute compared to its intrinsic width without the microwave. Therefore, the energy-dependent intrinsic spot width shown in fig. 5.2 (b) needs to be removed from the measured width after streaking by deconvolution. The uncertainty of retrieving a small change in width from a large spot size leads to a noise floor of 15 eV–20 eV FWHM or $\sim 10^{-3}$ of the central energy [81], which poses the resolution limit for small bandwidths. At larger bandwidths, the broadening of the spot exceeds the uncertainty of the intrinsic beam size; thus, relative changes are better resolved there. Note that the energy bandwidth of photoemission (<1 eV) is negligible here, contributing less than one pixel to the spot width. This is supported by the round spot shown in fig. 5.2 (c), i.e. having nearly identical widths, ΔX and ΔY, along the deflected and undeflected direction, respectively.

5.2 Synchronized microwave sources

PLL-VCOs are widely used in high-frequency electronics in order to generate a RF signal which is synchronized to a (typically much weaker) reference signal. To this end, a voltage-controlled oscillator generates a signal at a frequency close to the reference signal's frequency. The signal from the oscillator is then mixed with the reference signal in a double-balanced mixer at similar power levels. The mixer's output signal is periodic with the phase difference between the input signals, carrying a beating at the difference frequency between the input signals or a DC voltage if both input signals have the same frequency but a different phase. A loop filter, basically a proportional-integrating circuit, controls the frequency of the oscillator via a low-frequency control voltage (up to several MHz of bandwidth) such that the mixer's output signal is maintained at zero. Effectively, relative timing drift and jitter between the two signals are compensated by the loop filter within its bandwidth. The precision of the loop filter is limited by the accuracy with which the phase difference between the two signals is detected.

In contrast, the passively synchronized and optically enhanced microwave signal extracted from the photodiode (cf. chapter 4) operates without any phase detection or feedback loop. However, the microwave signal contains harmonic components of the laser's repetition rate even after filtering and the available power is limited by saturation of the photodiode. The microwave streak camera introduced in the previous section is capable of assessing the performance of this source in comparison to state-of-the-art PLL-VCO sources.

Fig. 5.3 depicts the three microwave sources used in this work. The source based on direct microwave extraction from a photodiode is shown in fig. 5.3 (a). The optical mode filter enhances the 1209$^{\text{th}}$ harmonic of the laser's repetition rate at 6.2 GHz[4], providing about −15 dBm of microwave power. This is insufficient for electron pulse compression or microwave streaking and therefore the signal is band-pass filtered around 6.2 GHz and amplified in two stages to a power level of up to 33 dBm (2 W). After passing through the two narrow band-pass filters and the microwave cavity (constituting another band-pass filter), the sidebands at ±5.128 MHz are suppressed by about 30 dB with respect to the desired mode at 6.2 GHz. Hence, their contribution to the signal is negligible. A saturating amplifier is used in the first amplification stage in order to minimize amplitude fluctuations.

The microwave source shown in fig. 5.3 (b) is referred to as the 1209$^{\text{th}}$-harmonic-PLL-VCO and has been manufactured by the Budker Institute of Nuclear Physics

[4]The optical mode filter is slightly detuned here compared to section 4.4 in order to match the frequency of the 1209$^{\text{th}}$-harmonic-PLL-VCO system operating at 6.2 GHz, which has been in use prior to the 76$^{\text{th}}$-harmonic-PLL-VCO system operating at 6.237 GHz.

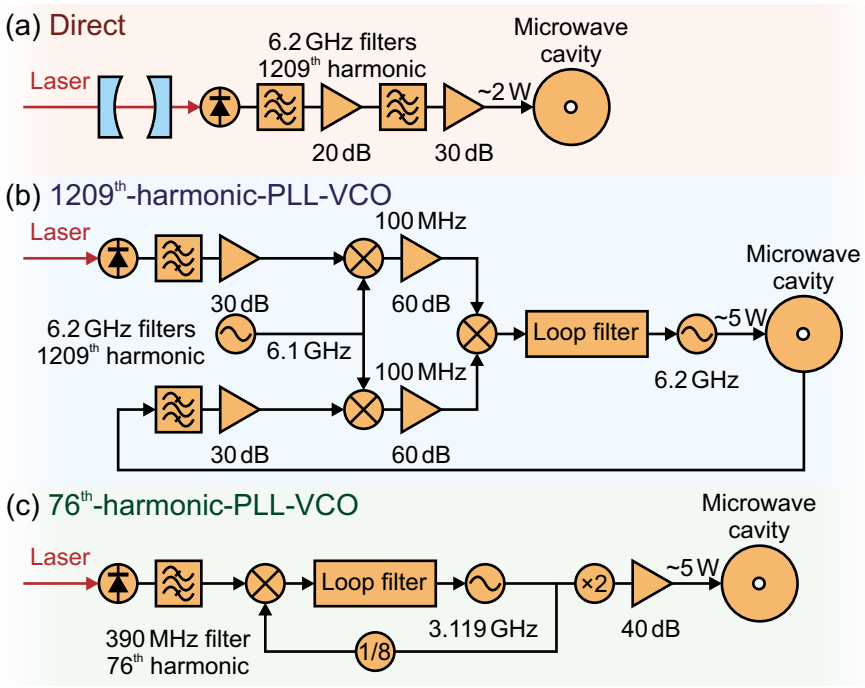

Figure 5.3: Microwave sources used in this work. (a) Optically enhanced direct microwave extraction from a photodiode at the 1209th harmonic of the laser's repetition rate (6.2 GHz). The signal is band-pass filtered and amplified in two stages to a power level of about 2 W. (b) PLL-VCO system at the 1209th harmonic of the laser's repetition rate (6.2 GHz). The signals from a photodiode and from the output port of the microwave cavity are band-pass filtered around 6.2 GHz, amplified, and mixed with a heterodyne signal from a synthesizer at 6.1 GHz, converting both signals down to ∼100 MHz. The 100 MHz signals are amplified and mixed in a double-balanced mixer, providing the phase error signal for a loop filter which controls the frequency of a voltage-controlled oscillator around 6.2 GHz. The oscillator feeds the microwave cavity with about 5 W of power. (c) PLL-VCO system at the 76th harmonic of the laser's repetition rate (simplified diagram). The signal from a voltage-controlled oscillator at 3.119 GHz is split in two parts. One part is frequency-divided by 8 and then mixed with the signal from a photodiode, which is band-pass filtered around 390 MHz. This provides the phase error for a loop filter controlling the oscillator's frequency. The other part of the oscillator's output is frequency-doubled to 6.237 GHz, amplified to about 5 W, and fed into the microwave cavity. A detailed description of this system can be found in [167].

(Novosibirsk, Russia). This system is designed to lock a microwave synthesizer at 6.2 GHz to the 1209th harmonic of the laser's repetition rate obtained from a photodiode without mode filtering. To this end, the signals from the microwave cavity's output port (cf. section 3.2) and the photodiode are band-pass filtered around 6.2 GHz, amplified to a power level of about −30 dBm, and mixed with a signal at 6.1 GHz from an auxiliary synthesizer. The resulting intermediate signals at ∼100 MHz preserve the same absolute frequency and phase difference as before, since they are

both mixed with an identical heterodyne signal at 6.1 GHz. The subsequent high amplification by 60 dB is more convenient at 100 MHz than at microwave frequencies. Finally, both amplified signals are mixed in a double-balanced mixer which provides the phase error signal for a loop filter. The high amplification is required in order to achieve appropriate power levels at the double-balanced mixer, which operates as a phase detector, since the power of the 6.2 GHz signal from the photodiode is between −60 dBm and −50 dBm without mode filtering. The loop filter controls the frequency of a voltage-controlled oscillator around 6.2 GHz, which feeds the microwave cavity and provides about 37 dBm (5 W) of power. Note that this feedback loop scheme is capable of measuring the microwave's phase inside the cavity via the cavity's output port. Both the reference signal from the photodiode as well as the feedback signal from the microwave cavity are processed inside the same temperature-stabilized casing, using identical RF components, and at identical power levels in order to minimize drifts. The oscillator's amplitude is also actively stabilized via a power sensor at the microwave cavity.

The third microwave source is shown in fig. 5.3 (c) and is referred to as the 76^{th}-harmonic-PLL-VCO. It is a customized commercial system (PLL Synchronizer, AccTec B.V.), originally designed to operate around 3 GHz [126, 167]. Here, the feedback signal is taken directly from a voltage-controlled oscillator operating at around 3.119 GHz, frequency-divided by 8, and mixed in a double-balanced mixer with the signal from a photodiode, which is band-pass filtered around the 76^{th} harmonic of the laser's repetition rate (390 MHz). This provides the phase error signal for a loop filter which controls the oscillator's frequency. A photodiode of lower bandwidth and higher saturation threshold can be used at this frequency, offering significantly more RF power than the fast photodiode used for the other two approaches. Hence, less amplification is required for appropriate power levels at the double-balanced mixer (see [167] for details). The output of the oscillator is frequency-doubled to 6.237 GHz, providing about −3 dBm of power, which is further amplified by 40 dB to a power level of about 37 dBm (5 W). Due to the internal feedback, this PLL-VCO is not capable of compensating drift of the microwave cavity's phase and therefore precise environmental stabilization of the cavity is required. Using an intermediate frequency for the phase-locked loop is favorable in terms of electronic noise, since the thermal noise floor of the photodetection (cf. section 4.1) is reduced and less amplification is needed. However, the phase detection operates only at 1/16 of the output frequency here and therefore the required accuracy is 16 times higher than for phase detection at the final microwave frequency. Note that the output frequency of the 76^{th}-harmonic-PLL-VCO is thus restricted to multiples of $5.128\,\text{MHz} \cdot 16 \approx 82\,\text{MHz}$, 5.128 MHz being the laser's repetition rate. Consequently, 6.237 GHz, based on the 76^{th} harmonic of the laser's repetition rate, is closest to the frequency of the other

two systems (6.2 GHz), for which the 1209$^{\text{th}}$-harmonic-PLL-VCO has been initially designed. The resonance frequency of the microwave cavity can be adjusted between these two values via a tuning pin (cf. section 3.2).

The PLL-VCO systems presented here are locked to the repetition rate of a free running laser oscillator. Alternatively, a phase detector and a loop filter can also be used to lock the laser's repetition rate to a stable microwave source by modulating the length of the laser's cavity. We employ the former approach, since mechanical modulation of the laser's cavity length by means of a high-frequency piezo actuator is technically more intricate and the control bandwidth is smaller compared to a voltage-controlled microwave oscillator [167]. Moreover, the range of frequency tuning is very limited for a piezo actuator and might require an additional (slow) translation stage in order to implement a large tuning range, e.g. for compensating temperature drift. Although a microwave reference can be more stable against slow temperature drift, a femtosecond mode-locked laser oscillator has usually a superior high-frequency phase noise performance (cf. section 4.3 and fig. 4.4).

5.3 Microwave streaking results

Fig. 5.4 shows some typical microwave streaking images obtained with the 1209$^{\text{th}}$-harmonic-PLL-VCO and electron pulses at 25 keV after 10 s of exposure time for each image. The line profiles in the right panels show the raw data converted to energy using eqn 5.3 and the calibration from fig. 5.2 (a) but without deconvolution of the intrinsic beam size from fig. 5.2 (b). Hence, the widths of the line profiles do not represent the actual energy spreads but rather are intended to supplement the images in the left panels. Fig. 5.4 (a) depicts the raw image and retrieved energy spectrum with a free running microwave oscillator, i.e. without synchronization. The microwave's phase inside the cavity is random for each electron pulse and therefore the energy spectrum contains all energy values accessible by the interaction with the microwave. The shape resembles the cycle-averaged probability distribution (or histogram) of the magnitude of the sinusoidal microwave field inside the cavity. The two peaks represent the most frequent microwave phases of highest energy gain or loss, i.e. the extrema of the energy modulation curve, and the maximum energy modulation can be inferred from their separation (several keV). The asymmetry of the intensity is caused by the energy-dependent sensitivity of the phosphor screen which is more sensitive at higher energies.

Fig. 5.4 (b)–(d) show streaking images with activated laser-microwave synchronization of the PLL-VCO. When the microwave's phase is set at the compressing zero crossing, as shown in fig. 5.4 (b), the central energy is unchanged. However, an increased spot size is evident along the the Wien filter's deflection plane compared

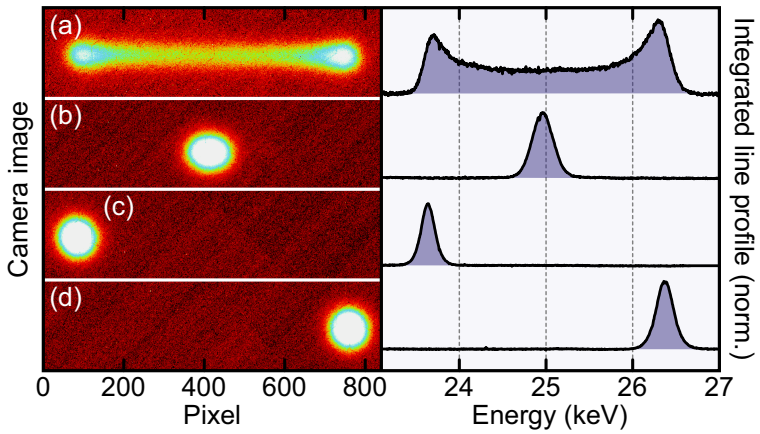

Figure 5.4: Raw images and converted energy spectra for different conditions of the microwave field, obtained with the 1209$^{\text{th}}$-harmonic-PLL-VCO and electron pulses at 25 keV. (a) Without synchronization, each electron pulse interacts with the microwave at a random phase. Thus, an energy spectrum is produced which covers all energies accessible by the interaction with the microwave. The shape resembles the probability distribution, i.e. the histogram, of the sinusoidal microwave field inside the cavity. (b) The PLL-VCO is synchronized to the laser's repetition rate and the microwave's phase is set to the compressing zero crossing. The central energy is unchanged; however, energy broadening is visible, indicating a temporal spread or timing jitter of the electron pulses at the microwave cavity. The microwave's phase is shifted by $\pm 90°$ in (c) and (d), respectively, showing a shift of the central energy but no apparent energy broadening. Note that the right panels show integrated line profiles of the raw data, converted to energy using eqn 5.3. No deconvolution of the intrinsic beam size is applied here; hence the widths of the line profiles do not represent the actual energy spreads.

to the perpendicular direction, indicating a significant energy spread and therefore temporal spread or jitter of the electrons with respect to the microwave's phase as they enter the cavity. The images in fig. 5.4 (c) and (d) are obtained at phase shifts of $\pm 90°$. The central energy is shifted towards the maximum and minimum values corresponding to the peaks in fig. 5.4 (a); however, no apparent energy broadening is visible. As expected, microwave streaking, like electron pulse compression, works best around a zero crossing of the energy modulation curve where the rate, i.e. the temporal derivative, of the energy transfer is highest. Note that electron pulse compression only takes place at one of the two possible zero crossings at which the leading electrons are decelerated, while the trailing ones are accelerated (cf. section 3.1). The correct zero crossing can be easily identified with the microwave streak camera by scanning the delay between the electron pulses and the microwave's phase around the zero crossing of the energy modulation curve.

Fig. 5.5 shows such delay measurements and the evaluated FWHM temporal spreads for the three microwave sources used in this work, covering more than one period of the microwave. The results for the 1209$^{\text{th}}$-harmonic-PLL-VCO source are

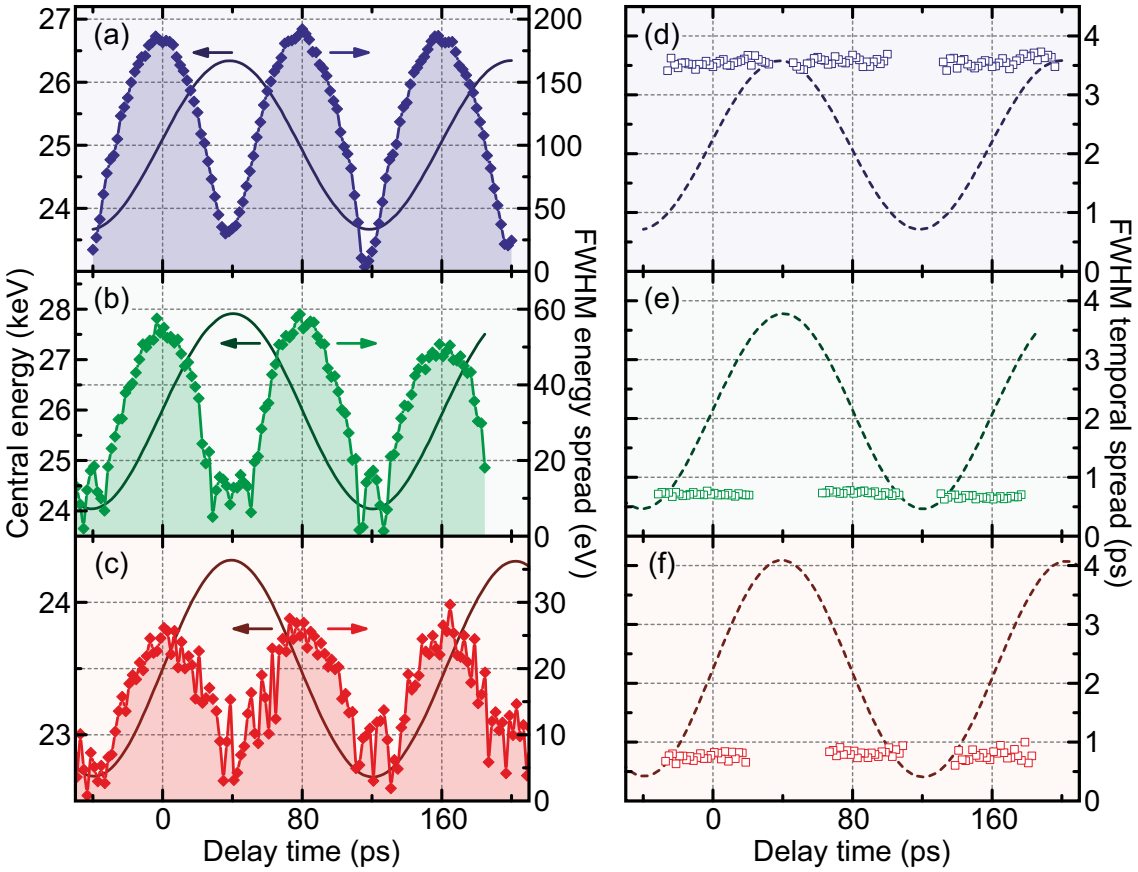

Figure 5.5: Delay scan between the electron pulses and the microwave's phase for the three different microwave sources. The left panels show the central energy of the electrons (solid lines) and their FWHM energy spread (diamonds), while the right panels show the FWHM temporal spread (squares) calculated from the energy spread and the temporal derivative of the respective energy modulation. The dashed lines reproduce the central energy modulation curves, taken from the corresponding left panels, as guides to the eye. The intrinsic beam size is deconvoluted from the measured spot widths, yielding the actual energy and temporal spreads. (a) and (d): 1209$^{\text{th}}$-harmonic-PLL-VCO, (b) and (e): 76$^{\text{th}}$-harmonic-PLL-VCO, (c) and (f): direct extraction source.

shown in fig. 5.5 (a) and (d), for the 76$^{\text{th}}$-harmonic-PLL-VCO source in fig. 5.5 (b) and (e), and for the passive direct microwave extraction source in fig. 5.5 (c) and (f), respectively. The solid lines in fig. 5.5 (a)–(c) depict the modulation of the central energy, $E(t)$, of the electrons by the microwave. Zero delay time is chosen at the compressing phase, i.e. where leading (early) electrons are decelerated and trailing (late) electrons are accelerated, while the central energy is unchanged. Note that the amplitude of the energy modulation is different for the three microwave sources, reflecting the available microwave power. Also, slightly different acceleration voltages are used for the different sources: 25 kV for the 1209$^{\text{th}}$-harmonic-PLL-VCO source,

26 kV for the 76$^{\text{th}}$-harmonic-PLL-VCO source, and 23.5 kV for the direct extraction source.

The energy spread (diamonds) is determined as FWHM for each delay step by deconvolution of the intrinsic beam size from the measured spot width using the according calibration, as shown in fig. 5.2 (b). As suggested by fig. 5.4, the energy spread is largest at the zero crossings of the energy modulation curve and smallest at the extrema, where it drops below the detection noise floor (cf. section 5.1). Since the temporal spread of the electron pulses with respect to the microwave's phase, τ_{e}, stays constant during the delay scan, the energy spread, $\Delta E(t)$, at a particular delay time is given by the temporal derivative of the energy modulation curve, $g_E(t) = \mathrm{d}E(t)/\,\mathrm{d}t$ (in units of eV/ps):

$$\Delta E(t) \approx \left| g_E(t) \tau_{\text{e}} \right| , \tag{5.4}$$

as long as τ_{e} is small compared to the period of the microwave and the initial energy bandwidth of photoemission (<1 eV) is negligible. The rate of energy gain, g_E, is also referred to as microwave compression strength, since it determines the energy or velocity spread imprinted onto the electrons and hence the position of the temporal focus when used at the compressing phase (see section 7.2).

The temporal spread of the electron pulses, calculated according to eqn 5.4, is shown in fig. 5.5 (d)–(f) as squares. In order to evaluate the temporal spread by streaking, a single measurement of the energy spread and the according rate of energy gain, g_E, is sufficient – preferably at the zero crossing of the energy modulation curve, where g_E and thus the induced energy spread are highest. Here, the temporal spread is evaluated over the entire delay scan for improved statistics, with the exception of the extrema of the energy modulation curve, where g_E becomes small and the energy spread drops below the noise floor of the detection. We obtain $\tau_{\text{e}} = (3560 \pm 100)$ fs for the 1209$^{\text{th}}$-harmonic-PLL-VCO, $\tau_{\text{e}} = (715 \pm 50)$ fs for the 76$^{\text{th}}$-harmonic-PLL-VCO, and $\tau_{\text{e}} = (800 \pm 150)$ fs for the direct extraction source (all values denote FWHM). The two latter approaches produce nearly identical results, despite their different conceptions, and clearly show a better performance than the former one. The streaking results are summarized in table 5.1.

The duration τ_{e}, obtained by microwave streaking, constitutes a convolution between the temporal spread of the dispersed electron pulses entering the microwave cavity (cf. sections 2.2 and 3.1) and the laser-microwave timing jitter. According to fig. 3.1, the initial duration of the electron pulses after photoemission, τ_{initial}, is given by the duration of the laser pulses used to generate the electron pulses. Dispersion broadens the pulses during static acceleration by τ_{acc}, as described in eqns 3.3 and 3.4, to a total dispersed duration of the electron pulses, τ_{disp}, with

Microwave source	Acc. field (kV/mm)	Max. g_E (eV/ps)	Max. ΔE (eV)	τ_e (fs)
1209^{th}-harmonic-PLL-VCO	1.71 ± 0.06	51.8 ± 0.2	184 ± 6	3560 ± 100
76^{th}-harmonic-PLL-VCO	2.11 ± 0.08	73.8 ± 0.5	53 ± 4	715 ± 50
Direct extraction source	1.91 ± 0.08	32.1 ± 0.1	26 ± 5	800 ± 150

Table 5.1: Microwave streaking results for three different microwave sources, showing the static acceleration field, the maximum energy gain rate, g_E, and energy spread, ΔE, at the zero crossing of the energy modulation curve, and the resulting temporal spread, τ_e. The spreads denote FWHM.

respect to the timing of the laser pulses. Timing jitter between the laser's repetition rate and the microwave's phase further broadens the temporal spread of the electron pulses by τ_{jitter}, yielding a measured duration, τ_e, of:

$$\tau_e^2 = \tau_{\text{initial}}^2 + \tau_{\text{acc}}^2 + \tau_{\text{jitter}}^2 = \tau_{\text{disp}}^2 + \tau_{\text{jitter}}^2 \tag{5.5}$$

Here, eqn 3.4 is substituted in eqn 5.5. The duration of the 267 nm UV laser pulses used for photoemission is estimated as $\tau_{\text{initial}} = (90 \pm 20)$ fs FWHM, based on the measured spectral bandwidth and the calculated optical dispersion of the vacuum window. The amount of dispersive broadening, τ_{acc} (cf. eqn 3.3), depends on the initial energy spread, the static acceleration field, and the assumed shape of the initial velocity or energy distribution, as pointed out in section 3.1. Literature offers different models to calculate τ_{acc} [78, 80, 82, 100, 114], which are based on eqn 3.3, yet differ by a factor of up to $\sim\sqrt{2}$, owed to different assumptions about the initial velocity or energy distribution. An initial energy spread of typically 0.2 eV FWHM and a static acceleration field of $\mathcal{E}_{\text{acc}} = 2\,\text{kV/mm}$ then yield a FWHM temporal broadening between $\tau_{\text{acc}} \approx 520\,\text{fs}$ [100] and $\tau_{\text{acc}} \approx 750\,\text{fs}$ [78]. When assuming a half-spherical distribution of the photoemission with a normal probability distribution of the kinetic energies, the temporal broadening lies in between. The initial energy bandwidth, $\Delta\varepsilon$, then denotes the width of the probability function at half maximum and eqn 3.3 can be rewritten according to [82] as:

$$\tau_{\text{acc}} \approx \frac{\sqrt{\sqrt{2} m_e \Delta\varepsilon}}{e\mathcal{E}_{\text{acc}}} \tag{5.6}$$

The work function of the 40 nm thin gold photocathode is ~4.2 eV [99] (cf. section 1.4) and the photon energy of the 267 nm UV laser pulses is 4.65 eV. The resulting FWHM energy spread of the photoelectrons is between 0.2 eV and 0.3 eV, estimated from the beam's divergence according to the model described in [82].

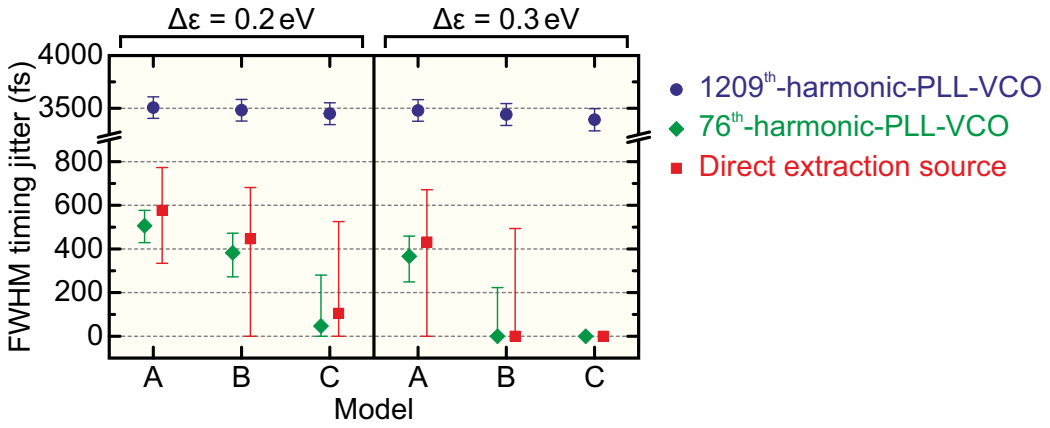

Figure 5.6: Deconvoluted FWHM timing jitter for the three different microwave sources and for different dispersion models, assuming an initial energy spread of $\Delta\varepsilon = 0.2\,\mathrm{eV}$ (left) and $\Delta\varepsilon = 0.3\,\mathrm{eV}$ (right), respectively. The 1209$^{\mathrm{th}}$-harmonic-PLL-VCO (blue dots) clearly exhibits a jitter above 3 ps, while the jitter of the other two microwave sources is comparable to the experimental and model uncertainties. This yields an upper limit of the jitter of 580 fs for the 76$^{\mathrm{th}}$-harmonic-PLL-VCO (green diamonds) and 770 fs for the direct microwave extraction source (red squares). Dispersion models: A [100], B [82] (cf. eqn 5.6), C [78].

The laser-microwave timing jitter can then be deconvoluted from the measured temporal spread using eqn 5.5. The uncertainties arising from the applied dispersion model and the initial energy spread are substantial and limit the precision of a quantitative assessment of the jitter. Fig. 5.6 shows the FWHM laser-microwave timing jitter, deconvoluted from the streaking measurement, for the three microwave sources using different dispersion models and assuming an initial FWHM energy spread of $\Delta\varepsilon = 0.2\,\mathrm{eV}$ and $\Delta\varepsilon = 0.3\,\mathrm{eV}$, respectively. The error bars arise from experimental uncertainties of τ_{e} (cf. table 5.1) and τ_{initial}. The FWHM timing jitter of the 1209$^{\mathrm{th}}$-harmonic-PLL-VCO (blue dots) lies between 3300 fs and 3600 fs within the error margins of both experimental and model uncertainties, revealing a poor synchronization of this microwave source. In contrast, the FWHM timing jitter of the other two approaches appears to be on the order of the electron pulse's duration at the microwave cavity, τ_{disp}, or below. Here, the experimental and model uncertainties are comparable in magnitude to the deconvoluted jitter, thus yielding only an upper limit of the jitter. We obtain $\tau_{\mathrm{jitter}} \leq 580\,\mathrm{fs}$ FWHM for the 76$^{\mathrm{th}}$-harmonic-PLL-VCO (green diamonds) and $\tau_{\mathrm{jitter}} \leq 770\,\mathrm{fs}$ FWHM for the direct microwave extraction source (red squares) within all error margins.

The timing jitter of a PLL-VCO source [167] very similar to the 76$^{\mathrm{th}}$-harmonic-PLL-VCO used in this work has been determined before by single-shot streaking [70] and by direct laser-microwave phase detection inside a microwave cavity [163]. In both cases the jitter is $\leq$100 fs rms (or $\leq$240 fs FWHM for a Gaussian distribution

of the timing noise), indicating that the jitter of the 76$^{\text{th}}$-harmonic-PLL-VCO is below the resolution limit of the microwave streak camera presented in this chapter. The direct extraction source yields a similar value for the upper limit of the jitter with a slightly higher uncertainty due to less available microwave power and thus a smaller value of g_E. Therefore, the actual jitter of the direct extraction source is also very likely below the resolution limit of the streak camera, as concluded for the 76$^{\text{th}}$-harmonic-PLL-VCO. This is supported by the estimations in section 4.5, predicting a high-frequency timing jitter on the order of some tens of femtoseconds in addition to slow timing drift, which is not measured here (see section 6.3).

5.4 Limitations of microwave streaking

Absolute assessment of laser-microwave jitter by microwave streaking is limited by three factors: First, the jitter and the electron pulse's duration at the entrance of the microwave cavity are added quadratically (cf. eqn 5.5); therefore, uncertainties start to dominate when these values become comparable. For the same reason the minimum energy detectable with the Wien filter is limited by the electron beam's size (cf. section 5.1). Thus, the electron pulse's duration, τ_{disp}, roughly limits the minimum measurable jitter and constitutes a noise floor of the measurement. In contrast, if the jitter is considerably larger than τ_{disp}, as in the case of the 1209$^{\text{th}}$-harmonic-PLL-VCO, the uncertainties are less significant and the measurement is more precise. Therefore, the microwave streak camera presented in this chapter is readily capable of assessing jitter on the order of picoseconds with high precision. In order to resolve femtosecond jitter, however, reducing τ_{disp} is crucial. Using the highest possible static acceleration field (about 10 kV/mm) and minimizing the initial energy spread, $\Delta\varepsilon$, by tuning the wavelength of the UV laser pulses close to the photocathode's work function promises $\tau_{\text{disp}} \approx 70$ fs FWHM [82].

Secondly, the dispersion model applied for calculating τ_{acc} introduces a relative uncertainty of $\sim\sqrt{2}$. Although eqn 5.6 is based on a reasonable assumption about the initial velocity distribution of the photoelectrons [82], the actual distribution might differ. A precise measurement, e.g. by energy and angular resolved photoemission electron microscopy [168], can facilitate accurate modeling of the dispersion.

Thirdly, the energy resolution of the Wien filter limits the shortest measurable temporal spread for a given microwave amplitude or g_E. Currently, the energy resolution is limited by the beam size, the maximum applicable field strength inside the Wien filter, and stray fields. An improved energy analyzer with a FWHM resolution of $\sim$1 eV (see chapter 6) is capable of measuring a timing jitter on the order of some tens of femtoseconds, given a short enough τ_{disp}.

Characterization of the dispersed electron pulses in the time domain can provide τ_{disp} directly without the need for modeling. Suitable techniques include transverse streak cameras [70, 169, 170], ponderomotive scattering [96, 171], or the recently developed optical field streaking technique [93]. Certainly, the laser-microwave jitter can be characterized by these techniques as well, rather than by microwave streaking, if the additional effort is acceptable. The temporal resolution of optical field streaking is even sufficient for characterization of compressed electron pulses in the 10 fs range (see chapter 7). Nevertheless, the microwave streaking technique presented here constitutes an efficient method for assessing the quality of different microwave sources, while effectively only using components which are already required for UED with electron pulse compression, besides the Wien filter analyzer. In a first experiment, the 1209^{th}-harmonic-PLL-VCO has been identified as incapable of femtosecond synchronization, owing to excessive noise in the amplifiers, while the 76^{th}-harmonic-PLL-VCO and the passively enhanced direct microwave extraction source potentially offer a sufficient quality of synchronization for electron pulse compression.

Chapter 6

High-resolution time-of-flight spectrometer for sub-relativistic electron pulses

The energy domain offers powerful and versatile possibilities for characterization of ultrashort electron pulses for UED, especially if microwave compression is employed. Energy-resolved analysis has been demonstrated in the previous chapter by means of a microwave streak camera, constituting a precise laser-microwave phase detector capable of measuring sub-picosecond timing jitter as a first application. Time-resolved spectroscopy of the electron pulses by optical field streaking [93] (see chapter 7) can provide a time-domain characterization as well as a visualization of the phase space transformations imposed by vacuum dispersion and microwave compression. Besides UED, ultrafast electron energy loss spectroscopy (EELS), usually in combination with an electron microscope in order to resolve nanostructures, can provide further insight into structural and electron dynamics in matter [97, 172–175].

These applications rely on a high-resolution energy analyzer suitable for electron pulses at sub-relativistic energies (tens of keV). The Wien filter analyzer (cf. section 5.1) is not capable of detecting few-femtosecond drift or jitter when operated as a laser-microwave phase detector, since the energy resolution is limited by a noise floor of about 20 eV. For a typical rate of energy gain from the microwave, g_E, of 50 eV/ps, an energy resolution of 0.5 eV is required in order to detect a timing drift of 10 fs. Also, the pinhole significantly reduces the usable signal, which particularly affects low-signal applications, such as optical field streaking or EELS.

Here, we introduce a home-built time-of-flight (ToF) spectrometer for sub-relativistic electron pulses with an energy resolution of well below 1 eV FWHM over a range of more than 10 eV at up to 30 keV of central energy. Nearly the entire signal can be used with little loss by employing collimating electron optics with-

out the need for an aperture. In this chapter, the conception, construction, and characterization of this instrument is presented. The ToF spectrometer replaces the previously used Wien filter analyzer as a laser-microwave phase detector in order to measure laser-microwave timing drift with few-femtosecond precision. Furthermore, this spectrometer is used in the experiments described in chapter 7 for time-domain characterization of uncompressed and compressed electron pulses.

6.1 Conception and design

Fig. 6.1 depicts the concept of a ToF spectrometer, which is based on a precise measurement of the arrival times of electron pulses at a detector with respect to a timing reference. As a consequence, a ToF spectrometer necessarily operates in pulsed mode, while transverse deflecting energy analyzers, such as the Wien filter (cf. section 5.1), also accept continuous beams of charged particles. Both types of spectrometers can be integrated into an existing UED experiment with manageable effort. Besides the aforementioned advantages of low signal loss and substantially higher resolution compared to the Wien filter analyzer, the single-shot nature of a ToF spectrometer also allows evaluating drift and noise in real-time on a shot-to-shot basis.

An electron gun, consisting of a photocathode, a region of static acceleration to some tens of keV of kinetic energy, and a solenoid for collimation [87] (cf. fig. 1.3 in section 1.4), generates ultrashort electron pulses using femtosecond laser pulses for photoemission. An electronic time-to-digital converter (TDC) measures the arrival time of each electron pulse at a micro-channel plate (MCP) detector with respect to a start signal which is triggered via a photodiode by a portion of the laser pulse used for photoemission. At 30 keV of central energy, an energy spread of 1 eV transforms into a temporal spread of ∼160 fs over a length of 1 m, which is not detectable by electronics. The temporal resolution of a state-of-the-art TDC is on the order of 200 ps FWHM, limited by the speed of the digital electronics as well as the analog bandwidth of the MCP detector which converts impinging electron pulses into short current pulses. Therefore, the central energy of the electron pulses needs to be substantially reduced, allowing the electrons to acquire sufficient temporal dispersion in order to achieve the desired energy resolution at the given temporal resolution of the detector. To this end, a high-voltage drift tube is employed, which is biased nearly at the same high negative potential as the photocathode. The electrons are thus strongly slowed down inside the drift tube, gaining the desired temporal dispersion, and accelerated afterwards again towards the grounded detector.

A commercial MCP detector is used in this work (MCP 3636, Surface Concept GmbH), providing a digital time bin size of 27.4 ps and an impulse response of

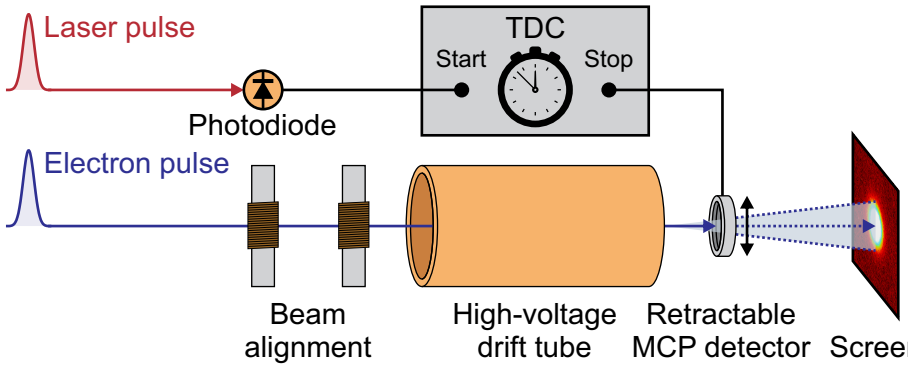

Figure 6.1: Concept of a ToF spectrometer for sub-relativistic electron pulses. Femtosecond laser pulses are used to generate ultrashort electron pulses (cf. the electron gun in fig. 1.3). A single-shot time-to-digital converter (TDC) measures the time between a start signal, triggered by the laser pulse via a photodiode, and a stop signal from a micro-channel plate (MCP) detector, triggered upon the arrival of an electron pulse. The electronic time resolution of the TDC is about 200 ps FWHM; therefore, the electrons are slowed down in a high-voltage drift tube in order to acquire sufficient temporal dispersion for the desired energy resolution. Two pairs of electromagnetic steering coils are used for precise alignment of the electron beam along the drift tube's axis. The MCP detector is retractable and a phosphor screen coupled to a CMOS camera chip behind the detector is used to monitor the beam geometry during alignment. The energy spectrum can be extracted from the ToF measurement provided by the TDC after calibration.

about 200 ps FWHM. The MCP stack is biased at about −2.5 kV and exhibits an active area with a diameter of 36 mm. Electrons impinging on the MCP release an avalanche of secondary electrons in the micro-channels, which are accelerated towards an underlying anode. This creates a current pulse which is subsequently amplified and detected by the electronics at a rate of up to 7 MHz. The detector consists of four quadrants, each being an individual anode, which allows for rough spatial resolution of the electron beam. In order to align the electron beam precisely along the axis of the drift tube, the MCP detector can be retracted, allowing the beam geometry to be monitored on a phosphor screen coupled to a CMOS camera chip (cf. section 5.1). Two pairs of deflecting electromagnetic coils are used for beam steering in front of the drift tube.

Slowing down the electron pulses inside a drift tube can in principle arbitrarily enhance the energy resolution by reducing the central kinetic energy almost to zero and thus arbitrarily increasing the temporal dispersion. However, this applies only to an infinitely thin and non-divergent electron beam along the drift tube's axis. A cylindrical drift tube constitutes an electrostatic lens for a realistic electron beam of a finite diameter and divergence. Thus, electrons entering the drift tube nonparallel or at a distance to the axis exhibit trajectories differing from the straight line of ideal

on-axis electrons and hence a larger ToF at the same kinetic energy. Therefore, the benefit of temporal dispersion inside a drift tube is to some extent compensated by the drift tube's geometrical effect on the trajectories of the electrons, i.e. the width of a ToF spectrum is constituted of both the energy spread and the beam's geometry inside the drift tube. Since both contributions are indistinguishable, the geometry-related broadening of the ToF poses a limit to the achievable energy resolution.

The practical design of the drift tube is defined by its diameter and length. A long drift tube provides more temporal dispersion than a short one; however, the length is limited in this work to 200 mm due to the dimensions of the vacuum chamber. For the diameter, there is an optimum choice: The electrostatic lensing effect becomes weaker for a larger diameter; however, the electric potential inside the drift tube is more homogeneous for a smaller diameter at a given length. In order to determine the achievable energy resolution and the optimum diameter of the drift tube, particle tracking simulations are performed using a finite element software (COMSOL, Inc.). Fig. 6.2 (a) shows an on-axis cross-section of the geometry used for the simulation (black). Note that the geometry has cylindrical symmetry around the axis. The drift tube (inner cylinder) is biased at −30 000 V, while the casing (outer cylinder) is grounded. The calculated electric potential (color-coded) is homogeneous and at a high negative value inside the drift tube. A lensing effect is evident as curvature of the electric potential at the openings of the drift tube. The dimensions of the casing are chosen to minimize stray fields outside the drift tube and inhomogeneities of the electric potential at the openings, complying with the physical constraints of the vacuum chamber.

The results of particle tracking inside the calculated electric potential are depicted as white trajectories for a collimated monoenergetic electron beam with a diameter of 1.9 mm at a kinetic energy of 30 002 eV. The electrons are thus slowed down to a kinetic energy of ∼2 eV inside the drift tube. At this reduced kinetic energy, an energy difference of 0.1 eV leads to a ToF difference of about 5.7 ns over the drift tube's length of 200 mm, which is well within the temporal resolution of the MCP detector. However, the electrostatic lensing effect at the openings of the drift tube leads to different trajectories for off-axis electrons of the same kinetic energy, as evident in fig. 6.2 (a). The simulated ToF as a function of the kinetic energy is shown in fig. 6.2 (b) for the on-axis trajectory (blue) and for a trajectory 0.9 mm off-axis at the entrance of the drift tube (green), representing the outer trajectories in fig. 6.2 (a). The ToF curves differ roughly by an offset of 2 ns and diverge for kinetic energies approaching the potential energy of the drift tube (30 000 eV), referred to as the threshold energy, E_{th}. The temporal dispersion per unit of energy bandwidth is directly given by the derivative of the ToF curves with respect to energy; thus, the energy resolution, $R(E)$, is strongly energy-dependent and highest close to the

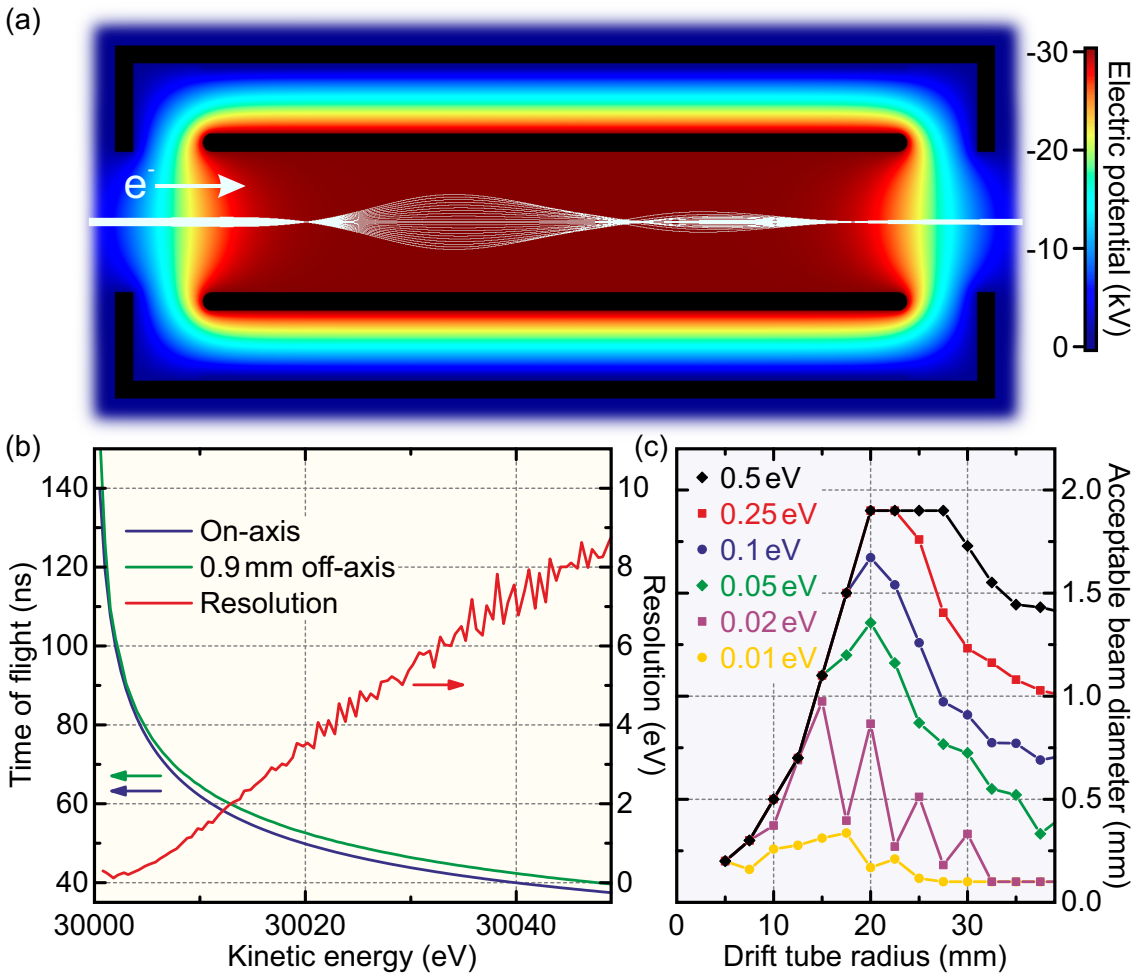

Figure 6.2: Drift tube geometry and particle tracking results. (a) On-axis cross-section through the drift tube (inner cylinder) and its casing (outer cylinder), indicated in black. The drift tube is biased at −30 000 V, while the casing is grounded; the calculated electric potential is color-coded. The white traces depict a collimated monoenergetic electron beam with a diameter of 1.9 mm at a kinetic energy of 30 002 eV. Different trajectories imply different ToF values. (b) ToF as a function of the kinetic energy for the on-axis trajectory (blue) and for a trajectory 0.9 mm off-axis at the entrance of the drift tube (green), representing the outer trajectories in (a). The energy resolution (red) is defined as the ToF difference between the two trajectories, convoluted with the MCP detector's temporal resolution, divided by the average derivative of the ToF curves with respect to energy (see eqn 6.1). The best (i.e. minimum) energy resolution of ∼0.2 eV is achieved over a narrow energy range of up to 3 eV above the threshold energy corresponding to the drift tube's potential ($E_{th} \approx 30\,000$ eV). (c) Maximum acceptable beam diameter as a function of the drift tube's radius for different achievable energy resolutions (between 0.01 eV and 0.5 eV). The optimum radius of the drift tube in order to achieve an energy resolution of 0.1 eV is thus 20 mm, facilitating a beam diameter of up to 1.7 mm. Note that the beam diameter is clipped at 1.9 mm, since the trajectories are only simulated up to this value.

threshold energy. It is given by the ToF difference between the two trajectories at a particular energy E, convoluted with the MCP detector's temporal resolution, τ_{det}, divided by the average derivative of the ToF curves with respect to energy:

$$R(E) = \frac{2\sqrt{\left(t_{\text{off-axis}}(E) - t_{\text{on-axis}}(E)\right)^2 + \tau_{\mathrm{det}}^2}}{\left|\frac{\mathrm{d}t_{\text{off-axis}}(E)}{\mathrm{d}E} + \frac{\mathrm{d}t_{\text{on-axis}}(E)}{\mathrm{d}E}\right|}, \tag{6.1}$$

$t_{\text{on-axis}}(E)$ and $t_{\text{off-axis}}(E)$ being the ToF of the on-axis and off-axis electron trajectory, respectively. The resolution, calculated from numerical derivatives of the ToF curves and assuming $\tau_{\mathrm{det}} = 150\,\mathrm{ps}$ FWHM, is shown in fig. 6.2 (b) in red. The minimum value is $\sim$0.2 eV over a narrow energy range of up to 3 eV above E_{th}. This curve denotes the FWHM resolution for a FWHM beam diameter of 1.8 mm in the case of a Gaussian profile of a collimated electron beam.

In fig. 6.2 (c), the maximum acceptable beam diameter is shown as a function of the drift tube's radius for different achievable energy resolutions (between 0.01 eV and 0.5 eV). The curves denote beam diameters which yield the same value for the best (i.e. minimum) achievable resolution. An optimum radius of the drift tube is evident, which slightly shifts towards higher values for worse (i.e. larger) target resolutions. Note that the beam diameter is clipped at 1.9 mm, since the trajectories are only simulated up to this value. A 20 mm radius of the drift tube is chosen for manufacturing, which is optimized for a resolution of 0.1 eV, allowing a beam diameter of up to 1.7 mm, which is easily achievable with a collimating magnetic lens. The achievable resolution scales in the same way with the beam's divergence as with its diameter, yielding the same optimum radius of the drift tube at a maximum acceptable divergence of about 4 mrad for an infinitely thin beam. A realistic beam has both a finite diameter and divergence; hence, the maximum acceptable beam diameter is reduced at a simultaneously present divergence, reflecting the conservation of emittance (cf. sections 1.4 and 2.1). A beam diameter of 1 mm thus allows for a maximum divergence of about 2.4 mrad in order to maintain an energy resolution of 0.1 eV.

Since the drift tube is biased at a high negative voltage, it is held inside the grounded casing cylinder via ceramic spacers. The edges are rounded in order to minimize local fields at the surface, which are enhanced by sharp edges and surface roughness and can cause arcing due to vacuum breakdown. A high-voltage connection is provided through a hole at the side of the casing. At the low kinetic energies inside the drift tube, external magnetic fields, especially earth's magnetic field, can substantially alter the trajectories of the electrons. Thus, the drift tube's casing is shielded by $\sim$1 mm of µ-metal, providing a nearly magnetic-field-free region inside the drift tube.

6.2 Calibration and resolution

For the precise alignment of the electron beam along the axis of the drift tube, the electrostatic lensing effect is utilized by monitoring the beam's shape and position on the camera, while slowly increasing the negative voltage applied to the drift tube. After the desired voltage is reached and the beam is properly aligned, the MCP detector is inserted into the beam and ToF spectra can be recorded. Fig. 6.3 (a) depicts several representative ToF spectra for different kinetic energies of the electron pulses, set by the acceleration voltage, at a drift tube voltage of about −29 513 V. Note that this value is slightly smaller in magnitude than the −30 000 V used in the simulation (cf. section 6.1), since the voltage applied to accelerate the electrons needs to exceed the drift tube voltage, which in that case would be beyond the range of the high-voltage supply used for electron acceleration (up to −30 000 V). The exposure time is about 1 s per spectrum, during which single-shot ToF measurements are triggered at 5.128 MHz, being the repetition rate of the laser system (cf. sections 4.3 and 6.1). The ToF spectra are time histograms of all measured events within the exposure time. Additionally, single-shot data can be used for time-domain analysis, since it contains modulations of the measured ToF at Fourier frequencies up to the count rate. Thus, systematic ToF or energy broadening, e.g. due to electronic or mechanical noise at characteristic Fourier frequencies, can be revealed and separated from purely statistical broadening which is "white" in the frequency domain.

The energy bandwidth of the electron pulses is 0.2 eV–0.3 eV (cf. section 5.3) throughout all measurements; hence, the different shapes of the ToF spectra are related to different amounts of temporal dispersion and geometry-related broadening at different central kinetic energies. The asymmetric broadening towards larger ToF values, which is more evident at higher central kinetic energies, arises from the beam's finite diameter and divergence, since all off-axis trajectories result in larger ToF values compared to the position of the peak (cf. section 6.1).

In order to convert an arbitrary ToF spectrum into an energy spectrum, a calibration of the spectrometer needs to be performed (cf. section 5.1). To this end, the kinetic energy of the electrons is scanned by changing the acceleration voltage over the range of interest (here about 50 V), starting at the value of the drift tube voltage, in steps of about 1 V. The ToF value at the peak of the ToF spectrum as a function of the kinetic energy then yields a calibration curve which can be used to convert an arbitrary ToF spectrum into energy. The relation between ToF after passing the drift tube, $t(E)$, and kinetic energy, E, follows from the classical equation of motion (cf. eqn 2.4):

$$t(E) = d\sqrt{\frac{m_\mathrm{e}}{2(E - E_\mathrm{th})}} + t_\mathrm{offset}, \tag{6.2}$$

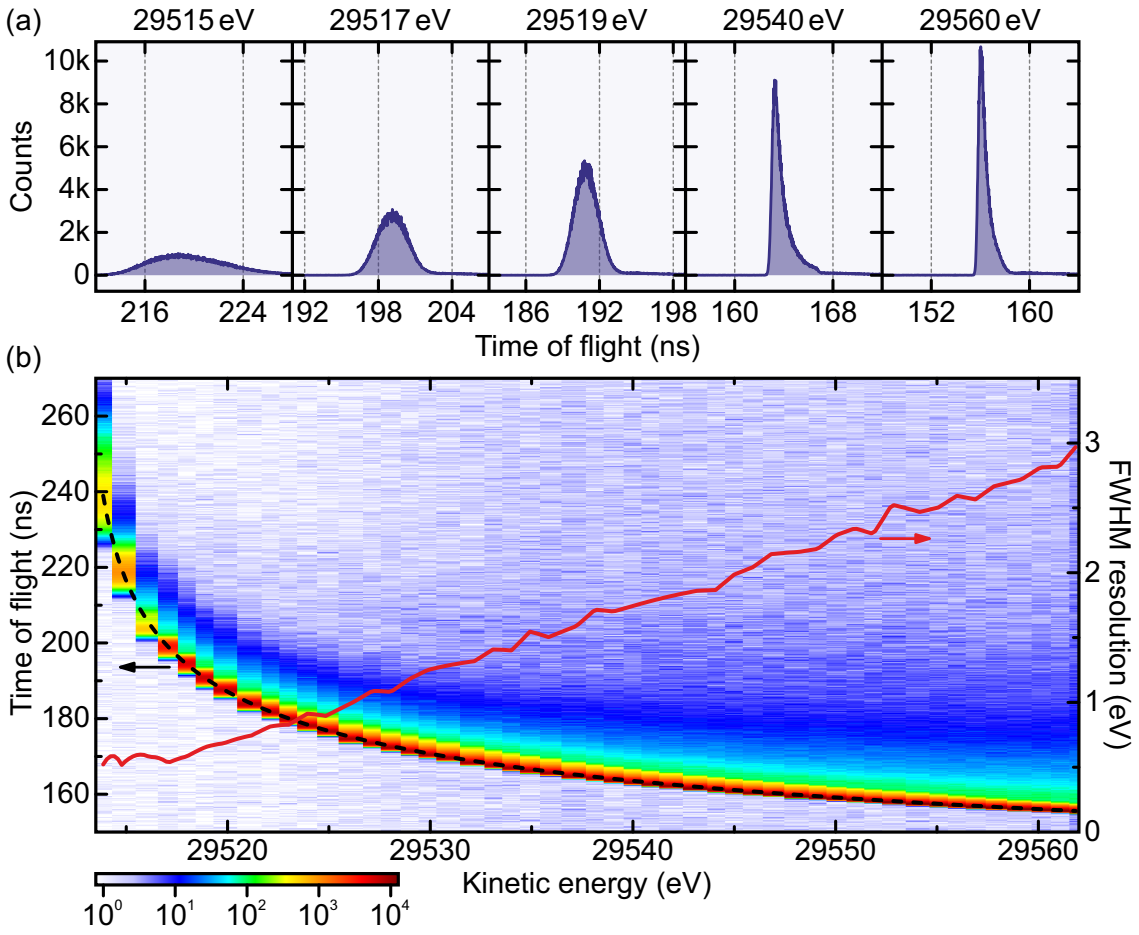

Figure 6.3: Results of the calibration scan for a drift tube voltage of about −29 513 V, corresponding to $E_{th} \approx 29\,513$ eV. (a) Representative ToF spectra for different kinetic energies of the electrons, showing an energy-dependent width due to different amounts of temporal dispersion and geometry-related broadening. Asymmetric broadening due to the beam's finite diameter and divergence is evident, since all off-axis trajectories result in larger ToF values compared to the position of the peak. (b) ToF spectra of the calibration scan are color-coded on a logarithmic scale, exhibiting a pronounced asymmetric background around the peak at larger ToF values due to geometry-related broadening. The dashed black line shows a fit of the energy-dependent position of the peaks of the ToF spectra, t(E), according to eqn 6.3. The FWHM energy resolution (red) is determined from the width of the ToF spectra (FWHM) and t(E), according to eqn 6.4, yielding <0.6 eV over a range of up to 5 eV above E_{th}.

d being the drift tube's length, m_e the electron's mass, E_{th} the threshold energy below which electrons are rejected and do not pass the drift tube, and t_{offset} a time offset accounting for the ToF outside the drift tube as well as delays of the signals inside the cables and the TDC. t_{offset} does not depend on the kinetic energy within the temporal resolution of the detector. This simple relation is only valid for a uniform motion and does not take into account the acceleration within regions of

inhomogeneous electric potential at the openings of the drift tube. Therefore, eqn 6.2 poorly reproduces the measured $t(E)$ curve as well as the simulated traces depicted in fig. 6.2 (b). An empirical relation is found to reproduce the actual energy dependence of the ToF very well, based on a generalization of eqn 6.2:

$$t(E) = \frac{A}{(E - E_{\mathrm{th}})^B} + t_{\mathrm{offset}}, \tag{6.3}$$

A and $0 < B < 1$ being fitting parameters. B is found to be $\sim$0.3 in order to reproduce the data, while it is 0.5 in eqn 6.2. All parameters, A, B, E_{th}, and t_{offset}, can be retrieved from a calibration scan by fitting eqn 6.3 to the data. This is shown as the dashed black line in fig. 6.3 (b), which is in excellent agreement with the numerically determined positions of the peaks of the measured ToF spectra. A calibration curve which is parametrized in that way can then be used to convert the ToF axis of an arbitrary spectrum into energy. In addition, the count values need to be weighted by $\mathrm{d}t(E)/\,\mathrm{d}E$ in order to conserve the total number of counts when integrating a part of the ToF spectrum and the corresponding part of the converted energy spectrum. This accounts for the nonlinear relation between the equidistantly sampled time bins (ToF spectrum) and non-equidistant energy bins (energy spectrum). The transmission through the drift tube is energy-dependent and varies by up to 50 % over a few-eV range above E_{th}, which can be compensated when converting an arbitrary ToF spectrum into energy, since the transmission curve is also acquired during the calibration scan. More than 80 % of the electrons are transmitted at kinetic energies of 5 eV above E_{th} and higher.

The raw ToF spectra of the calibration scan, some of which are also depicted in fig. 6.3 (a), are shown in fig. 6.3 (b), the counts being color-coded on a logarithmic scale. Asymmetric geometry-related broadening around the peak is evident as a broad background at larger ToF values, corresponding to smaller energies when converting the ToF spectrum into energy. Finally, the FWHM energy resolution, $R_{\mathrm{FWHM}}(E)$, can be determined from the derivative of the $t(E)$ curve with respect to energy and the energy-dependent ToF width of the measured spectra (FWHM), $\tau_{\mathrm{FWHM}}(E)$, in analogy to the resolution defined in eqn 6.1:

$$R_{\mathrm{FWHM}}(E) = \tau_{\mathrm{FWHM}}(E) \left| \frac{\mathrm{d}t(E)}{\mathrm{d}E} \right|^{-1} \tag{6.4}$$

Since the ToF spectra are asymmetric and non-Gaussian, their FWHM is determined numerically as the ToF width at half maximum. The resulting energy-dependent FWHM energy resolution is shown in fig. 6.3 (b) in red, yielding <0.6 eV over a range of up to 5 eV above E_{th} and <3 eV over a range of up to 50 eV above E_{th}. The

measured minimum energy resolution of ∼0.55 eV is limited by the bandwidth of the electron pulses, which is on the same order. Thus, the actual energy resolution is likely better and in good agreement with the intended specifications based on the simulations (cf. section 6.1).

6.3 Application: Laser-microwave phase detector

As a first application, the ToF spectrometer is employed as a laser-microwave phase detector, replacing the Wien filter analyzer presented in chapter 5 (cf. fig. 5.1). The superior energy resolution of the ToF spectrometer substantially improves the measurement precision of temporal spreads and drift by means of microwave streaking. Also, an improved electron gun is used [87], providing an acceleration field of 8.3 kV/mm at an acceleration voltage of −25 kV. The microwave cavity is driven at a frequency of 6.237 GHz and a power of ∼2 W by the direct microwave extraction source (cf. section 5.2). A calibrated phase shifter is used to set the microwave's phase inside the cavity to the compressing zero crossing of the energy modulation curve (cf. section 5.3). The rate of energy gain at this phase is $g_E = (69 \pm 2)\,\mathrm{eV/ps}$[1], which is determined by scanning the microwave's phase over a short range around the zero crossing, while recording the central kinetic energy with the ToF spectrometer. The drift tube's threshold energy, E_{th}, is set about 30 eV below the central kinetic energy of the electrons in order to accommodate for the large energy spread imprinted by the microwave field. After 5 s of acquisition time, the energy broadening induced by the microwave field is $\Delta E = (25 \pm 1)\,\mathrm{eV}$ FWHM compared to the intrinsic energy spread with the microwave cavity being switched off. This yields a temporal spread of $\tau_{\mathrm{e}} = \Delta E / g_E = (360 \pm 20)\,\mathrm{fs}$ FWHM, constituting an upper limit for both the dispersed electron pulse's duration at the microwave cavity and the laser-microwave jitter, since τ_{e} is a convolution between both values (cf. section 5.3). Here, τ_{e} is significantly smaller than in section 5.3 (cf. table 5.1), despite a nearly identical microwave source being used in both cases; thus, the reduced τ_{e} is owed predominantly to the higher acceleration field and an accordingly shorter duration of the dispersed electron pulses at the microwave cavity.

Fig. 6.4 depicts a measurement of the long-term drift of the central kinetic energy, i.e. the peak of the energy spectrum, as well as the corresponding timing drift, reflecting the drift of the microwave's phase inside the cavity. Each data point represents an energy spectrum which is averaged over an exposure time of 5 s. The relation between energy drift and timing drift is linear for small values and given by

[1] This value is higher than in the previous microwave streaking experiment with the direct extraction source (cf. table 5.1) because a prototype of this microwave source has been used in the experiments described in section 5.3, not yet providing the full power of ∼2 W.

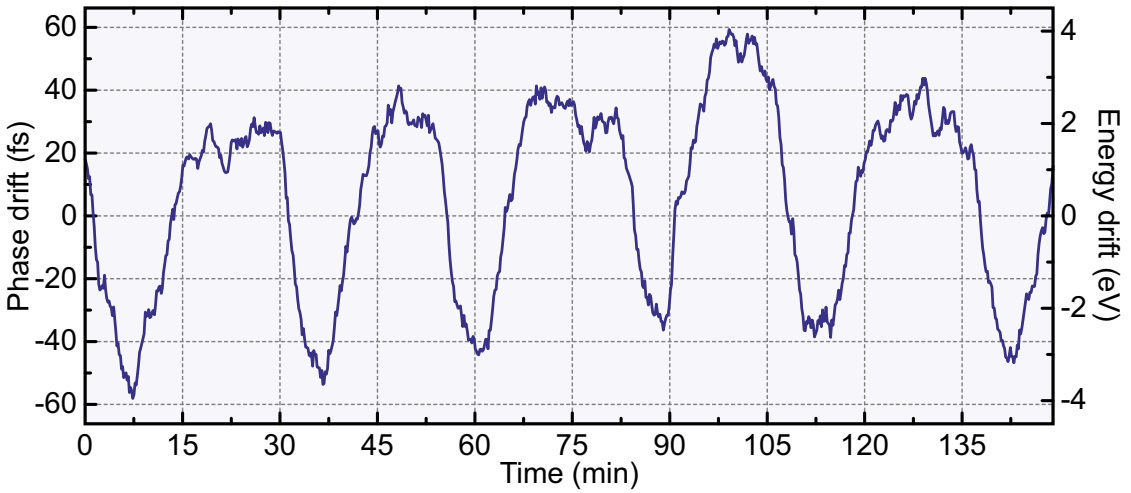

Figure 6.4: Long-term drift of the microwave's phase inside the microwave cavity, measured with the ToF spectrometer which is operated as a laser-microwave phase detector, in terms of timing drift as well as drift of the central energy. A timing drift on the order of 100 fs peak-to-peak is evident with a half-hour period, reflecting the periodic drift of the temperature in the laboratory despite stabilization. However, a timing stability of below 3 fs rms is achieved over short periods of up to 15 min. The precision of the measurement is about 1 fs rms for an integration time of 5 s.

g_E. A half-hour period of the timing drift is evident with a peak-to-peak amplitude of about 100 fs, reflecting periodic drift of the temperature in the laboratory. The period corresponds to the cooling cycle of the liquid used for air conditioning in the building. Since the temperature of the microwave cavity is stabilized separately, the timing drift is attributed mainly to drift of the laser's repetition rate (cf. section 4.3) and the separation between the mirrors of the optical mode filter (cf. section 4.5). Both contributions cause a timing drift due to the mode filter's and the microwave cavity's frequency-dependent phase.

This slow timing drift poses a limitation of the temporal resolution of UED employing electron pulse compression with microwave fields. Thus, a slow active phase stabilization is required in order to facilitate extended acquisition times (cf. section 4.5). However, a timing stability of below 3 fs rms over periods of up to 15 min is evident, enabling measurements of short acquisition times with high timing precision, e.g. electron pulse characterization in the time domain (see section 7.2). Note that the laser-microwave phase detector employing the ToF spectrometer presented in this chapter is capable of measuring the timing drift with a remarkable precision of about 1 fs rms, which is an upper limit based on the fluctuations of the data in fig. 6.4, for an integration time of 5 s. This corresponds to a precision of about 40 µrad rms in terms of microwave phase.

Chapter 7

Ten-femtosecond (rms) electron diffraction

Advancing the temporal resolution of UED by electron pulse compression requires an accurate and reliable characterization technique in the time domain, suitable for compressed and uncompressed electron pulses. Streaking by the microwave field used for compression [81], as presented in chapter 5, can be employed with little additional effort to characterize the dispersed electron pulses at the microwave cavity, i.e. before compression, thus providing some insight about the initial dispersion. However, this streak camera lacks the capability to elucidate the electron pulse compression after the microwave cavity and its temporal resolution is limited by the laser-microwave jitter. Only a direct temporal characterization of the compressed electron pulses at the temporal focus with respect to the laser pulses reveals the actual quality of the microwave compression, which determines the temporal resolution of UED pump-probe experiments.

An additional microwave cavity can be used as a streak camera for electron pulses at the temporal focus [70, 124]. However, the temporal resolution is limited to about 100 fs FWHM by the available microwave power; furthermore, laser-microwave jitter is neglected in this approach if the additional streaking cavity is driven by the same microwave source as the compression cavity. Thus, in order to determine the temporal resolution of UED pump-probe experiments, the jitter needs to be separately taken into account.

Ponderomotive scattering [96, 171] provides a free-space cross-correlation between an electron pulse and a laser pulse. The temporal resolution is limited by the spatial extent of the interaction region which the electron pulse has to traverse, given roughly by the focal cross-section of the electron beam and the laser pulse's duration. A temporal resolution of about 80 fs FWHM is reported in [96]. Typically, a laser pulse energy of several hundred µJ is required under optimized conditions for a significant ponderomotive interaction between the electron pulse and the laser

pulse, since the ponderomotive force scales with the gradient of the optical intensity. Hence, this method is restricted to amplified laser systems at kHz repetition rates and is not suitable for the 5 MHz laser oscillator used in this work, since the available pulse energy of this laser source is about 500 nJ (cf. section 4.3).

In this work, we employ a recently developed technique of optical field streaking of the electron pulses, providing a direct laser-electron cross-correlation for ultrafast characterization [93]. Here, the electric field of a laser pulse modulates the electron's kinetic energy; thus, the temporal resolution, given by the optical field transients, can ultimately reach down to tens of attoseconds [20, 33], provided that the shape of the optical field is well controlled. The pulse energy of a typical femtosecond Ti:sapphire oscillator is sufficient to modulate the kinetic energy of sub-relativistic electron pulses by an amount which is easily detectable, e.g. by the high-resolution ToF spectrometer presented in chapter 6. Besides a temporal laser-electron cross-correlation, streaking measurements also provide a correlation between time and energy, thus offering a powerful tool for visualization of the electron pulse's phase space and its transformation when microwave compression is applied.

In this chapter, the compression of single-electron pulses with microwave fields is studied by optical field streaking, employing the ToF spectrometer presented in chapter 6. A record-short electron pulse duration of (28 ± 5) fs FWHM or (12 ± 2) fs rms is demonstrated with respect to the arrival time of the streaking laser pulses, reflecting the achievable temporal resolution of possible UED pump-probe experiments. Furthermore, linear transformations of the electron pulse's phase space by the interaction with the microwave field and the dispersion in vacuum, as predicted in section 3.1, are verified. Characterization by optical field streaking also allows investigating the influence of space charge on the compressibility of the electron pulses and the achievable pulse duration when using few- and multi-electron pulses. Finally, the potential applicability of the compressed electron pulses for UED and ultrafast EELS is demonstrated by recording static diffraction patterns from an organic molecular crystalline sample as well as EELS spectra from aluminum.

7.1 Optical field streaking of sub-relativistic free electron pulses

Optical field streaking is based on a rapid transition of the electrons into or out of a controlled optical field within a transition time well below the duration of an optical cycle. In contrast, a free-space interaction between an optical pulse and an electron pulse leaves the electron's kinetic energy nearly unchanged, apart from a ponderomotive scattering effect [171]. For any intersection geometry between the two pulses,

the alternating acceleration of the electron inside the optical field cancels out after the interaction, since the time integral of the electric field of an optical pulse over the entire pulse is zero for any projection of the Gaussian optical beam onto the electron's trajectory. In optical streaking experiments employing attosecond XUV pulses, electrons are generated via photoemission by the XUV pulses from gas [20, 27] or solid state [19] targets in the presence of an optical streaking field. Thus, the electrons are released or "born" into the optical streaking field within the duration of the attosecond XUV pulse. Here, the net momentum transfer to the electrons is defined by the time integral of the streaking field over the remaining part of the streaking pulse. Depending on the phase of the streaking field at the instant at which the electrons are released by the XUV pulse, a non-zero momentum gain or loss is permitted after the streaking pulse has passed. As a consequence, the momentum modulation (and also the energy modulation for small changes around the central kinetic energy) as a function of the delay time between the XUV pulse and the streaking pulse reflects the streaking pulse's vector potential. Thus, the streaking electric field as well as the duration and phase of the XUV pulse releasing the electrons can be reconstructed [26]. This constitutes a streak camera, similar to the microwave streak camera presented in chapter 5, yet employing optical field transients at frequencies in the 100 THz range with a corresponding temporal resolution.

Streaking of free electron pulses by optical fields relies on the same principle, yet at kinetic energies of the electrons suitable for UED, 25 keV in this work, as compared to the ∼100 eV range in attosecond XUV streaking experiments. Here, an almost instantaneous transition of the electrons from the streaking field into a field-free region is facilitated by a 50 nm thin free-standing aluminum foil[1], as depicted in fig. 7.1, constituting a mirror for the streaking laser pulses but partially transmitting electron pulses (about 3.5 % of transmission at 25 keV). The experimental arrangement represents a UED pump-probe experiment employing microwave pulse compression (cf. fig. 1.3 in section 1.4) with the diffraction sample being replaced by the streaking foil. A non-collinear intersection between the laser beam and the electron beam at the foil and a polarization of the laser parallel to the plane spanned by the two beams provides a component of the optical electric field along the electron beam's propagation direction upon reflection at the foil (orange arrow in fig. 7.1), which modulates the electron's kinetic energy. At a wavelength of 800 nm, the $1/e$ penetration depth of aluminum is about 7.6 nm [176]. Therefore, the transition time for electrons at a kinetic energy of 25 keV is about 84 as, which is a small fraction of an optical cycle at this wavelength (2.67 fs). The non-collinear arrangement and the

[1] The foil is manufactured by thermal evaporation of aluminum onto a soap-covered glass substrate. The soap is subsequently removed with water and the foil is transferred to a copper mesh for support with a grid line separation of 250 µm [93].

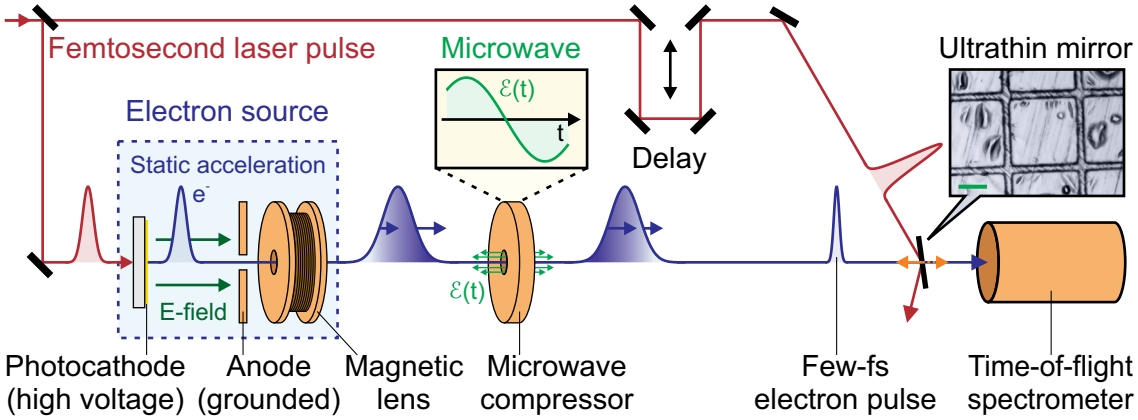

Figure 7.1: Concept of electron pulse characterization via optical field streaking. The experimental arrangement is essentially identical with a UED pump-probe experiment employing electron pulse compression with microwave fields (cf. fig. 1.3). However, instead of a diffraction sample, an ultrathin (50 nm) aluminum mirror is used as a streaking target. The free-standing aluminum foil on a copper grid is shown in the inset, the green scale bar denoting 100 µm. The laser pulse impinging on the foil is polarized parallel to the plane spanned by the laser and the electron beam, providing an optical field component along the electron beam's propagation direction upon reflection at the foil (orange arrow). The optical field is shielded by the foil within a fraction of the optical wavelength, while electrons are partially transmitted. Thus, electrons passing though the foil gain or lose energy from the interaction with the field, depending on the field's phase at that moment. A ToF spectrometer (cf. chapter 6) records the energy modulation as a function of the delay between the laser pulse and the electron pulse. This constitutes an optical streak camera with a resolution given by the optical oscillations.

finite diameter of the beams at the intersection necessitate group velocity matching between the respective wave fronts at the streaking foil by an appropriate choice of angles in order to ensure a constant delay over the entire interaction area at the foil. For electron pulses at 25 keV, the sweeping velocity of the wave front along the foil's surface is matched to the laser pulses at an angle of incidence of 17° and 77° to the surface normal for the electron beam and the laser beam, respectively [87]. The energy modulation by the optical streaking field is recorded via a high-resolution ToF spectrometer (cf. chapter 6) as a function of the delay time between the optical streaking pulse and the electron pulse. This yields streaking spectrograms which visualize the time-dependent energy modulation, providing a cross-correlation between the electron pulse and the optical streaking pulse.

A non-relativistic analysis of the acceleration of the electrons inside the optical streaking field yields an energy modulation which is proportional to the oscillating streaking field but phase-shifted by 90° [13]. This represents the vector potential. Higher-order terms can be neglected for the streaking field strengths used in this work. Assuming a field of the optical streaking pulse at the foil of the form

$\mathcal{E}(t) = \mathcal{E}_\mathrm{A}(t)\cos(\omega t)$, $\mathcal{E}_\mathrm{A}(t)$ being the temporal envelope of the electric field (i.e. its amplitude) and ω its angular frequency, the energy modulation due to a longitudinal interaction of the electrons with the streaking field is given by [87, 93]:

$$\Delta E = \frac{e\mathcal{E}_\mathrm{A}(t)}{\omega}\sqrt{\frac{2E_0}{m_\mathrm{e}}}\sin(\omega t), \tag{7.1}$$

e and m_e being the electron's charge and mass, respectively, and E_0 its central kinetic energy. A constant phase offset is neglected here. The carrier-envelope phase of the laser pulses used in this work (cf. section 4.3) is not stabilized and hence random for every laser shot. Therefore, the energy modulation in eqn 7.1 results in a cycle-averaged energy spectrum after a certain integration time, the maximum energy gain (or loss) at each delay time t reflecting the field envelope $\mathcal{E}_\mathrm{A}(t)$. Thus, the cycle-averaged maximum energy gain at $t = 0$ is simply given by:

$$\Delta E_\mathrm{max} = \frac{e\mathcal{E}_\mathrm{A,max}}{\omega}\sqrt{\frac{2E_0}{m_\mathrm{e}}}, \tag{7.2}$$

$\mathcal{E}_\mathrm{A,max} = \mathcal{E}_\mathrm{A}(t = 0)$ being the peak electric field at the streaking foil. Note that $\mathcal{E}_\mathrm{A}$ and $\mathcal{E}_\mathrm{A,max}$ refer to effective optical field amplitudes at the foil along the electron pulse's trajectory, taking into account the superimposed field of the reflected beam as well as the Lorentz force on the electrons [87]. For the experimental geometry used in this work, the effective field at the foil is enhanced by about 50 % as compared to the optical field in free space at the same intensity. The laser beam's diameter at the foil is 44 µm × 68 µm FWHM, projected onto the electron beam's axis, and the maximum pulse energy used for streaking is about 370 nJ, yielding $\mathcal{E}_\mathrm{A,max} \approx 1.83\,\mathrm{GV/m}$ [87] and a maximum – or cutoff – energy gain of about $\Delta E_\mathrm{max} \approx 73\,\mathrm{eV}$ at $E_0 = 25\,\mathrm{keV}$ according to eqn 7.2. In order to avoid thermal damage of the streaking foil, the repetition rate of the laser system is reduced to the 100 kHz range via a pulse picker [87]. The electron beam (same source as in section 6.3) is coarsely focused by a solenoid magnetic lens to a diameter of 288 µm × 323 µm FWHM.

Fig. 7.2 (a) shows a streaking spectrogram employing dispersed electron pulses with the microwave cavity switched off. Negative delay times indicate an early arrival of the electron pulses at the streaking foil with respect to the laser pulses, which is a common definition for pump-probe traces with the electron pulses being considered as probe. Here, about three electrons per pulse are used for enhanced statistics. The "unstreaked" energy spectrum at large negative delay times is subtracted from each spectrum constituting the spectrogram in order to enhance changes. Note that both increase and decrease of electron counts are depicted on a logarithmic scale using different color ranges. Hence, electron counts are visibly redistributed during the

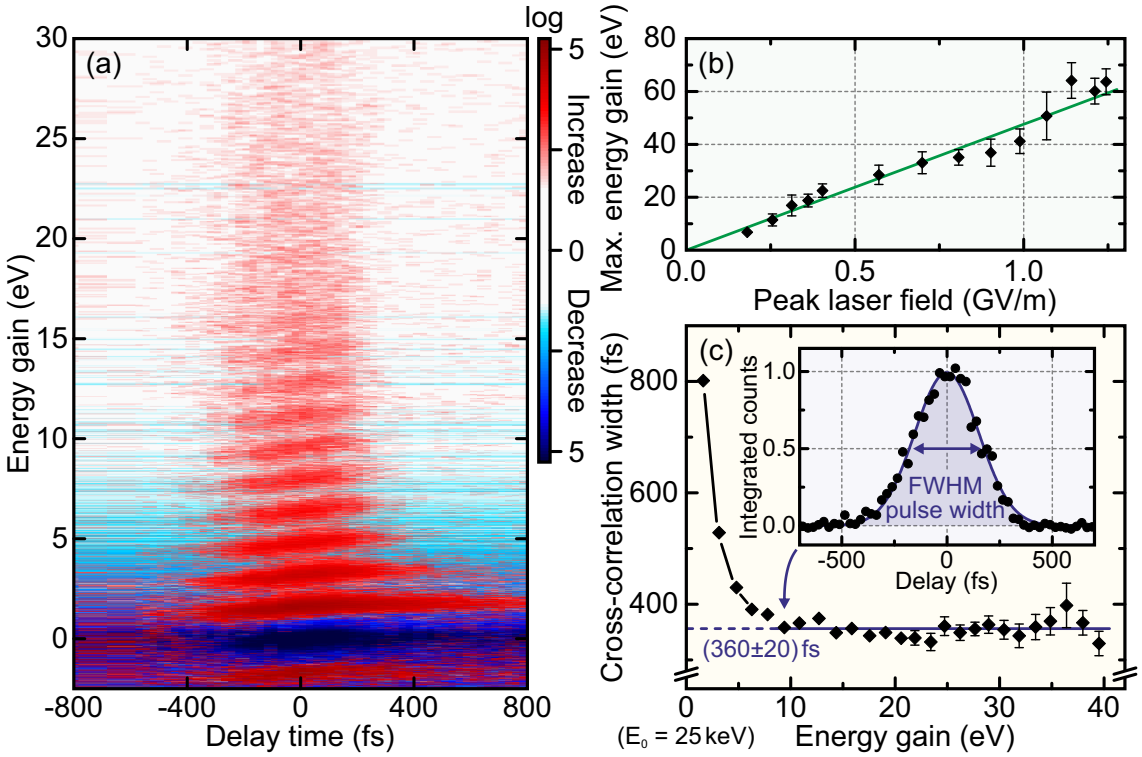

Figure 7.2: Optical streaking of dispersed electron pulses without microwave compression; data taken from [93]. (a) Streaking spectrogram showing the energy gain region around the central kinetic energy of $E_0 = 25\,\text{keV}$. Negative delay times indicate an early arrival of the electron pulses at the streaking foil with respect to the laser pulses. The "unstreaked" electron spectrum at large negative delays is subtracted in order to enhance changes. Increase and decrease of electron counts are both shown on a logarithmic scale using different color ranges. A spectral interference with a modulation period of $\sim$1.6 eV, corresponding to the streaking pulse's photon energy, indicates a longitudinal coherence time of the electron wave packet on the order of one optical cycle (2.67 fs) or longer. The interference orders as well as the decrease feature at zero energy gain are slanted, denoting an earlier arrival of higher-energetic electrons. This visualizes the electron pulse's chirp due to dispersion in vacuum. The temporal width of the spectrogram constitutes a cross-correlation between the electron pulse and the field envelope, $\mathcal{E}_A(t)$, of the streaking laser pulse. (b) Maximum measured energy gain reveals a linear dependence on the peak optical streaking field, $\mathcal{E}_{A,max}$, confirming the applicability of eqn 7.2 to sub-relativistic free electron pulses. (c) FWHM duration of the cross-correlation, extracted from the streaking spectrogram, as a function of the energy gain. The energy gain is proportional to the streaking field envelope; thus, the temporally broad pedestal of the streaking laser pulse (cf. fig. 4.3 (b)), despite carrying little optical intensity, is sufficient to induce a small energy gain. The electron pulse's duration dominates at higher values of the energy gain, since only the center of the laser pulse (50 fs FWHM duration of the intensity envelope) exhibits sufficient field strength to induce this energy gain. Thus, the width of the cross-correlation converges to the electron pulse's duration of (360 ± 20) fs FWHM (blue line) above $\sim$10 eV of energy gain. The inset shows a temporal line profile of the spectrogram integrated around the 6$^{\text{th}}$ interference order at about 9 eV of energy gain and a Gaussian fit (blue line).

temporal overlap between the electron pulse and the streaking laser pulse from their central kinetic energy ($E_0 = 25\,\mathrm{keV}$) to higher and lower energies. The threshold energy of the ToF spectrometer is set to few eV below the central kinetic energy of the electrons, such that the range of highest resolution covers the energy gain region, since the noise background is substantially lower for energies above the central kinetic energy than for lower energies (cf. section 6.2).

Since the carrier-envelope phase of the laser pulses is not fixed and the electron pulse's duration is much longer than an optical cycle, the streaking spectra are cycle-averaged, reflecting the streaking field's envelope rather than the field oscillations. A pronounced spectral interference is visible, spaced by a modulation period of $\sim$1.6 eV which corresponds well to the photon energy of the streaking pulse (1.55 eV). A single-electron wave packet which coherently extends over more than one optical cycle can interfere with itself if different parts of the wave packet leave the streaking field at subsequent optical cycles, while gaining or losing the same amount of energy [13, 93, 177]. This semi-classical description requires a quantum mechanical treatment of the electrons, while applying a classical optical field. The visibility of the interference fringes indicates a longitudinal coherence time of the electrons on the order of an optical cycle (2.67 fs) or longer, which is in good agreement with the longitudinal coherence estimated from the uncertainty relation (cf. section 2.1). However, a detailed quantitative analysis is limited by the spectrometer's energy resolution. Note that the visibility of the fringes decreases at higher interference orders due to the spectrometer's energy-dependent resolution which continuously deteriorates at higher energies above the threshold energy (cf. fig. 6.3 (b)). Similar sidebands have been observed in ultrafast electron microscopy of evanescent optical near-fields at nanostructures [174]. In contrast to optical streaking, this effect has been explained by multi-photon absorption of the electrons as a consequence of inelastic scattering, mediated by the near-field in the vicinity of a nanostructure [175].

The measured energy gain extends to $\sim$65 eV (not shown in the spectrogram), which is in agreement with the expected cutoff energy of 73 eV, according to eqn 7.2, and likely underestimated due to the small signal-to-noise ratio at high energy gain values. Fig. 7.2 (b) shows the measured maximum energy gain as a function of the peak effective electric field of the streaking pulse, $\mathcal{E}_{\mathrm{A,max}}$, at the foil. The linear dependence (green line) verifies optical field streaking (cf. eqn 7.2) rather than a nonlinear multi-photon effect as the mechanism responsible for the modulation of the electron's kinetic energy. Note that the linear field dependence of the streaking effect facilitates employing low-power laser oscillators at high repetition rates for streaking. At a pulse duration of 50 fs FWHM, a pulse energy of 10 nJ (typical for a Ti:sapphire oscillator in the 100 MHz range) is sufficient to induce a maximum energy gain of about 12 eV, which is well within the spectrometer's energy resolution.

According to eqn 7.1, the cycle-averaged temporal profile of the maximum energy gain follows the electric field envelope of the streaking field, $\mathcal{E}_A(t)$, if assuming a negligibly short electron pulse. However, for a significant duration of the electron pulse, the temporal profile is broadened by the electron pulse's duration. Hence, the temporal width of the spectrogram at a particular energy gain value constitutes a cross-correlation between the electron pulse's temporal profile and the portion of the streaking laser pulse's field envelope which is capable of imprinting this energy gain onto the electrons. The FWHM cross-correlation width is shown in fig. 7.2 (c) as a function of the energy gain. The width is evaluated by integrating the spectrogram over a range of ∼1.6 eV along the energy dimension around each interference order and fitting a Gaussian to the temporal line profile, as shown in the inset [87]. Since the interference orders become indistinguishable at higher energy gain values, equidistant slices of the same energy range are integrated there in order to obtain temporal line profiles.

The large temporal width at small energy gain values, i.e. for the lowest interference orders, results from the temporally broad pedestal of the streaking laser pulse (cf. figs. 4.3 (b) and 7.5 (a)). Despite the little optical power being carried within the pedestal (few percent), the corresponding electric field is sufficient to modulate the electron's kinetic energy by several eV. Higher energy gain requires a higher optical field strength, which is only provided by a temporally shorter portion of the streaking laser pulse around its peak. The highest energy gain corresponds to the peak electric field, i.e. an infinitely short moment in time. Practically, the temporal confinement at the maximum energy gain is dictated by the size of the delay time steps, the energy resolution, and the noise floor. The temporal broadening by the electron pulse's duration is equal for each energy gain value. Effectively, the width of the cross-correlation at each energy gain value is a convolution between the temporal profile of the electron pulse and an energy-gain-dependent sampling function which is given by the envelope of the streaking laser pulse's electric field. Thus, the cross-correlation width converges to the electron pulse's duration above a certain energy gain where the temporal width of the contributing streaking field envelope becomes significantly shorter than the electron pulse's duration. The laser pulse's duration is about 50 fs FWHM for the intensity envelope (cf. section 4.3), which is substantially shorter than the expected duration of the dispersed electron pulse (cf. section 5.3). Thus, the measured cross-correlation width converges to (360 ± 20) fs FWHM already at energy gain values above ∼10 eV (blue line in fig. 7.2 (c)), yielding directly the dispersed electron pulse's duration at the streaking foil. Remarkably, this value is in excellent agreement with the temporal spread measured by microwave streaking (cf. section 6.3), indicating a significantly smaller upper limit for the laser-microwave jitter (<170 fs FWHM within the error margins; cf. eqn 5.5).

The interference orders in fig. 7.2 (a) in both the energy gain and loss regions as well as the decrease feature at zero energy gain are slightly slanted, indicating higher kinetic energies of earlier arriving (i.e. faster) electrons due to dispersion in vacuum (cf. sections 2.2 and 3.1). This demonstrates the capability of the optical streaking technique of simultaneous temporal and spectral characterization, allowing a measurement of all phase space characteristics of the electron pulses, such as the temporal spread, the energy bandwidth, and the chirp.

7.2 Characterization of electron pulse compression in the time domain

Fig. 7.3 shows several representative streaking spectrograms, obtained by the optical streaking technique described in section 7.1, for different values of the microwave compression strength, g_E. The microwave source used to drive the compression cavity is based on optically enhanced direct microwave extraction from a photodiode (cf.

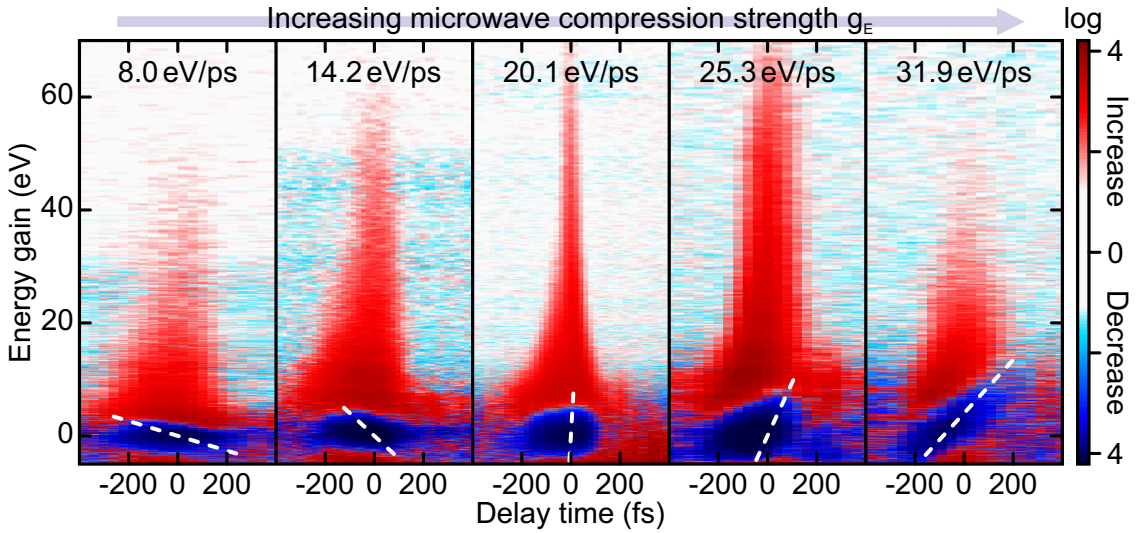

Figure 7.3: Visualization of electron pulse compression with microwave fields. Five representative streaking spectrograms are shown for increasing values of the microwave compression strength, g_E (left to right). The spectrograms are processed and presented in the same way as in fig. 7.2 (a). A minimum temporal width of the cross-correlation is evident for $g_E = 20.1\,\mathrm{eV/ps}$ at high energy gain values where the temporal width of the streaking laser pulse contributing to the cross-correlation is small (cf. section 7.1). Here, the temporal focus is at the streaking foil, while at higher or smaller values of g_E the temporal focus is before or behind the streaking foil, respectively. The linear chirp of the electron pulse is shown for each spectrogram as a white dashed line at the decrease feature, denoting the temporal distribution of different kinetic energies. The chirp changes its sign around the g_E value of optimum compression.

sections 5.2, 5.3, and 6.3). The microwave's phase is set via a phase shifter to the compressing[2] zero crossing of the energy modulation curve (cf. section 5.3) such that the central kinetic energy of the electron pulses is unchanged after passing the cavity. A variable attenuator is used to set the microwave's amplitude inside the cavity and thus the compression strength g_E. The microwave's phase is scanned over a short range around the zero crossing of the energy modulation curve in order to calibrate g_E for a particular microwave power fed into the cavity. All other values of g_E are calculated via this calibration and the measured microwave power, P, after the attenuator, according to $P \propto g_E^2$. Since the distance between the cavity and the streaking foil is fixed at $(24.0 \pm 0.5)\,\mathrm{cm}$, the temporal focus needs to be adjusted via the microwave compression strength to coincide with the streaking foil.

The phase space transformations involved in the compression of single-electron pulses are visualized in fig. 7.3 in an instructive way, being consistent with the illustration in fig. 2.2 (b): At small values of g_E, the chirp of the electron pulse (white dashed lines) is reversed, as compared to the uncompressed pulse (cf. fig. 7.2 (a)), i.e. electrons of higher kinetic energy arrive later at the streaking foil, in contrast to normal dispersion in vacuum. However, the temporal focus is behind the streaking foil due to insufficient compression strength. At $g_E = 20.1\,\mathrm{eV/ps}$, corresponding to an input microwave power of $P \approx 100\,\mathrm{mW}$, the temporal focus coincides with the position of the streaking foil, yielding the shortest duration of the cross-correlation. The chirp is nearly zero, as no apparent correlation between kinetic energy and delay time is evident. At higher values of g_E, the electron pulses become over-compressed, i.e. the temporal focus is before the streaking foil, leading to a longer duration of the cross-correlation at the foil. Here, the chirp is reversed again, as compared to smaller values of g_E, due to vacuum dispersion, which manifests itself in an earlier arrival time of higher-energetic electrons, as in the case of uncompressed pulses (cf. fig. 7.2 (a)). The duration of the cross-correlation is a convolution between the electron pulse's duration and the field envelope of the streaking laser pulse, as pointed out in section 7.1. Therefore, a reduced width of the cross-correlation due to electron pulse compression is only evident at energy gain values at which the compressed electron pulse's duration dominates the width of the cross-correlation (cf. fig. 7.2 (c)). For the shortest electron pulse, the cross-correlation essentially reproduces the field envelope of the streaking laser pulse (see section 7.3). Note that no spectral interference is visible, in contrast to the uncompressed electron pulses (cf. fig. 7.2 (a)). This is a result of the pulse's temporal compression, which also compresses the longitudinal coherence of the single-electron's wave function and thus reduces the visibility of

[2] Besides recording the energy modulation curve (cf. section 5.3), the compressing and anti-compressing zero crossings can also be distinguished by the associated transverse defocusing and focusing effect, respectively [77].

interference orders, even for small values of the compression strength. In addition, incoherent spectral broadening occurs due to residual laser-microwave jitter.

The velocity spread, Δv, required to compress a dispersed electron pulse of a duration τ_{disp} at a certain temporal focus can be expressed in terms of the corresponding energy spread, ΔE, imprinted by the microwave. The distance from the microwave cavity to the temporal focus, f, as introduced in section 2.2 (cf. eqn 2.7), is thus given by:

$$f = v_0 \frac{\Delta z}{\Delta v} = v_0^2 \frac{\tau_{\mathrm{disp}}}{\Delta v} \approx \frac{\tau_{\mathrm{disp}}}{D_{\mathrm{vac}} \Delta E} \tag{7.3}$$

Here, Δz denotes the spatial extent of the electron pulse, as defined in eqn 2.7, v_0 is the electron pulse's central velocity, and D_{vac} the energy-dependent group velocity dispersion of vacuum for electrons, defined as:

$$D_{\mathrm{vac}} = \frac{1}{v_0^2} \left. \frac{\mathrm{d}v(E)}{\mathrm{d}E} \right|_{E_0} \approx \frac{\Delta v}{v_0^2 \Delta E}, \tag{7.4}$$

$E_0 = m_{\mathrm{e}} v_0^2/2$ being the electron pulse's central kinetic energy and $v(E) = \sqrt{2E/m_{\mathrm{e}}}$ the electron's non-relativistic velocity, i.e. the inverse of the dispersion defined in eqn 2.4. At 25 keV of central kinetic energy, $D_{\mathrm{vac}} \approx 206\,\mathrm{fs/(eV\,m)}$, meaning that after 1 m of propagation an electron pulse of 1 eV of bandwidth is broadened or compressed by 206 fs, depending on the sign of the pulse's initial chirp. In eqns 7.3 and 7.4 the identity

$$\Delta v \approx \Delta E \left. \frac{\mathrm{d}v(E)}{\mathrm{d}E} \right|_{E_0} \tag{7.5}$$

is used for small relative velocity and energy spreads ($\Delta v \ll v_0$, $\Delta E \ll E_0$), respectively. Hence, eqns 7.3 and eqn 7.4 are only valid for small relative energy spreads, single-electron pulses, and sub-relativistic kinetic energies. This approximation is justified, since the highest microwave amplitudes used in this work imprint a relative energy spread on the order of 10^{-3} onto the electrons. As pointed out in section 5.3, the energy spread imprinted by the microwave onto the electrons is given by $\Delta E \approx \tau_{\mathrm{disp}} g_E$ (cf. eqns 5.4 and 7.8) if g_E stays approximately constant within τ_{disp}. Thus, using eqn 7.3, the distance to the temporal focus is simply given by:

$$f \approx \frac{1}{D_{\mathrm{vac}} g_E} \tag{7.6}$$

Note that eqn 7.6 neglects the chirp of the dispersed electron pulse at the entrance of the microwave cavity. However, the additional compression strength required to compensate for this dispersion caused by the initial energy spread (see eqn 7.9 below) is typically small for practical values of g_E which allow compression below the initial

duration (cf. section 3.1). Therefore, the electron pulse is considered "unchirped" with a duration of τ_{disp} at the entrance of the cavity. According to eqn 7.6, the compression strength required to set the temporal focus at the streaking foil at $f = (24.0 \pm 0.5)\,\mathrm{cm}$ is $g_E = (20.2 \pm 0.4)\,\mathrm{eV/ps}$, which is in good agreement with the measured value of 20.1 eV/ps for the shortest duration of the cross-correlation.

The cutoff energy gain for the peak effective electric field of the streaking pulse used here (1.9 GV/m, slightly higher than in section 7.1) is expected to be at about 77.4 eV, according to eqn 7.2, which is in good agreement with the maximum measured energy gain of $(80 \pm 4)\,\mathrm{eV}$ for the g_E value at optimum compression, considering the additional energy broadening by the microwave field (see fig. 7.4 (b)). Note that at other values of g_E the highest measurable energy gain is somewhat below the calculated cutoff value due to the broader temporal spread of the cross-correlation, which leads to a reduced signal-to-noise ratio.

Fig. 7.4 shows a quantitative evaluation of the temporal spread of the cross-correlation as well as the energy bandwidth and the linear chirp of the electron pulses for different values of the microwave compression strength, g_E, extracted from the streaking spectrograms. In order to minimize the contribution of the streaking pulse's field envelope to the duration of the cross-correlation, the spectrograms are integrated over a range of ∼15 eV below the highest measurable energy gain and the line profiles are fitted by a Gaussian (cf. fig. 7.4 (d) and the inset in fig. 7.2 (c)). The FWHM duration as a function of g_E is shown in fig. 7.4 (a) as black diamonds, the vertical error bars denoting the statistical error of the fit for the respective spectrogram and the horizontal error bars denoting the uncertainty of the calibration of g_E. Each duration marks an upper limit for the electron pulse's duration at the respective compression strength, limited by the residual contribution of the temporal width of the streaking pulse's field envelope to the duration of the cross-correlation.

The characteristic quantities of the electron pulse's phase space – duration, bandwidth, and chirp – are correlated during electron pulse compression, which is schematically demonstrated in fig. 3.1, and a simple analytic model is employed to describe this process, assuming linear phase space transformations by the microwave field and vacuum dispersion. For ideal compression, the electron pulse's duration, τ_{el}, decreases linearly with the propagation distance, starting from its dispersed duration at the entrance of the microwave cavity, τ_{disp}, to a limit, τ_{final}, which is given by the initial duration at the instant of photoemission, τ_{initial}, and the additional energy spread imprinted by the microwave (cf. eqn 3.2 in section 3.1). Since the distance to the temporal focus linearly depends on the compression strength, g_E (cf. eqn 7.6), the measured electron pulse's duration at the streaking foil is given by:

$$\tau_{\mathrm{el}} = \sqrt{\tau_{\mathrm{disp}}^2 \left(1 - f D_{\mathrm{vac}} g_E\right)^2 + \tau_{\mathrm{final}}^2} \tag{7.7}$$

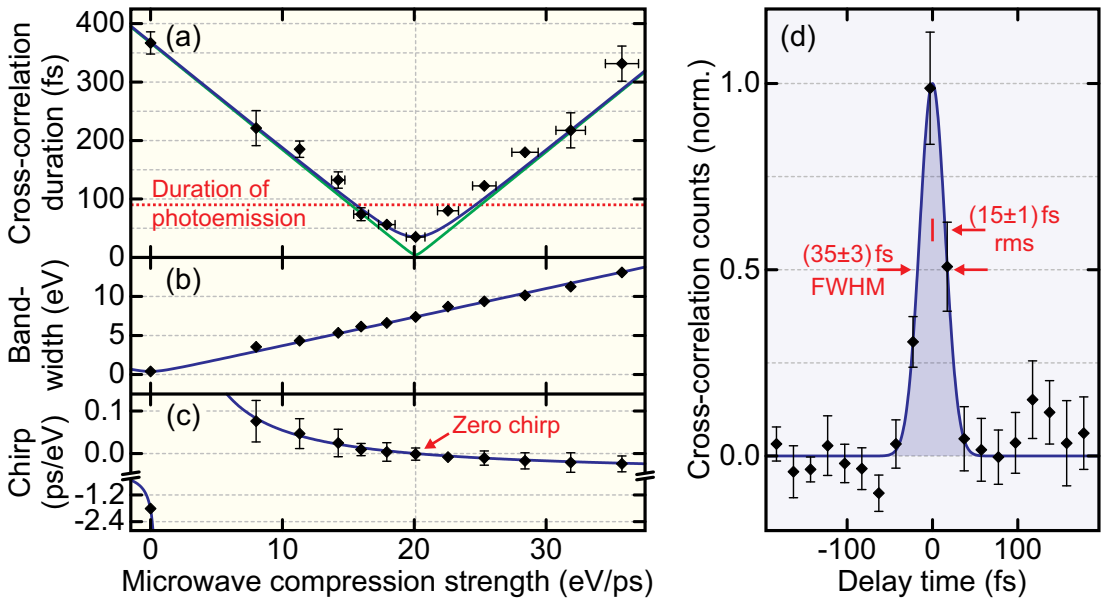

Figure 7.4: Quantitative analysis of electron pulse compression with microwave fields. The dashed gray vertical line in (a)–(c) denotes the compression strength yielding the shortest electron pulse, $g_E = 20.1\,\mathrm{eV/ps}$. (a) The shortest FWHM duration of the cross-correlation is determined by integrating each spectrogram over a range of ∼15 eV below the highest measurable energy gain and fitting a Gaussian to the line profile (see (d)). The solid lines are calculated according to eqn 7.7 for τ_{final} being limited by the shortest measured duration of the cross-correlation (blue) and for ideal phase-space-limited compression (green). Note that the duration of the cross-correlation falls significantly below the initial duration of photoemission (red dotted line) around the optimum compression strength. (b) FWHM bandwidth of the electron pulses after the microwave cavity, measured directly with the ToF spectrometer without the streaking laser pulse. A linear dependence on the microwave compression strength is evident, according to eqn 7.8 (blue line). (c) Linear chirp of the electron pulses, evaluated from the decrease feature of the spectrograms around zero energy gain (cf. white dashed lines in fig. 7.3). Nearly zero chirp is measured at optimum compression strength where the temporal focus is at the streaking foil. The blue line is calculated according to eqn 7.9. (d) Line profile of the cross-correlation of the shortest electron pulse at $g_E = 20.1\,\mathrm{eV/ps}$, integrated over ∼15 eV below the cutoff energy gain. A Gaussian fit yields a duration of (35 ± 3) fs FWHM, corresponding to a standard deviation of (15 ± 1) fs.

Here, 267 nm UV pulses are used for photoemission (cf. sections 5.1, 5.3, and 6.3) with a duration of (90 ± 20) fs FWHM at the photocathode after a dispersive vacuum window, implying $\tau_{\mathrm{initial}} = (90 \pm 20)$ fs FWHM (cf. section 5.3). The dispersed electron pulse's duration at the entrance of the microwave cavity is measured as $\tau_{\mathrm{disp}} = (360 \pm 20)$ fs FWHM[3] (cf. section 7.1). Thus, the energy spread imprinted

[3] In fact, the duration of the uncompressed electron pulse is measured at the streaking foil rather than directly at the position of the microwave cavity. However, according to eqn 7.4, the small energy bandwidth leads to an error of only ∼10 fs due to the additional distance.

onto the electrons at $g_E = 20.1\,\mathrm{eV/ps}$ for optimum compression at the streaking foil is about 7.2 eV FWHM (cf. eqn 5.4). The measured initial energy spread, extracted from the tilt of the interference orders of the uncompressed electron pulse (cf. fig. 7.2 (a)) and its duration, is $\Delta\varepsilon \approx 0.4\,\mathrm{eV}$ FWHM [87, 93] and therefore the electron pulse's duration at the temporal focus is $\tau_{\mathrm{final}} \approx 4.9\,\mathrm{fs}$ FWHM for ideal phase-space-limited compression, according to eqn 3.2. This is shown as the green line in fig. 7.4 (a), while the blue line indicates the duration of the cross-correlation, assuming $\tau_{\mathrm{final}} \approx 35\,\mathrm{fs}$ FWHM, which is the minimum measured duration, as shown in fig. 7.4 (d). Note that the duration of the cross-correlation, which constitutes an upper limit for the electron pulse's duration, falls significantly below τ_{initial} (red dotted line in fig. 7.4 (a)) around the optimum compression strength.

The FWHM energy bandwidth of the electron pulses after the interaction with the microwave field is extracted directly from the "unstreaked" energy spectra, i.e. without the streaking laser pulse, and depicted in fig. 7.4 (b). According to eqn 5.4, the energy broadening imprinted by the microwave field onto an electron pulse of a duration τ_{disp} is simply given by g_E. The initial energy bandwidth after photoemission, $\Delta\varepsilon$, is negligible for realistic values of the compression strength g_E:

$$\Delta E = \sqrt{\tau_{\mathrm{disp}}^2 g_E^2 + \Delta\varepsilon^2} \approx |\tau_{\mathrm{disp}} g_E| \tag{7.8}$$

The calculated energy bandwidth is shown as the blue line in fig. 7.4 (b), in good agreement with the measurement (black diamonds).

The linear chirp of the electron pulses is defined in analogy to optics as the derivative of the arrival time of each energy component constituting the pulse's phase space with respect to energy, in units of ps/eV. In the phase space diagram depicted in fig. 3.1 as well as in the measured streaking spectrograms this corresponds to the inverse slope of the peak delay time of each energy slice (white dashed lines in fig. 7.3). Furthermore, the sign of the chirp is positive if the low-energetic components are further advanced in time, i.e. arrive earlier at the target, than the high-energetic components; therefore, vacuum dispersion without microwave compression leads to a negative chirp, since electrons at higher kinetic energies propagate faster. Fig. 7.4 (c) shows the chirp evaluated from the spectrograms at the decrease feature around zero energy gain (black diamonds). Without the microwave field (cf. fig. 7.2 (a)), the chirp is negative. As the microwave compression strength increases, the chirp's sign becomes positive and its magnitude is successively reduced to zero at optimum compression (nearly vertical white dashed line in the central spectrogram in fig. 7.3). At higher values of the compression strength, the sign of the chirp is negative again, since the high-energetic components outrun the low-energetic components after the temporal focus and arrive earlier at the streaking foil. The chirp of the electron

pulses, C_{el}, at the streaking foil depends on three constituents: the dispersed chirp, C_{disp}, at the entrance of the microwave cavity, the effect of energy modulation by the microwave, g_E, and the subsequent dispersion through free propagation, D_{vac}, which leads to temporal compression or broadening. As discussed in section 3.1, the microwave field modulates the electron pulse's phase space in the energy domain, while vacuum dispersion modulates it in the time domain. Hence, we obtain:

$$C_{\mathrm{el}} = \frac{1}{C_{\mathrm{disp}}^{-1} + g_E} - f D_{\mathrm{vac}} \tag{7.9}$$

Note that C_{disp} is calculated from the chirp $C_{\mathrm{el},0}$, which is measured at the streaking foil without microwave compression ($g_E = 0$), according to eqn 7.9: $C_{\mathrm{disp}} = C_{\mathrm{el},0} + f D_{\mathrm{vac}}$. The calculated chirp as a function of g_E is shown as the blue line in fig. 7.4 (c), using $C_{\mathrm{disp}} \approx -1.76\,\mathrm{ps/eV}$ obtained from the streaking measurement without compression. The singularity at $g_E = -C_{\mathrm{disp}}^{-1} \approx 0.57\,\mathrm{eV/ps}$ denotes the microwave compression strength required to exactly compensate for the chirp due to the initial dispersion in vacuum. This mode of operation, though undesirable for temporal compression, can be utilized to compress the electron pulse's energy bandwidth rather than its duration, since the correlation between kinetic energy and delay time is removed here, conserving the phase space volume (cf. sections 2.2 and 3.1), while the dispersed duration, τ_{disp}, is maintained.

The remarkable agreement of the simple analytical model with the measured phase space transformations verifies the linearity and reliability of electron pulse compression with microwave fields, constituting a longitudinal "lens" for electron pulses [77]. At the optimum compression strength, a duration of the cross-correlation of $(35 \pm 3)\,\mathrm{fs}$ FWHM or $(15 \pm 1)\,\mathrm{fs}$ rms is achieved, as shown in fig. 7.4 (d), which deviates from the ideal compression due to the residual contribution of the streaking laser pulse's duration, laser-microwave jitter, and geometric broadening (see section 7.3).

7.3 Shortest electron pulses

As pointed out in section 7.1, the duration of the cross-correlation obtained by optical streaking is a convolution between the electron pulse's duration and an energy-gain-dependent sampling function which is given by the envelope of the streaking laser pulse's electric field. Therefore, the duration of the cross-correlation converges towards the electron pulse's duration above a certain energy gain value where the temporal width of the streaking field envelope becomes significantly shorter than the electron pulse's duration (cf. fig. 7.2 (c)). When microwave compression is employed,

the electron pulse's duration becomes comparable to the streaking pulse's duration or even shorter; thus, the temporal width of the streaking field envelope significantly contributes to the duration of the cross-correlation, even close to the cutoff energy gain. The spectrogram at optimum compression is integrated over ∼15 eV below the cutoff energy gain, i.e. from 65 eV to 80 eV, in order to extract the duration of the cross-correlation (cf. fig. 7.4 (d)). The center of this range is about 10 % below the cutoff. A Gaussian streaking laser pulse with a duration of the intensity envelope of 50 fs FWHM (cf. section 4.3), corresponding to a temporal width of the field envelope of $50\,\text{fs} \cdot \sqrt{2} \approx 71\,\text{fs}$ FWHM, has a duration of ∼28 fs (full width) at 10 % below the peak, which is close to the measured duration of the cross-correlation of ∼35 fs FWHM. This motivates precise modeling of the laser-electron interaction at the streaking foil in order to deconvolute the actual electron pulse's duration from the cross-correlation.

Fig. 7.5 shows the calculated field of the streaking laser pulse in comparison to the spectrogram at optimum compression strength (cf. fig. 7.3). The streaking field is derived by Fourier transformation of the measured optical spectrum (cf. fig. 4.3 (a)), assuming zero group delay dispersion (linear chirp), which is compensated at the streaking foil by adjusting the prism compressor (cf. section 4.3), and $-20\,200\,\text{fs}^3$ of uncompensated third-order dispersion. A significant asymmetry and a temporally broad pedestal are evident and also qualitatively reproduced at low energy gain values in the streaking spectrogram. The temporal width of the field envelope is 53 fs FWHM. The portion of the streaking pulse's field contributing to the duration of the cross-correlation, integrated from 65 eV of energy gain until the cutoff energy gain, is marked by the upper red arrows. The temporal width of the streaking field corresponding to an energy gain of 65 eV is ∼32 fs, which is comparable to the measured duration of the cross-correlation in this energy range, as discussed above.

A semi-classical simulation of the laser-electron interaction at the streaking foil is performed in order to deconvolute the electron pulse's duration from the measured cross-correlation. The electron is treated as a non-relativistic quantum mechanical wave packet in a classical optical field and the interaction at the streaking foil is assumed to be instantaneous. A detailed formalism can be found in [93]. The calculated streaking laser field (cf. fig. 7.5 (a)) is used in the simulation with a peak field amplitude fixed at 2 GV/m, corresponding to the measured cutoff energy gain of about 80 eV (cf. eqn 7.2). The coherence time of each single-electron wave packet is set to about 100 as of standard deviation, according to the uncertainty relation and the energy bandwidth imprinted by the microwave field (cf. section 2.1). At each laser-electron delay step, the interaction of single-electron wave packets with the streaking field is integrated over a Gaussian temporal electron density with a duration of τ_{final} (cf. the illustration in fig. 2.1). In addition, an integration over

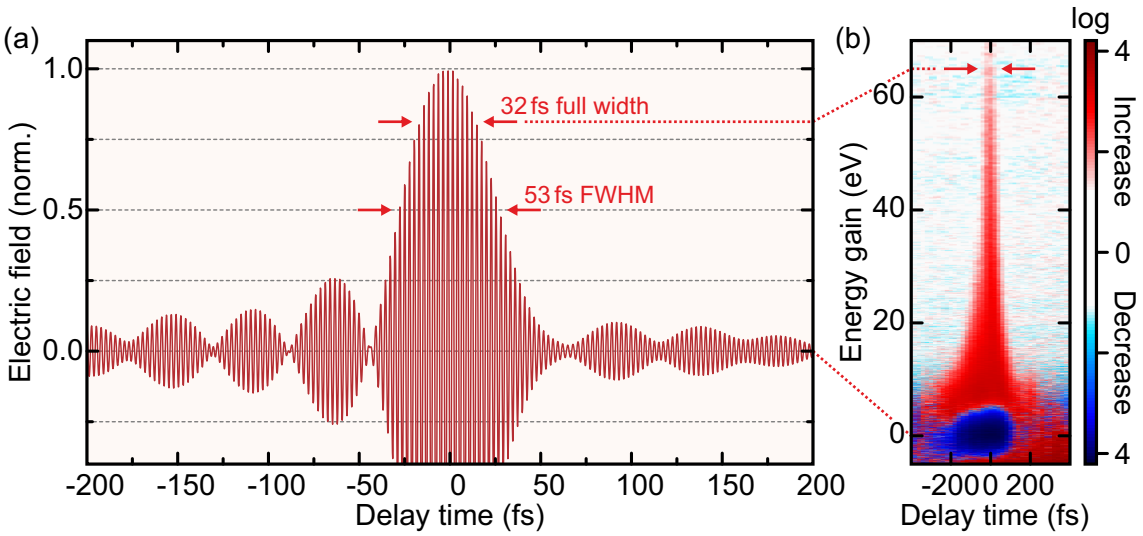

Figure 7.5: Contribution of the streaking laser pulse's temporal profile to the cross-correlation. (a) Streaking laser field calculated from the optical spectrum (cf. fig. 4.3 (a)) and uncompensated third-order dispersion of $-20\,200\,\mathrm{fs}^3$. The group delay dispersion (linear chirp) is compensated by the prism compressor and assumed to be zero. The pulse exhibits significant asymmetry and a broad temporal pedestal; the duration is 53 fs FWHM. (b) Spectrogram at optimum compression strength (cf. fig. 7.3) for comparison, which qualitatively reproduces the asymmetry as well as the pedestal. The upper red arrows mark the integration range used to calculate the duration of the cross-correlation, starting at 65 eV of energy gain, and the corresponding duration of the streaking pulse's field in (a) of about 32 fs.

the Gaussian cross-section of the interaction area between the streaking laser pulse and the electron pulse at the streaking foil accounts for the non-uniform streaking field strength across the beam diameter. Here, the laser beam's diameter at the foil is 56 µm × 86 µm FWHM, projected onto the electron beam's axis, and the electron beam is focused to a diameter of 94 µm × 113 µm FWHM (smaller than in section 7.1). τ_{final}, being the compressed electron pulse's duration, as well as the third-order dispersion of the laser pulse, defining the shape of the streaking field, are used as optimization parameters in order to maximize the agreement between the simulation and the measurement.

Fig. 7.6 shows the results of the simulation in comparison with the measurement. The measured streaking spectrogram at optimum compression strength (cf. fig. 7.3) is depicted in fig. 7.6 (a), while the simulated spectrogram is shown in fig. 7.6 (b). The best agreement with the measurement is achieved for a third-order dispersion of $-20\,200\,\mathrm{fs}^3$ (cf. fig. 7.5 (a)) and $\tau_{\mathrm{final}} = 28$ fs FWHM. Ripples of the streaking field envelope are clearly visible in the simulated spectrogram, while they are smeared out in the measured spectrogram due to larger steps of the delay time (∼20 fs), drift, and noise. Nevertheless, the outer shape shows good agreement. Fig. 7.6 (c) depicts

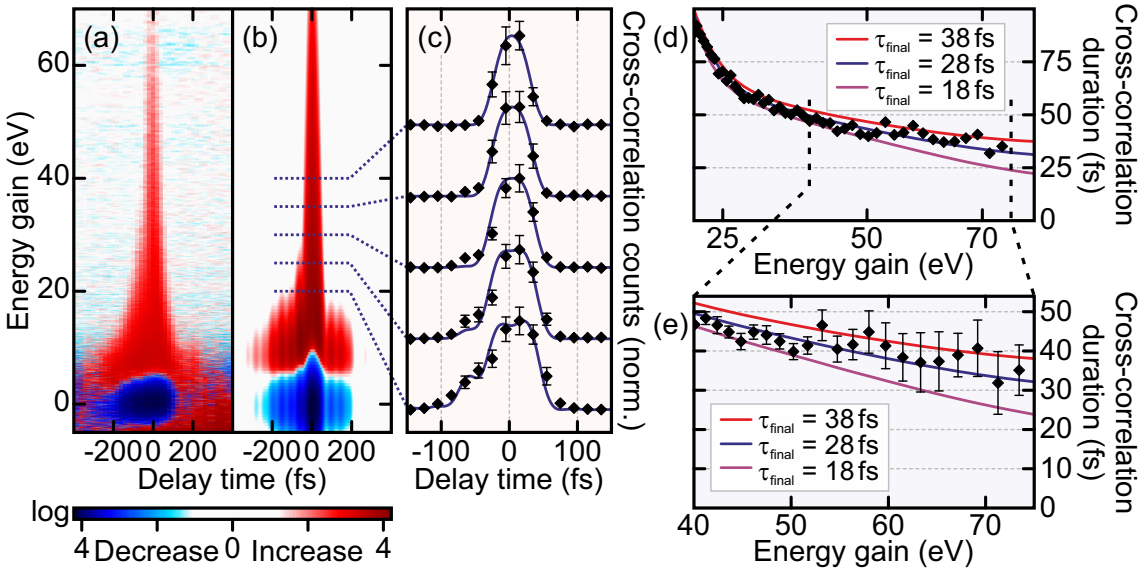

Figure 7.6: Semi-classical simulation of the laser-electron interaction at the streaking foil and comparison with the measurement. (a) Measured streaking spectrogram at optimum compression strength (cf. fig. 7.3). (b) Simulated streaking spectrogram which fits best to the data, using the third-order dispersion of the laser pulse and the electron pulse's duration as parameters. The streaking laser field in fig. 7.5 (a) is used and an electron pulse's duration of 28 fs FWHM. (c) Line profiles extracted from (a) (black diamonds) and from (b) (blue lines) at 20 eV, 25 eV, 30 eV, 35 eV, and 40 eV of energy gain, each integrated over a range of ∼2 eV. (d) Gaussian FWHM duration of the measured cross-correlation (black diamonds) as a function of the energy gain in comparison to three simulations (solid lines), assuming a duration of the compressed electron pulse of 38 fs FWHM (red), 28 fs FWHM (blue), and 18 fs FWHM (purple). (e) Zoom of (d), revealing the best agreement with the measured data for an electron pulse's duration of $\tau_{\text{final}} = 28$ fs FWHM.

line profiles extracted from the measured spectrogram (black diamonds) and from the simulation (blue lines) at different energy gain values, each integrated over a range of ∼2 eV. The error bars denote statistical errors of the measured spectrogram within the integration range. The FWHM duration of the cross-correlation as a function of the energy gain is shown in fig. 7.6 (d), evaluated by fitting a Gaussian to each line profile (cf. fig. 7.2 (c)). The measurement (black diamonds) is depicted in comparison to three simulations (solid lines), assuming a compressed electron pulse's duration of $\tau_{\text{final}} = 38$ fs FWHM (red), $\tau_{\text{final}} = 28$ fs FWHM (blue), and $\tau_{\text{final}} = 18$ fs FWHM (purple), respectively. Fig. 7.6 (e) shows a zoom of fig. 7.6 (d), revealing the best agreement of the simulation with the measurement for an electron pulse's duration of $\tau_{\text{final}} = 28$ fs FWHM. The error bars denote uncertainties of the respective Gaussian fits. The overall good agreement of the simulation with the measurement justifies a deconvoluted compressed electron pulse's duration of (28 ± 5) fs FWHM or (12 ± 2) fs rms, the error margin being estimated from fig. 7.6 (e).

This demonstrates a temporal compression of the electron pulses by more than an order of magnitude as compared to the dispersed pulses at the entrance of the microwave cavity, having a duration of $\tau_{\mathrm{disp}} = (360 \pm 20)\,\mathrm{fs}$ FWHM. Moreover, the compressed single-electron pulses reported here are about threefold shorter than the UV laser pulses used for photoemission and about sixfold shorter than previous demonstration of microwave compression using dense electron pulses [70], constituting, to our knowledge, the shortest electron pulses at a kinetic energy suitable for UED. Ideally, phase-space-limited compression implies a compressed electron pulse's duration of about 5 fs FWHM (cf. section 7.2). The deviation of this value from the measured duration is attributed to the nonlinear phase space transformation during the initial acceleration, transverse distortions of the beam profile inside electric and magnetic fields (cf. section 3.3), imperfect group velocity matching between the laser and the electron beam at the streaking foil (cf. section 7.1), and residual laser-microwave jitter and drift (cf. sections 4.5 and 6.3). The estimated temporal broadening due to these contributions, as discussed in the respective sections, is in good agreement with the achieved duration of the compressed electron pulse. Further compression into the few-femtosecond domain and below requires addressing all sources of temporal broadening, especially the quality of laser-microwave synchronization [136, 137] and geometric broadening [105] (see sections 8.2 and 8.3).

The characterization of electron pulse compression described in this work is also suitable for multi-electron pulses. In order to assess the influence of space charge on the achievable pulse duration, identical streaking measurements as reported above for single-electron pulses are also performed for 3, 10, 15, 27, and 43 electrons per pulse. The number of electrons per pulse is adjusted via the pulse energy of the UV laser pulses used for photoemission. The FWHM duration of the compressed electron pulses is obtained for each measurement by deconvolution, as described above, and shown in fig. 7.7. The optimum compression strength required to set the temporal focus at the streaking foil increases from 20.1 eV/ps for single-electron pulses to 25.3 eV/ps for 43 electrons per pulse. This trend is also predicted by simulations (cf. fig. 3.2), since the growing Coulomb repulsion around the temporal focus retards the compression. A significant temporal broadening is already evident for few electrons per pulse, roughly doubling the single-electron pulse's duration at 10 electrons per pulse. Nevertheless, this temporal resolution is still sufficient for studying interesting ultrafast structural dynamics at a tenfold electron flux, substantially reducing the acquisition time or providing improved statistics. Note that space-charge-induced broadening crucially depends on the electron's kinetic energy and the beam geometry throughout the entire propagation. A compressed electron pulse's duration of about 160 fs FWHM has been achieved for dense pulses of about 10^6 electrons at a similar distance of the temporal focus as reported in this work [70], albeit at a relativistic

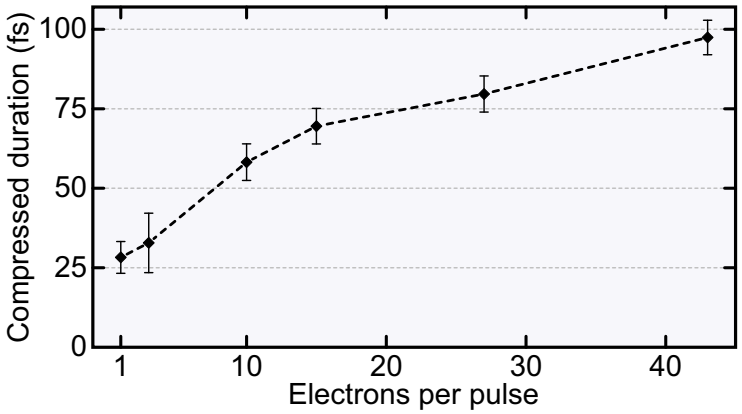

Figure 7.7: Broadening of multi-electron pulses due to space charge. The deconvoluted electron pulse's FWHM duration (black diamonds) is shown for 1, 3, 10, 15, 27, and 43 electrons per pulse, the black dashed line being a guide to the eye. The optimum compression strength increases from 20.1 eV/ps for single-electron pulses to 25.3 eV/ps for 43 electrons per pulse. Temporal broadening due to space charge is evident even for few electrons per pulse.

kinetic energy of 95 keV and a beam diameter of about 1 mm FWHM. Although temporal broadening due to space charge is certainly less severe at higher kinetic energies, fig. 7.7 clearly demonstrates the necessity of single-electron pulses in order to study electronic dynamics on a few-femtosecond or attosecond time scale.

7.4 Application: Static diffraction and EELS

In order to verify the feasibility of atomic-scale imaging with compressed single-electron pulses, static diffraction patterns are recorded from an organic molecular crystal of N-(triphenylmethyl)-salicylidenimine (schematic structure is shown as an inset in fig. 7.8 (a)), which forms a bi-molecular unit cell with a size of about 1 nm × 1 nm × 1 nm. Free-standing films of 50 nm thickness are produced by ultramicrotomy [86] and placed at the temporal focus. Diffraction is observed via a phosphor screen coupled to a CMOS camera chip (cf. section 5.1) with the ToF spectrometer removed. Fig. 7.8 shows the diffraction patterns for two cases, one with the spatial focus set at the sample for maximum diffraction efficiency (fig. 7.8 (a)) and one with the spatial focus adjusted onto the screen for maximum coherence and sharpness of the Bragg spots (fig. 7.8 (b)). Some asymmetry remains due to imperfect angular alignment. The observed sharpness of the spots in fig. 7.8 (b) indicates that the microwave compression and the associated energy broadening does not deteriorate the superior transverse coherence of the original single-electron source [86]. This demonstrates the ability to achieve atomic resolution with single-electron pulses using compression with microwave fields.

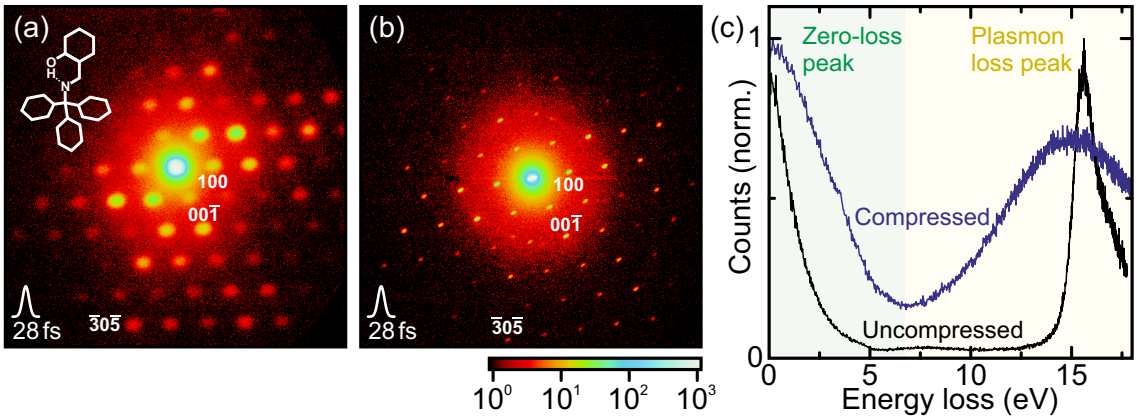

Figure 7.8: Static diffraction and EELS with compressed single-electron pulses. (a) Diffraction pattern obtained with compressed single-electron pulses focused on an organic molecular crystal of N-(triphenylmethyl)-salicylidenimine (structure shown as an inset) with unit cell dimensions of about 1 nm. (b) Diffraction pattern with the electron beam focused through the sample onto the screen for maximum coherence and sharpness of the Bragg spots. The measured intensities and the sharpness of the spots demonstrate the ability to achieve atomic-scale resolution with compressed single-electron pulses. The electron counts are color-coded on a logarithmic scale and some characteristic Bragg spots are labeled in the diffraction images. (c) EELS spectra of aluminum obtained with uncompressed (black line) and compressed (blue line) single-electron pulses. The plasmonic loss peak at about 15 eV of energy loss, representing the bulk metal's plasma frequency, is clearly distinguishable from the zero-loss peak in both cases.

As pointed out in the introduction of chapter 6, EELS is another powerful method for time-resolved structural analysis [172, 173]. Fig. 7.8 (c) shows an EELS spectrum of the aluminum foil used for streaking, recorded with uncompressed (∼360 fs FWHM, black line) and compressed (∼28 fs FWHM, blue line) electron pulses, respectively. The well-known plasmonic loss peak at about 15 eV of energy loss in aluminum, representing the bulk metal's plasma frequency [178], is clearly distinguishable from the zero-loss peak in both cases, despite the significant spectral broadening due to microwave compression. This suggests time-resolved electron spectroscopy as another promising method for investigating matter transformations with the unprecedented temporal resolution offered by the compression technique developed in the course of this work.

In conclusion, this work presents ultrashort electron pulses for UED, capable of resolving the fastest atomic and molecular motion in space and time. Although spatial and temporal resolution are demonstrated separately, the implementation of this electron source into an actual UED experiment is straightforward and the subject of current research. These results pave the way for future applications of UED as a tool for observing charge densities in motion on an atomic length scale and an electronic time scale.

Chapter 8

Towards attosecond electron diffraction: Route and caveats

In summary, this work conclusively demonstrates record-short single-electron pulses for UED at a de Broglie wavelength of 0.08 Å, or a kinetic energy of 25 keV, with a duration of (28 ± 5) fs FWHM or (12 ± 2) fs rms. This duration is measured with respect to the timing of femtosecond laser pulses, denoting the realistically achievable effective temporal resolution of UED pump-probe experiments employing ultrashort laser pump pulses and single-electron probe pulses. The transverse coherence is suitable for diffraction from complex molecular crystals. The temporal resolution is already sufficient for 4D imaging of the fastest known atomic motion in chemical reactions, such as intra-molecular proton transfer, occurring on a time scale of 30 fs–100 fs [11]. Currently, only large-scale X-ray FEL facilities offer slightly shorter pulses capable of atomic-scale imaging, but with reduced spatial resolution (cf. fig. 1.2).

Essentially, the unprecedented electron pulse duration reported here is due to the combination of four concepts: single-electron pulses (cf. chapter 2), a microwave compression technique (cf. chapter 3), superior temporal synchronization of the microwave source to a femtosecond mode-locked laser (cf. chapter 4), and temporal characterization by optical field streaking offering potentially attosecond resolution (cf. chapter 7).

Fundamentally, at kinetic energies of tens of keV, the shortest duration of single-electron pulses allowed by the uncertainty principle is on the order of zeptoseconds (10^{-21} s) at accordingly high bandwidths. The nearly linear phase space transformation afforded by the microwave cavity (cf. section 7.2) demonstrates that the microwave compression technique can confine single-electron wave packets almost arbitrarily in time, limited only by the acceptable energy bandwidth (see section 8.4). Thus, the temporal resolution of single-electron UED can potentially compete with

or even surpass the resolution of attosecond laser spectroscopy (cf. section 1.3). The results and concepts of this work mark an important first milestone towards this goal and motivate further improvement. The unfolding perspectives and remaining challenges of advancing UED into the few-femtosecond or attosecond domain are discussed in the following.

8.1 Promising first sample systems for attosecond dynamics

Several fundamental processes driven by few-femtosecond and attosecond electronic motion are pointed out in chapter 1, such as Auger relaxation after atomic inner-shell excitation, electron tunneling in atoms, collective electron motion (plasmons and polaritons), and the polarization response of a material to external electric fields [5, 179]. Many of these processes have been studied via spectroscopy with attosecond optical pulses. This requires excitation of suitable transitions by the probe pulse and a subsequent change of transition probability during the course of the dynamics. The large photon energy and bandwidth of attosecond optical pulses (typically XUV or soft X-ray radiation) in comparison to atomic potential energies of valence electrons or chemical bonds thus limits attosecond spectroscopy to quite specific sample systems. In addition, spectroscopy only provides access to energy levels without direct structural information.

In contrast, UED potentially offers direct visualization of charge densities independent of internal energy levels and transitions. The concepts described here indicate the possibility to eventually reach electron pulse durations of few femtoseconds or below. At these time scales, motion of electron densities in matter can be observed, while nuclei are almost stationary [5].

Fig. 8.1 illustrates two proposed applications for studying attosecond electronic dynamics by UED, using crystalline molecular iodine as a model system [5]. The crystal structure consists of diatomic molecules, two electrons contributing to an intramolecular σ bond for each molecule with a length of $\sim$2.7 Å. Fig. 8.1 (a) depicts the first potential application which is an anti-bonding excitation of the system. The redistribution of electron density during the transition from covalently bound molecules into a (transient) crystal of isolated atoms is accompanied by a significant change in the Bragg spot intensities, on the order of 10 %–30 %, before any nuclear motion takes place [5]. The temporal resolution available for mapping out this process is limited by the duration of the laser pump pulses used for excitation.

Iodine atoms, due to their large mass, do not move significantly within the first tens of femtoseconds. The electron pulses achieved in this work are short enough

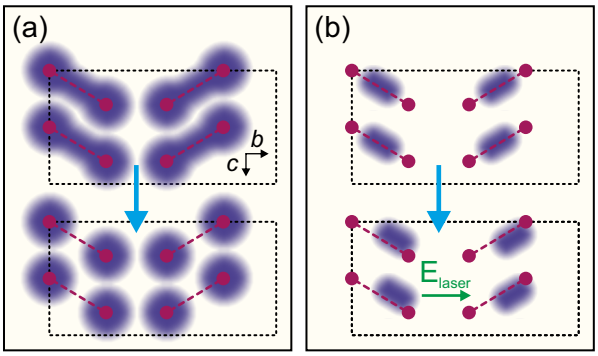

Figure 8.1: Schematic of proposed attosecond UED applications for studying electronic dynamics, using crystalline molecular iodine as a model system; figure adapted from [5]. (a) Transition of molecular bonding order upon excitation from a bonding (upper panel) into an anti-bonding state (lower panel). (b) Displacement of electron density, mainly intramolecular bonding electrons, in a non-resonant external laser field, constituting the material's polarization response.

to potentially visualize the electron density of the S_1 excited state prior to any atomic motion, hence providing information on the photophysical forces responsible for photochemical reactions. Challenges for realizing this experiment are preparation of an iodine crystal for diffraction in transmission and investigation of thermal stress (see section 8.2). One of the central difficulties, the electron pulse's duration, is now solved in this case.

The second proposed application, as shown in fig. 8.1 (b), is the displacement of electron densities in the presence of an external electric field, such as a laser field at optical frequencies. Depending on the local atomic or molecular potential, electron densities follow the external field with a phase delay, constituting the material's polarization response and refractive index, which is in general nonlinear at high external field strengths. Non-uniform displacement of the charge densities can be visualized by means of electron diffraction without the need for the (slower) nuclei to move, provided sufficiently short electron pulses capable of resolving the optical field oscillations. At non-resonant frequencies of the external field, little energy is transferred to the system – in contrast to resonant excitation of electronic transitions in the case of spectroscopy – which minimizes thermal stress of the sample, especially since single-electron UED requires a large number of pump-probe cycles (see section 8.2).

In fig. 8.1 (b), an external electric field is applied along the b axis, which is the axis of least symmetry. A field amplitude of about 1 GV/m, readily provided by a femtosecond laser pulse, is below the damage threshold of the sample and causes a charge displacement of the intramolecular bond of $\sim$0.08 Å. The corresponding

changes in the intensities of some Bragg spots are on the order of ±15 %, allowing visualization of sub-ångström displacement of charge densities [5].

First studies of electronic polarization response upon non-resonant optical excitation have been experimentally conducted by time-resolved hard-X-ray diffraction [179], albeit without sub-optical-cycle temporal resolution yet. This shows that 4D imaging of electronic processes is possible by diffraction. Here, electron diffraction offers the possibility of attosecond temporal resolution, enabling investigation of fundamental light-matter interaction in the time domain.

8.2 Stability, thermal stress, and reversibility

Dense electron bunches are widely used for UED, since they allow acquisition of high-quality diffraction snapshots of the specimen's transient structure during a single pump-probe cycle (single-shot UED), providing a temporal resolution of several 100 fs after microwave compression [70, 96]. Only few pump-probe cycles are required to map out the entire dynamics of the system under investigation when using single-shot UED. A low repetition rate in the kHz range or below is therefore sufficient for reasonable acquisition times. This also minimizes the thermal energy transferred to the sample by the excitation, avoiding thermal damage of the sample. Moreover, investigation of irreversible processes is facilitated. However, approaching sub-femtosecond temporal resolution with UED necessitates single-electron pulses, since Coulomb repulsion within a dense electron bunch substantially limits the achievable electron pulse's duration after microwave compression (cf. section 7.3).

In contrast to dense electron bunches, using single-electron pulses requires averaging over many pump-probe cycles (roughly 10^5–10^6) for a single pump-probe delay step in order to obtain a diffraction image with a sufficient signal-to-noise ratio for detecting small changes in the positions and intensities of the Bragg spots. This restricts the application of single-electron UED to highly reversible processes, unless the specimen is rapidly and reproducibly replaced. Furthermore, the repetition rate of single-electron UED has to be ideally in the 100 kHz to MHz range in order to maintain a reasonable acquisition time. Thus, thermal energy deposited by the optical pump pulses can accumulate and damage a thin-film crystalline sample (cf. section 1.3). This constraint is significantly relaxed when studying dynamics of electron densities which are non-resonantly driven by external fields, avoiding deposition of thermal energy inside the specimen by absorption (cf. section 8.1).

Higher kinetic energies of the electrons than reported here allow using thicker specimens for UED, which are less susceptible to thermal damage. The microwave power required for electron pulse compression scales with the cube of the kinetic energy. Therefore, increasing the kinetic energy from 25 keV to 100 keV requires in-

creasing the microwave power inside the compression cavity used in this work from ∼100 mW to about 6.4 W at a frequency of ∼6.2 GHz for a distance to the temporal focus of about 24 cm. Although this increase in power demand is substantial, such a power level can be readily provided with little technical effort by solid-state microwave amplifiers. The available microwave power gives rise to a trade-off between the maximum achievable ratio of temporal compression (see section 8.4) and the maximum usable kinetic energy of the electrons.

Long-term stability is essential for single-electron UED, which typically requires measurement times on the order of hours for mapping out structural dynamics via diffraction with a sufficient signal-to-noise ratio. A drift of the microwave signal's phase with respect to the laser's repetition rate on the order of 100 fs peak-to-peak on a half-hour time scale is evident for the passive synchronization scheme presented in this work (cf. section 6.3). Moreover, residual high-frequency phase noise of the microwave signal contributes to the limit of the achievable compressed electron pulse's duration in this work (cf. section 4.5). Both issues can be addressed by an improved active laser-microwave synchronization based on optical interferometric laser-microwave phase detection, promising sub-femtosecond stability with regard to timing drift and jitter [136, 137].

8.3 Isochronic electron beams

Spatial distortions of the electron beam in electron-optical elements, such as the anode hole, magnetic lenses, or the compression cavity, lead to a curved pulse front and thus temporal broadening. In this work, the magnitude of this broadening is comparable to the residual timing jitter of the microwave source (cf. sections 3.3 and 4.5) and constitutes another significant contribution to the limit of the achievable compressed electron pulse's duration. Therefore, avoiding transverse distortions of the beam profile is crucial for achieving electron pulse durations on the order of few femtoseconds and below.

Fig. 8.2 (a) schematically shows an isochronic beam geometry for minimizing spatial distortions [105], consisting of a magnetic lens after the compression cavity. This geometry ensures a constant timing over the entire transverse beam profile at a simultaneous spatial and temporal focus. Particle tracking simulations of the beam diameter and the electron pulse's duration during propagation are depicted in fig. 8.2 (b) for different values of the cavity's compression strength. The spatial focus is set via the current through the magnetic lens to coincide with the cavity's temporal focus. Further details can be found in [105]. Although a simultaneous spatial and temporal focus is evident for all compression strengths, there is a clear minimum of the achievable electron pulse's duration at the focus for a magnification by

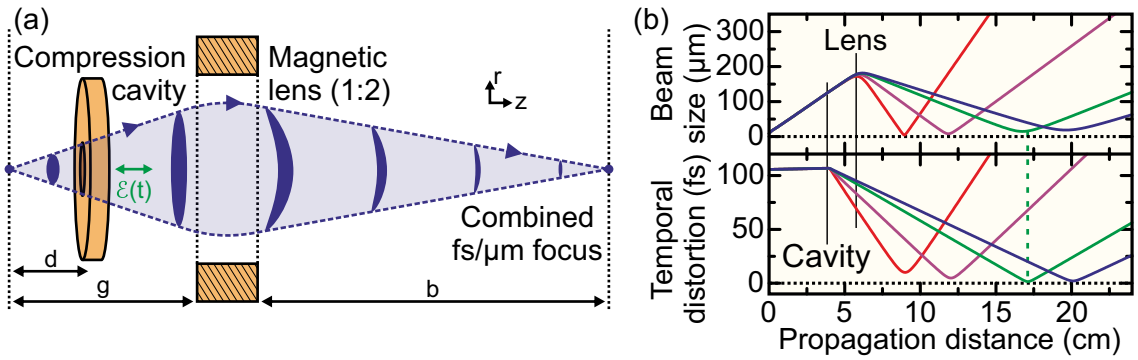

Figure 8.2: Avoiding transverse distortions in electron-optical elements; data and figure taken from [105]. (a) Schematic of an isochronic beam geometry with a magnetic lens (g = 6 cm) after a compressing microwave cavity (d = 4 cm), providing a simultaneous spatial and temporal focus for a magnification by the magnetic lens of about 1:2. (b) Particle tracking simulations showing the beam diameter and electron pulse's duration (all values denote FWHM) for different values of the microwave cavity's compression strength, setting the temporal focus at a propagation distance of 9 cm (red), 12 cm (purple), 17 cm (green), and 19.5 cm (blue). In each case, the current of the magnetic lens is chosen to produce a spatial focus at the same distance as the cavity's temporal focus. Focusing in space and time is evident for all cases; however, spatiotemporal distortions are minimized for a magnification of about 1:2 (green), yielding a beam diameter of ∼20 μm and a pulse duration of ∼1.4 fs at the focus.

the magnetic lens of about 1:2. For typical electron beam parameters similar to the experimental parameters in this work and a distance to the temporal focus of about 13 cm after the microwave cavity, the electron pulse is compressed to a FWHM duration of ∼1.4 fs, while the FWHM beam diameter at the focus is ∼20 μm [105]. An isochronic beam geometry using other magnification ratios than 1:2 requires an additional magnetic lens [105].

8.4 Duration and bandwidth of electron pulses

There is a fundamental limit for the duration of electron pulses and thus the temporal resolution of UED. In analogy to optical pulses, the intrinsic duration of a single-electron wave packet is limited to roughly one de Broglie period. At kinetic energies suitable for diffraction – on the order of 10 keV to 1 MeV – this single-cycle limit is in the zeptosecond range, which is far below any current technological constraint. However, the sharpness of the Bragg spots is limited by the bandwidth of the electron pulses, the spread of the diffraction angles being given by the relative energy spread for small angles and small relative bandwidths.

The microwave compression technique presented in this work squeezes the electron pulse's phase space distribution in the temporal domain at the expense of an

according increase in bandwidth. Thus, according to eqn 3.2, any compression ratio is in principle achievable, provided a sufficiently strong linear temporal gradient of the microwave field (i.e. compression strength) and as long as the imprinted energy spread is tolerable by the UED application. For example, using 50 fs UV laser pulses for photoemission, the electron pulses can be compressed to 50 as, while the energy spread increases from typically 0.2 eV–0.3 eV to about 200 eV–300 eV, which is still acceptable for diffraction at a central energy of tens of keV. Here, the distance to the temporal focus is on the order of millimeters (cf. eqn 7.6). It can be increased to more practical lengths by allowing the electron pulse to disperse before entering the compression cavity, e.g. by using a smaller static acceleration field, thus requiring a smaller compression strength to gain the same amount of energy spread. Moreover, the initial bandwidth can be minimized by tuning the laser's photon energy close to the photocathode's work function [82] or by using an ultracold electron source [84]. This increases the maximum compression ratio for a given maximum acceptable energy spread.

8.5 Characterization of ultrashort electron pulses

Notably, the compressed electron pulses demonstrated in this work are shorter than the laser pulses involved in their generation and characterization. Ultrashort electron pulses with durations well below the period of an optical cycle facilitate applying transients of optical fields for both interaction with charge densities in suitable samples on attosecond time scales (cf. section 8.1) as well as *in-situ* characterization via optical field streaking (cf. section 7.1).

Fig. 8.3 depicts simulated streaking spectrograms of the laser-electron cross-correlation described in section 7.1 [93]; durations denote FWHM. Fig. 8.3 (a) qualitatively reproduces the measurement in fig. 7.2 (a), assuming a 50 fs laser pulse and a 300 fs chirped electron pulse which coherently extends over several laser cycles, approximately reflecting the experimental conditions. When using few-cycle laser pulses (5 fs duration) with stabilized carrier-envelope phase for streaking and reducing the electron pulse's duration close to the period of an optical cycle (3 fs), depicted in fig. 8.3 (b), the spectrogram shows a transition from the regime of cycle-averaged coherent interference to field-resolved sampling [13]. Further reducing the electron pulse's duration well below the period of an optical cycle (1 fs), as shown in fig. 8.3 (c), yields a spectrogram very similar to attosecond XUV streaking spectrograms [31], accurately mapping the laser pulse's vector potential and thus its electric field. Therefore, few-femtosecond and sub-femtosecond electron pulses offer the potential of probing optical-field-induced dynamics of charge densities in matter by UED, combining the superior temporal resolution of attosecond XUV spectroscopy

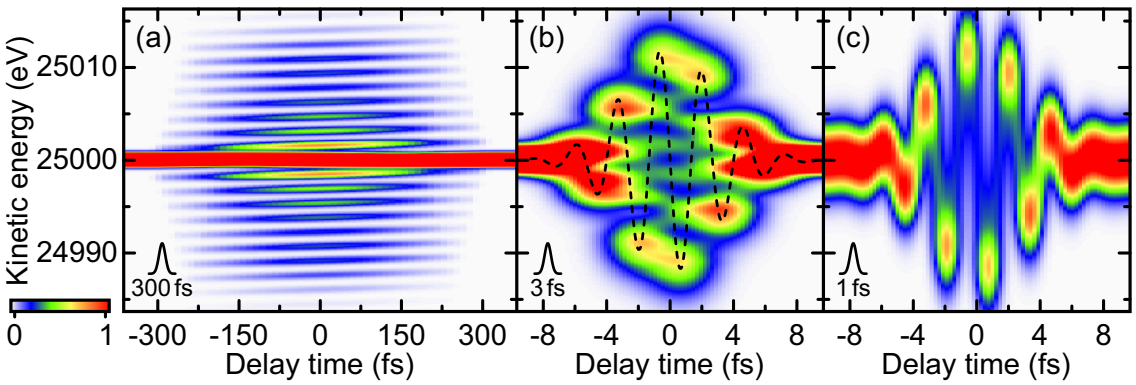

Figure 8.3: Simulated streaking spectrograms of the laser-electron cross-correlation described in section 7.1 (durations denote FWHM); data and figure taken from [93]. (a) A 50 fs laser pulse at a wavelength of 800 nm and a 300 fs chirped electron pulse at a central energy of 25 keV coherently extending over several laser cycles qualitatively reproduce the tilted interference pattern in fig. 7.2 (a). (b) A transition between the coherent interference regime and field-resolved sampling is visible for a 5 fs laser pulse with stabilized carrier-envelope phase (black dashed line) and a 3 fs electron pulse. (c) Direct sampling of the 5 fs laser field is evident when using a 1 fs electron pulse.

with atomic spatial resolution of electron diffraction. In addition, the simulations demonstrate the possibility of achieving attosecond temporal resolution with the characterization technique applied in this work, which is a crucial requirement for advancing the temporal resolution of UED into the few-femtosecond or attosecond regime.

8.6 Conclusions

The implementation of a UED experiment with few-femtosecond or attosecond temporal resolution requires combining a stable single-electron source [87] and the microwave compression technique presented in this work with the concepts for improving the temporal resolution discussed in this chapter. Despite the remaining challenges and requirements for a future UED beam line with sub-femtosecond stability and temporal resolution, all necessary technologies and improvements are either already available or plausible through simulations.

The results of this work as well as the concepts and methods presented here lay the groundwork for accessing the interesting new regime of electronic dynamics by attosecond electron diffraction, promising to elucidate some of the most fundamental physics of light-matter interaction.

Bibliography

[1] E. Muybridge. *Animals in Motion.* Dover Anatomy for Artists (Dover Publications, 1957).

[2] A. Velten, T. Willwacher, O. Gupta, A. Veeraraghavan, M. G. Bawendi, and R. Raskar. *Recovering three-dimensional shape around a corner using ultrafast time-of-flight imaging.* Nature Communications **3**, 745 (2012).

[3] J. S. Baskin and A. H. Zewail. *Freezing Atoms in Motion: Principles of Femtochemistry and Demonstration by Laser Stroboscopy.* Journal of Chemical Education **78**, 737 (2001).

[4] M. Chergui and A. H. Zewail. *Electron and X-Ray Methods of Ultrafast Structural Dynamics: Advances and Applications.* ChemPhysChem **10**, 28–43, and references therein (2009).

[5] P. Baum and A. H. Zewail. *4D attosecond imaging with free electrons: Diffraction methods and potential applications.* Chemical Physics **366**, 2–8 (2009).

[6] J. Kubelka, J. Hofrichter, and W. A. Eaton. *The protein folding 'speed limit'.* Current Opinion in Structural Biology **14**, 76–88 (2004).

[7] P. Baum, D.-S. Yang, and A. H. Zewail. *4D Visualization of Transitional Structures in Phase Transformations by Electron Diffraction.* Science **318**, 788–792 (2007).

[8] F. Carbone, P. Baum, P. Rudolf, and A. H. Zewail. *Structural Preablation Dynamics of Graphite Observed by Ultrafast Electron Crystallography.* Physical Review Letters **100**, 035501 (2008).

[9] S. Pandelov, B. M. Pilles, J. C. Werhahn, and H. Iglev. *Time-Resolved Dynamics of the OH Stretching Vibration in Aqueous NaCl Hydrate.* Journal of Physical Chemistry A **113**, 10184–10188 (2009).

[10] H. Iglev, M. K. Fischer, A. Gliserin, and A. Laubereau. *Ultrafast Geminate Recombination after Photodetachment of Aqueous Hydroxide.* Journal of the American Chemical Society **133**, 790–795 (2011).

[11] A. Rosspeintner, B. Lang, and E. Vauthey. *Ultrafast Photochemistry in Liquids.* Annual Review of Physical Chemistry **64**, 247–271 (2013).

[12] A. H. Zewail. *Chemistry at the Uncertainty Limit*. Angewandte Chemie, International Edition **40**, 4371–4375 (2001).

[13] M. Drescher, M. Hentschel, R. Kienberger, M. Uiberacker, V. Yakovlev, A. Scrinzi, T. Westerwalbesloh, U. Kleineberg, U. Heinzmann, and F. Krausz. *Time-resolved atomic inner-shell spectroscopy*. Nature **419**, 803–807 (2002).

[14] M. Uiberacker, T. Uphues, M. Schultze, A. J. Verhoef, V. Yakovlev, M. F. Kling, J. Rauschenberger, N. M. Kabachnik, H. Schröder, M. Lezius, K. L. Kompa, H. G. Muller, M. J. J. Vrakking, S. Hendel, U. Kleineberg, et al. *Attosecond real-time observation of electron tunnelling in atoms*. Nature **446**, 627–632 (2007).

[15] M. F. Kling, C. Siedschlag, A. J. Verhoef, J. I. Khan, M. Schultze, T. Uphues, Y. Ni, M. Uiberacker, M. Drescher, F. Krausz, and M. J. J. Vrakking. *Control of Electron Localization in Molecular Dissociation*. Science **312**, 246–248 (2006).

[16] A. Wirth, R. Santra, and E. Goulielmakis. *Real time tracing of valence-shell electronic coherences with attosecond transient absorption spectroscopy*. Chemical Physics **414**, 149–159 (2013).

[17] M. Krüger, M. Schenk, and P. Hommelhoff. *Attosecond control of electrons emitted from a nanoscale metal tip*. Nature **475**, 78–81 (2011).

[18] S. Zherebtsov, T. Fennel, J. Plenge, E. Antonsson, I. Znakovskaya, A. Wirth, O. Herrwerth, F. Süssmann, C. Peltz, I. Ahmad, S. A. Trushin, V. Pervak, S. Karsch, M. J. J. Vrakking, B. Langer, et al. *Controlled near-field enhanced electron acceleration from dielectric nanospheres with intense few-cycle laser fields*. Nature Physics **7**, 656–662 (2011).

[19] A. L. Cavalieri, N. Müller, T. Uphues, V. S. Yakovlev, A. Baltuška, B. Horvath, B. Schmidt, L. Blümel, R. Holzwarth, S. Hendel, M. Drescher, U. Kleineberg, P. M. Echenique, R. Kienberger, F. Krausz, et al. *Attosecond spectroscopy in condensed matter*. Nature **449**, 1029–1032 (2007).

[20] M. Schultze, M. Fiess, N. Karpowicz, J. Gagnon, M. Korbman, M. Hofstetter, S. Neppl, A. L. Cavalieri, Y. Komninos, T. Mercouris, C. A. Nicolaides, R. Pazourek, S. Nagele, J. Feist, J. Burgdörfer, et al. *Delay in Photoemission*. Science **328**, 1658–1662 (2010).

[21] F. Krausz and M. Ivanov. *Attosecond physics*. Review of Modern Physics **81**, 163–234 (2009).

[22] A. Shukla and N. Jain. *Dynamic damage growth in particle reinforced graded materials*. International Journal of Impact Engineering **30**, 777–803 (2004).

[23] P. Pupalaikis. *Teledyne LeCroy Successfully Demonstrates World's First 100 GHz Real-Time Oscilloscope*. Press release, Teledyne LeCroy, Inc. (2013).

[24] D. J. Bradley, B. Liddy, and W. E. Sleat. *Direct linear measurement of ultrashort light pulses with a picosecond streak camera*. Optics Communications **2**, 391–395 (1971).

[25] M. Y. SCHELEV, M. C. RICHARDSON, and A. J. ALCOCK. *Image-converter streak camera with picosecond resolution.* Applied Physics Letters **18**, 354–357 (1971).

[26] J. GAGNON. *Attosecond Electron Spectroscopy Theory and its Applications.* PhD thesis, Ludwig-Maximilians-Universität München (2010).

[27] M. T. HASSAN, A. WIRTH, I. GRGURAŠ, A. MOULET, T. T. LUU, J. GAGNON, V. PERVAK, and E. GOULIELMAKIS. *Invited Article: Attosecond photonics: Synthesis and control of light transients.* Review of Scientific Instruments **83**, 111301 (2012).

[28] L. E. HARGROVE, R. L. FORK, and M. A. POLLACK. *Locking of He-Ne Laser Modes Induced by Synchronous Intracavity Modulation.* Applied Physics Letters **5**, 4–5 (1964).

[29] D. E. SPENCE, P. N. KEAN, and W. SIBBETT. *60-fsec pulse generation from a self-mode-locked Ti:sapphire laser.* Optics Letters **16**, 42–44 (1991).

[30] T. GANZ, W. KOHLER, V. PERVAK, and P. BAUM. *Few-cycle high-energy pulse compression at MHz repetition rate.* In Proceedings of SPIE. Vol. 8240, 824400S. Edited by K. L. Vodopyanov. Nonlinear Frequency Generation and Conversion: Materials, Devices, and Applications XI (2012).

[31] E. GOULIELMAKIS, M. SCHULTZE, M. HOFSTETTER, V. S. YAKOVLEV, J. GAGNON, M. UIBERACKER, A. L. AQUILA, E. M. GULLIKSON, D. T. ATTWOOD, R. KIENBERGER, F. KRAUSZ, and U. KLEINEBERG. *Single-Cycle Nonlinear Optics.* Science **320**, 1614–1617 (2008).

[32] M. SCHULTZE, E. M. BOTHSCHAFTER, A. SOMMER, S. HOLZNER, W. SCHWEINBERGER, M. FIESS, M. HOFSTETTER, R. KIENBERGER, V. APALKOV, V. S. YAKOVLEV, M. I. STOCKMAN, and F. KRAUSZ. *Controlling dielectrics with the electric field of light.* Nature **493**, 75–78 (2013).

[33] K. ZHAO, Q. ZHANG, M. CHINI, Y. WU, X. WANG, and Z. CHANG. *Tailoring a 67 attosecond pulse through advantageous phase-mismatch.* Optics Letters **37**, 3891–3893 (2012).

[34] A. H. ZEWAIL. In *Les Prix Nobel: The Nobel Prices 1999.* Chapter: Femtochemistry: Atomic-scale dynamics of the chemical bond using ultrafast lasers, 110–203, and references therein. Edited by T. Frängsmyr (Almqvist & Wiksell, Stockholm, 2000).

[35] A. H. ZEWAIL. *Laser Femtochemistry.* Science **242**, 1645–1653 (1988).

[36] A. H. ZEWAIL. *Femtochemistry.* Journal of Physical Chemistry **97**, 12427–12446 (1993).

[37] P. BAUM and A. H. ZEWAIL. *Attosecond electron pulses for 4D diffraction and microscopy.* Proceedings of the National Academy of Sciences of the United States of America **104**, 18409–18414 (2007).

[38] A. H. ZEWAIL. *Four-Dimensional Electron Microscopy.* Science **328**, 187–193 (2010).

[39] R. LAENEN, T. ROTH, and A. LAUBEREAU. *Novel Precursors of Solvated Electrons in Water: Evidence for a Charge Transfer Process.* Physical Review Letters **85**, 50–53 (2000).

[40] R. SRINIVASAN, J. S. FEENSTRA, S. T. PARK, S. XU, and A. H. ZEWAIL. *Dark Structures in Molecular Radiationless Transitions Determined by Ultrafast Diffraction.* Science **307**, 558–563 (2005).

[41] G. BINNIG and H. ROHRER. *Scanning tunneling microscopy.* IBM Journal of Research and Development **30**, 355–369 (1986).

[42] G. BINNIG and H. ROHRER. In *Nobel Lectures in Physics 1981-1990.* Chapter: Scanning Tunneling Microscopy – From Birth to Adolescence. Edited by G. Ekspong (World Scientific Publishing Co., 1991).

[43] W. L. BRAGG. *The Structure of Some Crystals as Indicated by Their Diffraction of X-rays.* Proceedings of the Royal Society of London. Series A, Containing Papers of a Mathematical and Physical Character **89**, 248–277 (1913).

[44] S. KLINGE, F. VOIGTS-HOFFMANN, M. LEIBUNDGUT, S. ARPAGAUS, and N. BAN. *Crystal Structure of the Eukaryotic 60S Ribosomal Subunit in Complex with Initiation Factor 6.* Science **334**, 941–948 (2011).

[45] L. A. BENDERSKY and F. W. GAYLE. *Electron Diffraction Using Transmission Electron Microscopy.* Journal of Research of the National Institute of Standards and Technology **106**, 997–1012 (2001).

[46] P. M. B. PICCOLI, T. F. KOETZLE, and A. J. SCHULTZ. *Single Crystal Neutron Diffraction for the Inorganic Chemist – A Practical Guide.* Comments on Inorganic Chemistry: A Journal of Critical Discussion of the Current Literature **28**, 3–38 (2007).

[47] R. ERNI, M. D. ROSSELL, C. KISIELOWSKI, and U. DAHMEN. *Atomic-Resolution Imaging with a Sub-50-pm Electron Probe.* Physical Review Letters **102**, 096101 (2009).

[48] E. RUSKA. In *Nobel Lectures in Physics 1981-1990.* Chapter: The Development of the Electron Microscope and of Electron Microscopy. Edited by G. Ekspong (World Scientific Publishing Co., 1991).

[49] D. J. FLANNIGAN and A. H. ZEWAIL. *4D Electron Microscopy: Principles and Applications.* Accounts of Chemical Research **45**, 1828–1839 (2012).

[50] A. A. ZHOLENTS and M. S. ZOLOTOREV. *Femtosecond X-Ray Pulses of Synchrotron Radiation.* Physical Review Letters **76**, 912–915 (1996).

[51] R. W. SCHOENLEIN, W. P. LEEMANS, A. H. CHIN, P. VOLFBEYN, T. E. GLOVER, P. BALLING, M. ZOLOTOREV, K.-J. KIM, S. CHATTOPADHYAY, and C. V. SHANK. *Femtosecond X-ray Pulses at 0.4 Å Generated by 90° Thomson Scattering: A Tool for Probing the Structural Dynamics of Materials.* Science **274**, 236–238 (1996).

[52] R. H. MILBURN. *Electron Scattering by an Intense Polarized Photon Field.* Physical Review Letters **10**, 75–77 (1963).

[53] W. ACKERMANN, G. ASOVA, V. AYVAZYAN, A. AZIMA, N. BABOI, J. BÄHR, V. BALANDIN, B. BEUTNER, A. BRANDT, A. BOLZMANN, R. BRINKMANN, O. I. BROVKO, M. CASTELLANO, P. CASTRO, L. CATANI, et al. *Operation of a free-electron laser from the extreme ultraviolet to the water window.* Nature Photonics **1**, 336–342 (2007).

[54] H. N. Chapman, P. Fromme, A. Barty, T. A. White, R. A. Kirian, A. Aquila, M. S. Hunter, J. Schulz, D. P. DePonte, U. Weierstall, R. B. Doak, F. R. N. C. Maia, A. V. Martin, I. Schlichting, L. Lomb, et al. *Femtosecond X-ray protein nanocrystallography*. Nature **470**, 73–77 (2011).

[55] A. Barty, C. Caleman, A. Aquila, N. Timneanu, L. Lomb, T. A. White, J. Andreasson, D. Arnlund, S. Bajt, T. R. M. Barends, M. Barthelmess, M. J. Bogan, C. Bostedt, J. D. Bozek, R. Coffee, et al. *Self-terminating diffraction gates femtosecond X-ray nanocrystallography measurements*. Nature Photonics **6**, 35–40 (2012).

[56] C. Bostedt, J. D. Bozek, P. H. Bucksbaum, R. N. Coffee, J. B. Hastings, Z. Huang, R. W. Lee, S. Schorb, J. N. Corlett, P. Denes, P. Emma, R. W. Falcone, R. W. Schoenlein, G. Doumy, E. P. Kanter, et al. *Ultra-fast and ultra-intense x-ray sciences: first results from the Linac Coherent Light Source free-electron laser*. Journal of Physics B: Atomic, Molecular and Optical Physics **46**, 164003 (2013).

[57] C. Bressler. *Conceptual Design Report: Scientific Instrument FXE*. XFEL.EU TR-2011-005, European X-Ray Free-Electron Laser Facility GmbH (2011).

[58] T. Ishikawa, H. Aoyagi, T. Asaka, Y. Asano, N. Azumi, T. Bizen, H. Ego, K. Fukami, T. Fukui, Y. Furukawa, S. Goto, H. Hanaki, T. Hara, T. Hasegawa, T. Hatsui, et al. *A compact X-ray free-electron laser emitting in the sub-ångström region*. Nature Photonics **6**, 540–544 (2012).

[59] K. Nakajima. *Compact X-ray sources: Towards a table-top free-electron laser*. Nature Physics **4**, 92–93 (2008).

[60] A. M. Kondratenko and E. L. Saldin. *Generation of coherent radiation by a relativistic electron beam in an ondulator*. Particle Accelerators **10**, 207–219 (1980).

[61] J. Amann, W. Berg, V. Blank, F.-J. Decker, Y. Ding, P. Emma, Y. Feng, J. Frisch, D. Fritz, J. Hastings, Z. Huang, J. Krzywinski, R. Lindberg, H. Loos, A. Lutman, et al. *Demonstration of self-seeding in a hard-X-ray free-electron laser*. Nature Photonics **6**, 693–698 (2012).

[62] T. Tanaka. *Proposal for a Pulse-Compression Scheme in X-Ray Free-Electron Lasers to Generate a Multiterawatt, Attosecond X-Ray Pulse*. Physical Review Letters **110**, 084801 (2013).

[63] D. Kim, H. Lee, S. Chung, and K. Lee. *Attosecond keV x-ray pulses driven by Thomson scattering in a tight focus regime*. New Journal of Physics **11**, 063050 (2009).

[64] M. Fuchs, R. Weingartner, A. Popp, Z. Major, S. Becker, J. Osterhoff, I. Cortrie, B. Zeitler, R. Hörlein, G. D. Tsakiris, U. Schramm, T. P. Rowlands-Rees, S. M. Hooker, D. Habs, F. Krausz, et al. *Laser-driven soft-X-ray undulator source*. Nature Physics **5**, 826–829 (2009).

[65] A. Buck, M. Nicolai, K. Schmid, C. M. S. Sears, A. Sävert, J. M. Mikhailova, F. Krausz, M. C. Kaluza, and L. Veisz. *Real-time observation of laser-driven electron acceleration*. Nature Physics **7**, 543–548 (2011).

[66] F. GRÜNER, S. BECKER, U. SCHRAMM, T. EICHNER, M. FUCHS, R. WEINGARTNER, D. HABS, J. MEYER-TER-VEHN, M. GEISSLER, M. FERRARIO, L. SERAFINI, B. van der GEER, H. BACKE, W. LAUTH, and S. REICHE. *Design considerations for table-top, laser-based VUV and X-ray free electron lasers.* Applied Physics B: Lasers and Optics **86**, 431–435 (2007).

[67] A. R. MAIER, A. MESECK, S. REICHE, C. B. SCHROEDER, T. SEGGEBROCK, and F. GRÜNER. *Demonstration Scheme for a Laser-Plasma-Driven Free-Electron Laser.* Physical Review X **2**, 031019 (2012).

[68] J. C. WILLIAMSON, M. DANTUS, S. B. KIM, and A. H. ZEWAIL. *Ultrafast diffraction and molecular structure.* Chemical Physics Letters **196**, 529–534 (1992).

[69] J. C. WILLIAMSON and A. H. ZEWAIL. *Ultrafast electron diffraction. Velocity mismatch and temporal resolution in crossed-beam experiments.* Chemical Physics Letters **209**, 10–16 (1993).

[70] T. van OUDHEUSDEN, P. L. E. M. PASMANS, S. B. van der GEER, M. J. de LOOS, M. J. van der WIEL, and O. J. LUITEN. *Compression of Subrelativistic Space-Charge-Dominated Electron Bunches for Single-Shot Femtosecond Electron Diffraction.* Physical Review Letters **105**, 264801 (2010).

[71] Y. MUROOKA, N. NARUSE, S. SAKAKIHARA, M. ISHIMARU, J. YANG, and K. TANIMURA. *Transmission-electron diffraction by MeV electron pulses.* Applied Physics Letters **98**, 251903 (2011).

[72] A. TAKAOKA, K. URA, H. MORI, T. KATSUTA, I. MATSUI, and S. HAYASHI. *Development of a new 3 MV ultra-high voltage electron microscope at Osaka University.* Journal of Electron Microscopy **46**, 447–456 (1997).

[73] P. KIRKPATRICK and A. V. BAETZ. *Formation of Optical Images by X-Rays.* Journal of the Optical Society of America **38**, 766–773 (1948).

[74] J. ASHLEY, C. TUNG, and R. RITCHIE. *Electron inelastic mean free paths and energy losses in solids: I. Aluminum metal.* Surface Science **81**, 409–426 (1979).

[75] D. LILJEQUIST. *A simple calculation of inelastic mean free path and stopping power for 50 eV-50 keV electrons in solids.* Journal of Physics D: Applied Physics **16**, 1567–1582 (1983).

[76] T. van OUDHEUSDEN, E. F. de JONG, S. B. van der GEER, W. P. E. M. op 'T ROOT, O. J. LUITEN, and B. J. SIWICK. *Electron source concept for single-shot sub-100 fs electron diffraction in the 100 keV range.* Journal of Applied Physics **102**, 093501 (2007).

[77] P. L. E. M. PASMANS, G. B. van den HAM, S. F. P. DAL CONTE, S. B. van der GEER, and O. J. LUITEN. *Microwave TM_{010} cavities as versatile 4D electron optical elements.* Ultramicroscopy **127**, 19–24 (2013).

[78] G. SCIAINI and R. J. DWAYNE MILLER. *Femtosecond electron diffraction: heralding the era of atomically resolved dynamics.* Reports on Progress in Physics **75**, 096101 (2011).

[79] E. FILL, L. VEISZ, A. APOLONSKI, and F. KRAUSZ. *Sub-fs electron pulses for ultrafast electron diffraction.* New Journal of Physics **8**, 272 (2006).

[80] L. Veisz, G. Kurkin, K. Chernov, V. Tarnetsky, A. Apolonski, F. Krausz, and E. Fill. *Hybrid dc–ac electron gun for fs-electron pulse generation.* New Journal of Physics **9**, 451 (2007).

[81] A. Gliserin, A. Apolonski, F. Krausz, and P. Baum. *Compression of single-electron pulses with a microwave cavity.* New Journal of Physics **14**, 073055 (2012).

[82] M. Aidelsburger, F. O. Kirchner, F. Krausz, and P. Baum. *Single-electron pulses for ultrafast diffraction.* Proceedings of the National Academy of Sciences of the United States of America **107**, 19714–19719 (2010).

[83] W. J. Engelen, M. A. van der Heijden, D. J. Bakker, E. J. D. Vredenbregt, and O. J. Luiten. *High-coherence electron bunches produced by femtosecond photoionization.* Nature Communications **4**, 1693 (2013).

[84] W. J. Engelen, E. P. Smakman, D. J. Bakker, O. J. Luiten, and E. J. D. Vredenbregt. *Effective temperature of an ultracold electron source based on near-threshold photoionization.* Ultramicroscopy **136**, 73–80 (2014).

[85] P. Baum. *On the physics of ultrashort single-electron pulses for time-resolved microscopy and diffraction.* Chemical Physics **423**, 55–61 (2013).

[86] F. O. Kirchner, S. Lahme, F. Krausz, and P. Baum. *Coherence of femtosecond single electrons exceeds biomolecular dimensions.* New Journal of Physics **15**, 063021 (2013).

[87] F. O. Kirchner. *Ultrashort and coherent single-electron pulses for diffraction at ultimate resolutions.* PhD thesis, Ludwig-Maximilians-Universität München (2013).

[88] F. Reiter, U. Graf, M. Schultze, W. Schweinberger, H. Schröder, N. Karpowicz, A. M. Azzeer, R. Kienberger, F. Krausz, and E. Goulielmakis. *Generation of sub-3 fs pulses in the deep ultraviolet.* Optics Letters **35**, 2248–2250 (2010).

[89] S. Düsterer, P. Radcliffe, C. Bostedt, J. Bozek, A. L. Cavalieri, R. Coffee, J. T. Costello, D. Cubaynes, L. F. DiMauro, Y. Ding, G. Doumy, F. Grüner, W. Helml, W. Schweinberger, R. Kienberger, et al. *Femtosecond x-ray pulse length characterization at the Linac Coherent Light Source free-electron laser.* New Journal of Physics **13**, 093024 (2011).

[90] T. Tschentscher. *Layout of the X-Ray Systems at the European XFEL.* XFEL.EU TR-2011-001, European X-Ray Free-Electron Laser Facility GmbH (2011).

[91] P. Hansen, C. Baumgarten, H. Batelaan, and M. Centurion. *Dispersion compensation for attosecond electron pulses.* Applied Physics Letters **101**, 083501 (2012).

[92] G. F. Mancini, B. Mansart, S. Pagano, B. van der Geer, M. de Loos, and F. Carbone. *Design and implementation of a flexible beamline for fs electron diffraction experiments.* Nuclear Instruments and Methods in Physics Research, Section A: Accelerators, Spectrometers, Detectors, and Associated Equipment **691**, 113–122 (2012).

[93] F. O. Kirchner, A. Gliserin, F. Krausz, and P. Baum. *Laser streaking of free electrons at 25 keV.* Nature Photonics **8**, 52–57 (2014).

[94] A. LASSISE, P. H. A. MUTSAERS, and O. J. LUITEN. *Compact, low power radio frequency cavity for femtosecond electron microscopy.* Review of Scientific Instruments **83**, 043705 (2012).

[95] Z.-H. HE, A. G. R. THOMAS, B. BEAUREPAIRE, J. A. NEES, B. HOU, V. MALKA, K. KRUSHELNICK, and J. FAURE. *Electron diffraction using ultrafast electron bunches from a laser-wakefield accelerator at kHz repetition rate.* Applied Physics Letters **102**, 064104 (2013).

[96] M. GAO, H. JEAN-RUEL, R. R. COONEY, J. STAMPE, M. de JONG, M. HARB, G. SCIAINI, G. MORIENA, and R. J. DWAYNE MILLER. *Full characterization of RF compressed femtosecond electron pulses using ponderomotive scattering.* Optics Express **20**, 12048–12058 (2012).

[97] S. T. PARK, A. YURTSEVER, J. S. BASKIN, and A. H. ZEWAIL. *Graphene-layered steps and their fields visualized by 4D electron microscopy.* Proceedings of the National Academy of Sciences of the United States of America **110**, 9277–9282 (2013).

[98] D. J. FLANNIGAN, B. BARWICK, and A. H. ZEWAIL. *Biological imaging with 4D ultrafast electron microscopy.* Proceedings of the National Academy of Sciences of the United States of America **107**, 9933–9937 (2010).

[99] X. JIANG, C. N. BERGLUND, A. E. BELL, and W. A. MACKIE. *OS3: Photoemission from gold thin films for application in multiphotocathode arrays for electron beam lithography.* Journal of Vacuum Science and Technology B **16**, 3374–3379 (1998).

[100] D. WYTRYKUS, M. CENTURION, P. RECKENTHAELER, F. KRAUSZ, A. APOLONSKI, and E. FILL. *Ultrashort pulse electron gun with a MHz repetition rate.* Applied Physics B: Lasers and Optics **96**, 309–314 (2009).

[101] K. ABRAHAMYAN, J. BÄHR, I. BOHNET, M. KRASSILNIKOV, D. LIPKA, V. MILTCHEV, A. OPPELT, F. STEPHAN, K. FLÖTTMANN, and I. TSAKOV. *Transverse Emittance Measurement at the Photo Injector Test Facility at DESY Zeuthen (PITZ).* In Proceedings DIPAC, (2003).

[102] P. HOMMELHOFF, C. KEALHOFER, A. AGHAJANI-TALESH, Y. R. P. SORTAIS, S. M. FOREMAN, and M. A. KASEVICH. *Extreme localization of electrons in space and time.* Ultramicroscopy **109**, 423–429 (2009).

[103] J.-P. STEIN. *Tip-based electron source for femtosecond electron diffraction.* Diploma thesis, Technische Universität München (2011).

[104] B. CHO, T. ICHIMURA, R. SHIMIZU, and C. OSHIMA. *Quantitative Evaluation of Spatial Coherence of the Electron Beam from Low Temperature Field Emitters.* Physical Review Letters **94**, 246103 (2004).

[105] C. WENINGER and P. BAUM. *Temporal distortions in magnetic lenses.* Ultramicroscopy **113**, 145–151 (2012).

[106] S. HUMPHRIES, Jr. *Principles of Charged Particle Acceleration.* Dover Books on Physics (Dover Publications, 2012).

[107] R. A. JAMESON. In *High-Brightness Accelerators.* NATO ASI Series. Vol. 178, Chapter: RF Breakdown Limits, pp. 497–506. Edited by A. K. Hyder, M. F. Rose, and A. H. Guenther. Vol. 178 (Plenum Press, New York, 1988).

[108] S. Tokita, M. Hashida, S. Inoue, T. Nishoji, K. Otani, and S. Sakabe. *Single-Shot Femtosecond Electron Diffraction with Laser-Accelerated Electrons: Experimental Demonstration of Electron Pulse Compression*. Physical Review Letters **105**, 215004 (2010).

[109] G. H. Kassier, K. Haupt, N. Erasmus, E. G. Rohwer, and H. Schwoerer. *Achromatic reflectron compressor design for bright pulses in femtosecond electron diffraction*. Journal of Applied Physics **105**, 113111 (2009).

[110] Y. Wang and N. Gedik. *Electron Pulse Compression With a Practical Reflectron Design for Ultrafast Electron Diffraction*. IEEE Journal of Selected Topics in Quantum Electronics **18**, 140–147 (2012).

[111] P. Baum and A. H. Zewail. *Breaking resolution limits in ultrafast electron diffraction and microscopy*. Proceedings of the National Academy of Sciences of the United States of America **103**, 16105–16110 (2006).

[112] D. Kreier and P. Baum. *Avoiding temporal distortions in tilted pulses*. Optics Letters **37**, 2373–2375 (2012).

[113] S. Lahme. *Private communication*. A long-term decay of the photoemission yield is observed in our laboratory. It can be possibly attributed to contamination of the photocathode with organic substances, which reduces the work function, and subsequent partial removal of the contamination by the impinging laser. However, different or additional causes for the observed effect cannot be excluded.

[114] A. Gahlmann, S. T. Park, and A. H. Zewail. *Ultrashort electron pulses for diffraction, crystallography and microscopy: theoretical and experimental resolutions*. Physical Chemistry Chemical Physics **10**, 2894–2909 (2008).

[115] H. Monjushiro, I. Watanabe, and Y. Yokoyama. *Ultraviolet Photoelectron Yield Spectra of Thin Gold Films Measured in Air*. Analytical Sciences **7**, 543–547 (1991).

[116] W. E. Spicer. *Optical Transitions in Which Crystal Momentum is Not Conserved*. Physical Review Letters **11**, 243–245 (1963).

[117] W. E. Spicer. *Possible Non-One-Electron Effects in the Fundamental Optical Excitation Spectra of Certain Crystalline Solids and Their Effect on Photoemission*. Physical Review **154**, 385–394 (1967).

[118] D. H. Dowell and J. F. Schmerge. *Quantum efficiency and thermal emittance of metal photocathodes*. Physical Review Special Topics – Accelerators and Beams **12**, 074201 (2009).

[119] M. Born and E. Wolf. *Principles of Optics* (Cambridge University Press, 1999).

[120] R. L. Fork, O. E. Martinez, and J. P. Gordon. *Negative dispersion using pairs of prisms*. Optics Letters **9**, 150–152 (1984).

[121] O. E. Martinez, J. P. Gordon, and R. L. Fork. *Negative group-velocity dispersion using refraction*. Journal of the Optical Society of America A: Optics, Image Science & Vision **1**, 1003–1006 (1984).

[122] R. Szipöcs, K. Ferencz, C. Spielmann, and F. Krausz. *Chirped multilayer coatings for broadband dispersion control in femtosecond lasers*. Optics Letters **19**, 201–203 (1994).

[123] T. P. WANGLER. *RF Linear Accelerators* (Wiley-VCH, 2008).

[124] T. van OUDHEUSDEN. *Electron source for sub-relativistic single-shot femtosecond diffraction*. PhD thesis, Technische Universiteit Eindhoven (2010).

[125] E. A. KNAPP, B. C. KNAPP, and J. M. POTTER. *Standing Wave High Energy Linear Accelerator Structures*. Review of Scientific Instruments **39**, 979–991 (1968).

[126] F. B. KIEWIET. *Ultra-short high-brightness electron bunches from an RF photo-injector*. PhD thesis, Technische Universiteit Eindhoven (2003).

[127] A. AGARWAL and J. H. LANG. *Foundations of Analog and Digital Electronic Circuits* (Morgan Kaufmann, 2005).

[128] J. ARTHUR, P. ANFINRUD, P. AUDEBERT, K. BANE, I. BEN-ZVI, V. BHARADWAJ, R. BIONTA, P. BOLTON, M. BORLAND, P. H. BUCKSBAUM, R. C. CAUBLE, J. CLENDENIN, M. CORNACCHIA, G. DECKER, P. D. HARTOG, et al. *Linac Coherent Light Source (LCLS) Conceptual Design Report*. SLAC-R-593, UC-414, Stanford Linear Accelerator Center, Stanford University (2002).

[129] M. ALTARELLI, R. BRINKMANN, M. CHERGUI, W. DECKING, B. DOBSON, S. DÜSTERER, G. GRÜBEL, W. GRAEFF, H. GRAAFSMA, J. HAJDU, J. MARANGOS, J. PFLÜGER, H. REDLIN, D. RILEY, I. ROBINSON, et al. *The European X-Ray Free-Electron Laser, technical design report*. DESY 2006-097, DESY XFEL Project Group (2007).

[130] C. J. BOCCHETTA, A. ABRAMI, E. ALLARIA, I. ANDRIAN, D. BACESCU, L. BADANO, L. BANCHI, D. BULFONE, C. BONTOIU, R. BRACCO, F. CARGNELLO, K. CASARIN, M. CORNACCHIA, P. CRAIEVICH, D. COCCO, et al. *FERMI@Elettra, Conceptual Design Report*. ST/F-TN-07/12, Sincrotrone Trieste (2007).

[131] T. UDEM, R. HOLZWARTH, and T. W. HÄNSCH. *Optical frequency metrology*. Nature **416**, 233–237, and references therein (2002).

[132] A. BARTELS, S. A. DIDDAMS, C. W. OATES, G. WILPERS, J. C. BERGQUIST, W. H. OSKAY, and L. HOLLBERG. *Femtosecond-laser-based synthesis of ultrastable microwave signals from optical frequency references*. Optics Letters **30**, 667–669 (2005).

[133] J. KIM, J. A. COX, J. CHEN, and F. X. KÄRTNER. *Drift-free femtosecond timing synchronization of remote optical and microwave sources*. Nature Photonics **2**, 733–736 (2008).

[134] J. KIM and F. X. KÄRTNER. *Attosecond-precision ultrafast photonics*. Laser & Photonics Reviews **4**, 432–456 (2009).

[135] A. J. BENEDICK, J. G. FUJIMOTO, and F. X. KÄRTNER. *Optical flywheels with attosecond jitter*. Nature Photonics **6**, 97–100 (2011).

[136] J. KIM and F. X. KÄRTNER. *Microwave signal extraction from femtosecond mode-locked lasers with attosecond relative timing drift*. Optics Letters **35**, 2022–2024 (2010).

[137] K. JUNG and J. KIM. *Subfemtosecond synchronization of microwave oscillators with mode-locked Er-fiber lasers*. Optics Letters **37**, 2958–2960 (2012).

[138] W. Zhang, Z. Xu, M. Lours, R. Boudot, Y. Kersalé, G. Santarelli, and Y. Le Coq. *Sub-100 attoseconds stability optics-to-microwave synchronization.* Applied Physics Letters **96**, 211105 (2010).

[139] T. M. Fortier, M. S. Kirchner, F. Quinlan, J. Taylor, J. C. Bergquist, T. Rosenband, N. Lemke, A. Ludlow, Y. Jiang, C. W. Oates, and S. A. Diddams. *Generation of ultrastable microwaves via optical frequency division.* Nature Photonics **5**, 425–429 (2011).

[140] S. A. Diddams, M. Kirchner, T. M. Fortier, D. Braje, A. M. Weiner, and L. Hollberg. *Improved signal-to-noise ratio of 10 GHz microwave signals generated with a mode-filtered femtosecond laser frequency comb.* Optics Express **17**, 3331–3340 (2009).

[141] H. Jiang, J. Taylor, F. Quinlan, T. M. Fortier, and S. A. Diddams. *Noise Floor Reduction of an Er:Fiber Laser-Based Photonic Microwave Generator.* IEEE Photonics Journal **3**, 1004–1012 (2011).

[142] A. Gliserin, M. Walbran, and P. Baum. *Passive optical enhancement of laser-microwave synchronization.* Applied Physics Letters **103**, 031113 (2013).

[143] R. Sabella and S. Merli. *Analysis of InGaAs P-I-N Photodiode Frequency Response.* IEEE Journal of Quantum Electronics **29**, 906–916 (1993).

[144] Z. Li, H. Pan, H. Chen, A. Beling, and J. C. Campbell. *High-Saturation-Current Modified Uni-Traveling-Carrier Photodiode With Cliff Layer.* IEEE Journal of Quantum Electronics **46**, 626–632 (2010).

[145] J. Taylor, S. Datta, A. Hati, C. Nelson, F. Quinlan, A. Joshi, and S. A. Diddams. *Characterization of Power-to-Phase Conversion in High-Speed P-I-N Photodiodes.* IEEE Photonics Journal **3**, 140–151 (2011).

[146] W. Zhang, T. Li, M. Lours, S. Seidelin, G. Santarelli, and Y. Le Coq. *Amplitude to phase conversion of InGaAs pin photo-diodes for femtosecond lasers microwave signal generation.* Applied Physics B: Lasers and Optics **106**, 301–308 (2012).

[147] F. Quinlan, T. M. Fortier, H. Jiang, A. Hati, C. Nelson, Y. Fu, J. C. Campbell, and S. A. Diddams. *Exploiting shot noise correlations in the photodetection of ultrashort optical pulse trains.* Nature Photonics **7**, 290–293 (2013).

[148] J. B. Johnson. *Thermal Agitation of Electricity in Conductors.* Physical Review **32**, 97–109 (1928).

[149] H. Nyquist. *Thermal Agitation of Electric Charge in Conductors.* Physical Review **32**, 110–113 (1928).

[150] I. Zamek and S. Zamek. *Definitions of jitter measurement terms and relationships.* In Proceedings of IEEE International Test Conference (ITC 2005), 25–34 (2005).

[151] J. R. Vig, E. S. Ferre-Pikal, J. C. Camparo, L. S. Cutler, L. Maleki, W. J. Riley, S. R. Stein, C. Thomas, F. L. Walls, and J. D. White. *IEEE Standard Definitions of Physical Quantities for Fundamental Frequency and Time Metrology – Random Instabilities.* IEEE Std. 1139-1999, IEEE Power & Energy Society (1999).

[152] A. Hajimiri and T. H. Lee. *A General Theory of Phase Noise in Electrical Oscillators*. IEEE Journal of Solid-State Circuits **33**, 179–194 (1998).

[153] A. Hati, D. A. Howe, F. L. Walls, and D. K. Walker. *Merits of PM noise measurement over noise figure: A study at microwave frequencies*. IEEE Transactions on Ultrasonics, Ferroelectrics and Frequency Control **53**, 1889–1894 (2006).

[154] Z. Li, Y. Fu, M. Piels, H. Pan, A. Beling, J. E. Bowers, and J. C. Campbell. *High-power high-linearity flip-chip bonded modified uni-traveling carrier photodiode*. Optics Express **19**, B385–B390 (2011).

[155] K. J. Williams, R. D. Esman, and M. Dagenais. *Effects of High Space-Charge Fields on the Response of Microwave Photodetectors*. IEEE Photonics Technology Letters **6**, 639–641 (1994).

[156] M. S. Kirchner, D. A. Braje, T. M. Fortier, A. M. Weiner, L. Hollberg, and S. A. Diddams. *Generation of 20 GHz, sub-40 fs pulses at 960 nm via repetition-rate multiplication*. Optics Letters **34**, 872–874 (2009).

[157] J. Chen, J. W. Sickler, P. Fendel, E. P. Ippen, F. X. Kärtner, T. Wilken, R. Holzwarth, and T. W. Hänsch. *Generation of low-timing-jitter femtosecond pulse trains with 2 GHz repetition rate via external repetition rate multiplication*. Optics Letters **33**, 959–961 (2008).

[158] T. Steinmetz, T. Wilken, C. Araujo-Hauck, R. Holzwarth, T. W. Hänsch, and T. Udem. *Fabry–Pérot filter cavities for wide-spaced frequency combs with large spectral bandwidth*. Applied Physics B: Lasers and Optics **96**, 251–256 (2009).

[159] A. Haboucha, W. Zhang, T. Li, M. Lours, A. N. Luiten, Y. Le Coq, and G. Santarelli. *Optical-fiber pulse rate multiplier for ultralow phase-noise signal generation*. Optics Letters **36**, 3654–3656 (2011).

[160] S. Naumov, A. Fernandez, R. Graf, P. Dombi, F. Krausz, and A. Apolonski. *Approaching the microjoule frontier with femtosecond laser oscillators*. New Journal of Physics **7**, 216 (2005).

[161] B. C. Young, F. C. Cruz, W. M. Itano, and J. C. Bergquist. *Visible Lasers with Subhertz Linewidths*. Physical Review Letters **82**, 3799–3802 (1999).

[162] K. Czuba and D. Sikora. *Temperature Stability of Coaxial Cables*. Acta Physica Polonica, A **119**, 553–557 (2011).

[163] G. J. H. Brussaard, A. Lassise, P. L. E. M. Pasmans, P. H. A. Mutsaers, M. J. van der Wiel, and O. J. Luiten. *Direct measurement of synchronization between femtosecond laser pulses and a 3 GHz radio frequency electric field inside a resonant cavity*. Applied Physics Letters **103**, 141105 (2013).

[164] W. Wien. *Untersuchungen über die elektrische Entladung in verdünnten Gasen*. Annalen der Physik **313**, 244–266 (1902).

[165] G. H. Curtis and J. Silcox. *A Wien Filter for Use as an Energy Analyzer with an Electron Microscope*. Review of Scientific Instruments **42**, 630–637 (1971).

[166] K. Jensen and E. Veje. *Construction of a wien filter heavy ion accelerator*. Nuclear Instruments and Methods **122**, 511–515 (1974).

[167] F. B. Kiewiet, A. H. Kemper, O. J. Luiten, G. J. H. Brussaard, and M. J. van der Wiel. *Femtosecond synchronization of a 3 GHz RF oscillator to a mode-locked Ti:sapphire laser*. Nuclear Instruments and Methods in Physics Research, Section A: Accelerators, Spectrometers, Detectors, and Associated Equipment **484**, 619–624 (2002).

[168] J. Lin, N. Weber, A. Wirth, S. H. Chew, M. Escher, M. Merkel, M. F. Kling, M. I. Stockman, F. Krausz, and U. Kleineberg. *Time of flight-photoemission electron microscope for ultrahigh spatiotemporal probing of nanoplasmonic optical fields*. Journal of Physics: Condensed Matter **21**, 314005 (2009).

[169] G. H. Kassier, K. Haupt, N. Erasmus, E. G. Rohwer, H. M. von Bergmann, H. Schwoerer, S. M. M. Coelho, and F. D. Auret. *A compact streak camera for 150 fs time resolved measurement of bright pulses in ultrafast electron diffraction*. Review of Scientific Instruments **81**, 105103 (2010).

[170] M. Gao, Y. Jiang, G. H. Kassier, and R. J. Dwayne Miller. *Single shot time stamping of ultrabright radio frequency compressed electron pulses*. Applied Physics Letters **103**, 033503 (2013).

[171] C. T. Hebeisen, R. Ernstorfer, M. Harb, T. Dartigalongue, R. E. Jordan, and R. J. Dwayne Miller. *Femtosecond electron pulse characterization using laser ponderomotive scattering*. Optics Letters **31**, 3517–3519 (2006).

[172] F. Carbone, B. Barwick, O.-H. Kwon, H. S. Park, J. S. Baskin, and A. H. Zewail. *EELS femtosecond resolved in 4D ultrafast electron microscopy*. Chemical Physics Letters **468**, 107–111 (2009).

[173] F. Carbone, O.-H. Kwon, and A. H. Zewail. *Dynamics of Chemical Bonding Mapped by Energy-Resolved 4D Electron Microscopy*. Science **325**, 181–184 (2009).

[174] B. Barwick, D. J. Flannigan, and A. H. Zewail. *Photon-induced near-field electron microscopy*. Nature **462**, 902–906 (2009).

[175] S. T. Park, M. Lin, and A. H. Zewail. *Photon-induced near-field electron microscopy (PINEM): theoretical and experimental*. New Journal of Physics **12**, 123028 (2010).

[176] A. D. Rakić. *Algorithm for the determination of intrinsic optical constants of metal films: application to aluminum*. Applied Optics **34**, 4755–4767 (1995).

[177] P. Reckenthaeler, M. Centurion, V. S. Yakovlev, M. Lezius, F. Krausz, and E. Fill. *Proposed method for measuring the duration of electron pulses by attosecond streaking*. Physical Review A: Atomic, Molecular, and Optical Physics **77**, 042902 (2008).

[178] R. F. Egerton. *Electron Energy-Loss Spectroscopy in the Electron Microscope* (Springer, 2011).

[179] J. Stingl, F. Zamponi, B. Freyer, M. Woerner, T. Elsaesser, and A. Borgschulte. *Electron Transfer in a Virtual Quantum State of $LiBH_4$ Induced by Strong Optical Fields and Mapped by Femtosecond X-Ray Diffraction*. Physical Review Letters **109**, 147402 (2012).

Data archiving

The experimental raw data, evaluation files, and original figures can be found on the Data Archive Server of the Laboratory for Attosecond Physics at the Max Planck Institute of Quantum Optics: `/afs/rzg/mpq/lap/publication_archive`

The source data of all figures is organized relative to the root folder of the data archive for the thesis within subfolders inside the `/figures` directory, using the same figure numbers as in the thesis. A text file within each figure's folder named `fig_X.X.txt` (`X.X` being the figure's number) gives detailed information about the organization and format of the raw data, as well as the processing performed in order to obtain the final figure. Further experimental and simulation details are given where applicable, in addition to the main text.

Acknowledgments

At this point, I would like to express my special gratitude to the numerous people who contributed to this work with advice, assistance, and support. First of all, I thank Prof. Ferenc Krausz for giving me the opportunity to carry out my doctoral project in his extraordinary research group. The broad and interdisciplinary spectrum of research as well as the international atmosphere made my stay in this group a unique and valuable experience, both scientifically and personally. I would also like to thank Prof. Eberhard Riedle for kindly offering to review my thesis.

I cordially thank my supervisor Peter Baum for guiding and supporting me throughout my project and for valuable advice on the manuscript. Your continuous interest in my work, your patient and calm way of discussing problems as well as your remarkably honest and professional approach to science and (especially our own) research kept me constantly motivated. I could greatly benefit and learn from your broad scientific knowledge, experience, and advice. Most of all, I am grateful for the freedom you granted me in my research, be it concerning the direction of the project, the implementation in the laboratory, the funding, or even the working hours. Certainly, it is not to be taken for granted in this field of research and I greatly appreciate it.

I am also very grateful to Matthew Walbran, my favorite Kiwi and laboratory partner, for his support with setting up the ToF spectrometer and the optically enhanced microwave source during my final year. Your help greatly relieved my burden and I definitely failed to honor it appropriately. Furthermore, I thank Friedrich Kirchner for the collaboration on the initial optical streaking experiment, Stefan Lahme for preparing most of the samples and for countless fruitful discussions about science, LabVIEW, and the ordeal of research, and all other current and former members of the UED group for interesting discussions and our group activities, such as the traditional döner lunch after the group meeting.

I thank Ernst Fill and Alexander Apolonski for the initiation of the electron pulse compression project as well as Grigory Kurkin's team from the Budker Institute of

Nuclear Physics in Novosibirsk for constructing the microwave cavity and especially Igor Zapryagaev for the on-site assistance and for all the struggle with the electronics. I also thank Casey Chew for suggesting the perfect detector for the ToF spectrometer and for giving me good advice based on her PEEM experiment. Moreover, I thank all colleagues from the Krausz group at the LMU building for the nice atmosphere and good collaboration as well as Rolf Oehm and his workshop team for professional consultation and supply of all mechanical components.

Besides all the work, there have always been opportunities for fun and amazement: At every Frauenchiemsee meeting or Christmas celebration, I am impressed and grateful to enjoy the almost military-grade organizational skills of our secretary Monika Wild, overseeing a crowd of more than 100 scientists. Kart racing with Volodymyr Pervak usually ends up in war and a very mean look from the race organizer, which is always a highlight. Thanks to Ivan Angelov I could restore my Quake skills after many years of abstinence. I thank all mentioned and unmentioned colleagues for the fun times we had outside the laboratory.

I am grateful to Casey Chew and Catherine Kealhofer for careful proofreading and helpful suggestions on the manuscript.

Finally, I thank my entire family, especially my parents Tamara and Nikolai Gliserin, for continuing and unconditional support throughout all these years. But most of all, I thank God for the wonderland of His creation, the gift of curiosity, and the hope which is in Him.